One quasi-particle properties of 1d quantum spin-systems by non-perturbative linked-cluster expansions

Master's Thesis in Physics

Presented by
Harald Leiser

2024-09-23

Friedrich-Alexander-Universität Erlangen-Nürnberg

Supervisor: Prof. Dr. Kai Phillip Schmidt
Dr. Max Hörmann

Abstract

An important step in understanding dynamical properties of quantum many-body systems is the investigation of one-particle properties in the thermodynamic limit. For a Hamiltonian $H = H_0 + V$, with H_0 already in block-diagonal form, we used the relatively new developed cluster-additive transformation (PCAT) to derive an effective block-diagonal Hamiltonian $H_{\text{eff}} = T^\dagger H T$. With this projective cluster-additive transformation (PCAT) we calculated the energy gap with numerical linked-cluster expansions (NLCEs) for the transverse field Ising model on various 1D lattice strips, namely the linear chain, saw-tooth lattice, ANNNI ladder and cross-stitch ladder. Moreover, the XXZ model up to three dimensions was considered. Also, we studied the scaling behaviour of this approach. By comparing the results of the energy gap with perturbative approaches, we see that the NLCE calculations converge well within the perturbative limit but diverge beyond due to (artificial) avoided level crossings on the finite clusters. The issue of avoided crossings, in general, is well known in perturbation theory and were also discussed in the gCUT framework. To understand the connections better we give an overview of this problem under different views and also show the relations to the appearance of exceptional points within the complex plane. Even though the work does not present a final framework overcoming the perturbative limit, many insights and ideas for further research have been presented.

Apart from that, we expand the framework of NLCE to obtain one-particle properties more efficiently. Specifically, we use the information on $S = \log T$ of a cluster expansion up to a cluster size with N spins to calculate $\exp(-S)H\exp(S)$ in the thermodynamic limit and compare this with the usual NLCE up to the same cluster-size.

Contents

1. Introduction 1

2. Methods 3
- 2.1. Effective Hamiltonian . . . 3
- 2.2. Linked cluster expansion and cluster additivity . . . 7
- 2.3. Block transformation method PCAT . . . 11
  - 2.3.1. Block diagnalizsation of matrices via eigenvectors . . . 12
  - 2.3.2. Cluster-additivity of PCAT . . . 14
- 2.4. CUT Method . . . 18
  - 2.4.1. Directly evaluated epCUT (deepCUT) . . . 20
  - 2.4.2. OS-CUT . . . 22
- 2.5. Numerical implementation of modified OS-CUT . . . 23
- 2.6. Extrapolations . . . 24

3. Avoided level crossings and exceptional points 27
- 3.1. General description . . . 27
- 3.2. Embedding of S as an Ansatz . . . 31
- 3.3. Example: linear cluster with additional spin . . . 33

4. Lattice Geometries 36
- 4.1. Linear Chain . . . 36
  - 4.1.1. NLCE and critical behaviour . . . 37
  - 4.1.2. CUT-Method: deepCUT . . . 39
  - 4.1.3. CUT-Method: OS-CUT . . . 41
  - 4.1.4. CUT method: OS-CUT numerical implementation . . . 43
- 4.2. Spin ladder . . . 46
  - 4.2.1. High-field limit . . . 46
  - 4.2.2. Low-field phase . . . 51
- 4.3. Saw-tooth chain . . . 55
- 4.4. ANNNI Model . . . 60
  - 4.4.1. Frustration and Phase-diagram . . . 60
  - 4.4.2. Energy gap . . . 62
- 4.5. Cross Stitch strip . . . 66

5. XXZ model 70
- 5.1. XXZ model in 1D . . . 70
  - 5.1.1. NLCE calculation . . . 72
  - 5.1.2. Exceptional Points . . . 77
  - 5.1.3. deepCUT . . . 80
- 5.2. XXZ Model in 2D and 3D . . . 81
- 5.3. Outlook and remaining questions . . . 84

6. Conclusion **87**
6.1. Summary . . . 87
6.2. Outlook . . . 88

A. Appendix **89**
A.1. NLCE for 1D lattices . . . 89
A.2. Modified OS-CUT on trimer . . . 90
A.3. OS-CUT ladder . . . 92
A.4. deepCUT for XXZ model . . . 92
A.4.1. First order . . . 93
A.4.2. Second order . . . 93

1. Introduction

The topic of quantum many-body physics describes the emergent phenomena of many interacting particles. The interesting point is that the physical interaction between the particles are well-known and can be often described by undergraduate quantum mechanics. However, their interplay leads to rich physical phenomena and unexpected macroscopic behaviour. In the words of P.W. Anderson, this can be described as *More is Different* [1]. Examples of such arising collective quantum effects are quantum spin liquids [2], superconductivity, topologically ordered phases [3], and many more.

The main focus of this work is on Ising spin lattice systems at zero temperature that contain a half-integer spin on each site. Due to zero temperature, the emerging phases are not driven by thermal fluctuations, but rather by quantum fluctuations [4]. The systems considered in this project consist of simple short-range Ising spin-spin interactions. However, due to the geometry of the lattices, different features emerge. One prominent example here is *geometric frustration*, which leads to a macroscopically degenerate ground state. Interestingly, this degeneracy is responsible for different phases. An extensive overview of different 2D lattices with geometric frustration is given by Moessner in [5]. Examples of well-known transitions based on geometric frustration are the disorder-by-disorder transition in the Kagome lattice and the order-by-disorder scenario in the triangular lattice [6]. Unfortunately, many of these spin systems (even those without frustration) are difficult to solve analytically, e.g., via Bethe ansatz [7] or applying Bogoliubov transformations. Consequently, we depend on numerical methods that try to capture the relevant information of the system. Since the corresponding Hilbert space scales exponentially with the number of particles considered, it is difficult to describe these systems within the thermodynamic limit (system size $N \to \infty$), leading to various truncation schemes.
Over the last four decades, many well-established methods have been developed, such as DMRG [8], tensor networks [9] and Quantum Monte Carlo [10] which use different perspectives to truncate the system appropriately. For example, DMRG and tensor networks use the entanglement entropy to access the targeted quantity efficiently. However, not every method is equally suited for all many-body spin system, which highlights why constant research on new and improved methods is necessary. Considering DMRG again, it has been found that its usage is mainly limited to one-dimensional systems.
Another example of a method is *continuous unitary transformations* (CUT) [11], whose ideas will also be used in this project. In comparison to the previously mentioned methods, the problem is mapped to a set of flow equations. In the specific implementations like sCUT and deepCUT [12], the system is then truncated at the level of operators.
Many of the methods have in common that the Hamiltonian is split up into two parts:

$$H = H_0 + xV \tag{1.1}$$

with H_0 already block-diagonal and $[H_0, V] \neq 0$. The reason why the above-mentioned methods are used instead of classical perturbation theory is that even there, efficient computation is non-trivial. However, one has to keep in mind that many of the previous

methods also use ideas of perturbation theory intrinsically, e.g., by expanding terms as powers of the perturbative parameter x.
In this thesis, we will use both perturbative and non-perturbative approaches to calculate effective models of low-lying excitations for various gapped spin systems. The difference between perturbative and non-perturbative methods lies in the specific implementation of the truncation scheme. A perturbative approach uses the perturbative order in x, leading to a result that is exact up to a certain order n. On the other hand, non-perturbative approaches take other parameters for truncation, like correlation length. Since we are interested in the low-lying excitations we derive an effective model $H_{\text{eff}} = T^\dagger H T$, which enables us to extract only the targeted information.

In this thesis, we will at first introduce the concepts of effective Hamiltonian and establish different methods of deriving them. The main focus will be on the cluster additive transformation PCAT (projective cluster-additive transformation)[13]. Since cluster additivity is important for our calculations, we explain the concept and show why PCAT fulfills this conditions. Therefore, we summarize the basic concepts presented in its original paper and try to explain connections to other methods like Schrieffer-Wolff [14]. Since the convergence of PCAT is currently limited to the perturbative regime due to avoided crossings, the basic concepts of these crossings and their connection to exceptional points are explained in section 3. In the main part of the thesis, PCAT is applied to different 1D spin models to gain insights in the strengths and differences of the approach in comparison with other methods. Therefore we use in section 4 different 1D Ising models with a transverse field. For each model, we explain the underlying physics and compare the calculated energy gap with results obtained from other methods. In addition, in section 5, the XXZ model is introduced. In comparison to the previous models, here we calculate not the energy gap but the energy of the bound states of the system. However, both kind of systems are suitable to examine the boundaries of NLCE. Lastly, all the insights obtained from the project are summarized in section 6. Besides, an outlook on future research aspects is given.

2. Methods

2.1. Effective Hamiltonian

As mentioned in the introduction (section 1), we focus here on problems of spin-$\frac{1}{2}$ models defined on a lattice where the Hamiltonian can be decomposed in two parts

$$H = H_0 + xV, \tag{2.1}$$

with H_0 the unperturbed part of the Hamiltonian and V the perturbation. We consider only systems, where H_0 has already been solved. For our cases, we assume that the spectrum of H_0 has a lower-bound, which is associated with the ground-state, donated by $|0\rangle$. All higher-lying states are then viewed as excitations or quasi-particles. For the n-particle state, we choose as a basis the eigenbasis of H_0, written in second quantization as:

$$|i_1, i_2, \cdots, i_n\rangle = b^\dagger_{i_1} b^\dagger_{i_2} \cdots b^\dagger_{i_n} |0\rangle\,, \tag{2.2}$$

where i_j ($j \in \{1, \cdots n\}$) denotes the lattice site, and $b^\dagger_{i_j}$ is the creation operator for a particle at site i_j. The advantage of this basis is that it is local, as each excitation corresponds to a lattice site i. This provides direct insight into the physical system. Since each lattice site is associated with a spin-$\frac{1}{2}$, there is a direct connection between a physical spin-flip and an excitation (see Mastsubara-Matsuda transformaion [15]). By choosing the z-axis as the reference axis, the connection between these local operators and the local Pauli-Matrices is:

$$\begin{aligned} \sigma^x_i &= b_i + b^\dagger_i, \\ \sigma^z_i &= 1 - 2b^\dagger_i b_i. \end{aligned} \tag{2.3}$$

Consequently, the operators b and $b^\dagger$ obey the hard-core boson relations, namely

$$b_i b_i = 0 = b^\dagger_i b^\dagger_i \qquad [b_i, b^\dagger_j] = \delta_{ij}(1 - 2n_i), \tag{2.4}$$

with the particle number operator $n_i = b^\dagger_i b_i$.
Before continuing with the internal structure of effective Hamiltonians, a brief introduction to the field of effective Hamiltonians is provided, following [16], [17] and [18].

The basic idea of an effective Hamiltonian is to simplify the complex structure of a system into a more manageable framework that captures only the relevant physics under investigation, such as low-lying excitations. This simplification enables a more detailed analysis of the system.
Starting at $x = 0$, both the eigenvalues E^0_i as well as the eigenvectors $|\phi_i\rangle_0$ are known through the relation

$$H_0 |\phi_i\rangle_0 = E^0_i |\phi_i\rangle_0\,, \tag{2.5}$$

where $|\phi_i\rangle_0 \in \mathcal{H}_0$ represents an element of the unperturbed Hilbert space $\mathcal{H}_0$. For $x \neq 0$, the unperturbed levels face an energy shift (level splitting):

$$H |\phi_i\rangle = (E_0 + \Delta E_{\phi_i}) |\phi_i\rangle\,, \tag{2.6}$$

where $|\phi_i\rangle \in \mathcal{H}$ is an element of the perturbed Hilbert space. We assume that the states of interest are adiabatically connected to the corresponding states of the unperturbed Hilbert space $\mathcal{H}_0$. This condition is expected to hold, at least for x within the region of interest, which in our case typically extends up to the point of a phase transition. For clarity, we refer the space of interest as Ω and the adiabatically connected initial manifold as Ω_0, which contains the unperturbed states (see fig. 1). The latter is also known as the *model space*. The idea is to set up a Hamiltonian (denoted H_{eff}) that describes Ω by acting only on Ω_0. Before going into details, we introduce the projectors P and Q, which divide $\mathcal{H}_0$ into Ω_0 and its complement $(1-\Omega_0)$, respectively. Acting with P or Q on an arbitrary state $|\Psi\rangle \in \mathcal{H}$ results into

$$P|\Psi\rangle \in \Omega_0, \tag{2.7}$$
$$Q|\Psi\rangle \in 1-\Omega_0. \tag{2.8}$$

The general properties of P and Q are

$$P^2 = P \qquad Q^2 = Q \qquad P+Q=1 \qquad PQ=0 \tag{2.9}$$
$$[H_0, P] = [H_0, Q] = 0. \tag{2.10}$$

This means that the Hamiltonian H is partitioned as follows:

$$H = \begin{pmatrix} E_i^{(0)} + xPVP & xPVQ \\ xQVP & QH_0Q + xQVQ \end{pmatrix}. \tag{2.11}$$

As previously mentioned, our aim is to construct H_{eff} so that it acts only within Ω_0, without losing the targeted information (e.g. low-lying excitations) contained in Ω. In other words, we want

$$H_{\text{eff}}|\phi_i\rangle_0 = E_i|\phi_i\rangle_0 \qquad \text{with} \quad |\phi_i\rangle_0 \in \Omega_0, \tag{2.12}$$
$$H|\phi_i\rangle = E_i|\phi\rangle \qquad \text{with} \quad |\phi_i\rangle \in \Omega. \tag{2.13}$$

In general, the requirements for H_{eff} are that it not only has the same eigenvalues but also maintains a one-to-one correspondence between the eigenvectors of H and H_{eff}. This is fulfilled by using an appropriate similarity transformation T

$$\bar{H} = T^{-1}HT. \tag{2.14}$$

Further it is assumed, that S decouples the subspaces Ω and $1-\Omega$

$$\bar{H} = \begin{pmatrix} P\bar{H}P & 0 \\ 0 & Q\bar{H}Q \end{pmatrix} = \begin{pmatrix} H_{\text{eff}} & 0 \\ 0 & Q\bar{H}Q \end{pmatrix}, \tag{2.15}$$

which ensures, that each eigenvector $|\alpha\rangle$ (with $P|\alpha\rangle = |\alpha\rangle$) of $\bar{H}$ belongs to the manifold Ω.
Up to this point, the general properties and demands for H_{eff} have been described, raising

the question of whether H_{eff} is unique. To answer this, we rewrite T in terms of $S = AB$, with A and B nonsingular operators, resulting into

$$H_A = A^{-1}HA = B\bar{H}B^{-1}. \tag{2.16}$$

Both H_A and $\bar{H}$ fulfill the conditions we set for a possible effective Hamiltonian, implying that the effective Hamiltonian has different representations, without losing its characteristic properties [16]. In the second half of the last century, different forms of T were proposed and expanded in a power series to get H_{eff} via perturbation theory. Names of important contributors to this field are Van Fleck, Bloch, Kato, Takahashi, des Cloiseaux and many more (for a overview see [18] and [19]). However, it was later shown that some of the different perturbative approaches leads to the identical effective Hamiltonian.
To illustrate, for a possible S, one can choose ([17])

$$T = \bar{P}(P\bar{P}P)^{-\nu} + \bar{Q}(Q\bar{Q}Q)^{-\nu}, \tag{2.17}$$

with $\bar{P}$ and $\bar{Q}$ the operators, which project into Ω and its complement, respectively. In the case of $\nu = 0$, this yields the non-hermitian Bloch effective Hamiltonian

$$H_{\text{eff,Bloch}} = PH\bar{P}(P\bar{P}P)^{-1}. \tag{2.18}$$

In contrast, for $\nu = 1/2$ one obtains the well-known hermitian effective Hamiltonian proposed by des Cloizeaux:

$$H_{\text{eff,dC}} = (P\bar{P}P)^{-1/2}\bar{P}H\bar{P}(P\bar{P}P)^{-1/2}. \tag{2.19}$$

In the paper of Takahashi ([20]), this formulation is used in combination with Kato's result [21]

$$\bar{P} = P - \sum_{n=1}^{\infty} x^n \sum_{\substack{k_1+k_2+\cdots+k_{n+1}=n \\ k_i \geq 0}} T^{k_1} V T^{k_2} V \cdots V T^{k_{n+1}}, \tag{2.20}$$

with $T^0 = -P$ and $T^k = \left(\frac{1-P}{E_0-H_0}\right)^k$ to set up a systematic way of calculating H_{eff} perturbatively. A good introduction of this is given in [22] and in [13].
To summarize, the aim is to construct a H_{eff} that contains all the information of the targeted states, while being written in terms of the unperturbed states. In the following sections, methods will be introduced that provide a systematic approach of constructing H_{eff}. Before that, we want to go a step toward the connection to the targeted quantities in this thesis by following the paper by C. Knetter el al. [23] and a review paper by P. Adelardt et al.[24].

For calculating the energy gap, we are interested into the dynamics of the one quasiparticle (1QP) states for $x > 0$. Dynamics means here hopping processes, where one excitation from site i can move to site j, driven by the perturbation. As mentioned, we assume that these fluctuations are continuously connected to the unperturbed 1QP states until the critical point. Therefore the space Ω_0 is spanned by all local 1QP states $|i\rangle = b_i^\dagger |0\rangle$.

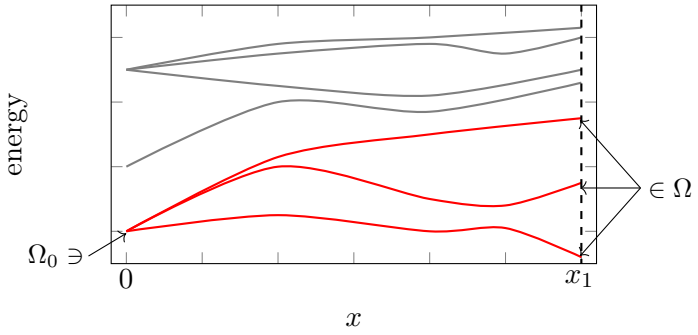

Figure 1: Schematic sketch of the energy levels as a function of x. The energy levels are adiabatically connected with the initial states at $x = 0$. The levels corresponding to the model space are marked in red. The goal is to obtain a Hamiltonian at $x_1 \neq 0$ that describes the corresponding states within the model space Ω_0.

The resulting 1QP states in Ω for $x > 0$ are then dressed states, which means, they contain contributions also from other QP numbers. For illustration, one can look at the following Hamiltonian,

$$H(x) = \begin{array}{c} \begin{matrix} \langle 001| & \langle 010| & \langle 100| & \langle 111| \end{matrix} \\ \begin{pmatrix} 2 & x & 0 & x \\ x & 2 & x & 0 \\ 0 & x & 2 & x \\ x & 0 & x & 6 \end{pmatrix} \end{array} \begin{matrix} |001\rangle \\ |010\rangle \\ |100\rangle \\ |111\rangle \end{matrix} \tag{2.21}$$

which is one $\mathbb{Z}_2$ symmetry block of the transverse-field Ising model (TFIM) on three sites (see section 4.1). By applying an appropriate transformation S (details how the transformation can be obtained see section 2.3), one can extract the 1QP sector for $x = 0.7$

$$PT^{-1}H(x = 0.7)TP = \begin{array}{c} \begin{matrix} \langle 001| & \langle 010| & \langle 100| \end{matrix} \\ \begin{pmatrix} 1.878 & -0.68 & -0.122 \\ -0.68 & 2 & -0.68 \\ -0.122 & -0.68 & 1.878 \end{pmatrix} \end{array} \begin{matrix} |001\rangle \\ |010\rangle \\ |100\rangle \end{matrix}$$

The corresponding basis states are written as a superposition from the entire Hilbert space:

$$\begin{aligned} |\phi_1\rangle_{x=0.7} &= 0.985\,|001\rangle + 0.005\,|010\rangle - 0.015\,|100\rangle + 0.169\,|111\rangle\,, \\ |\phi_2\rangle_{x=0.7} &= 0.005\,|001\rangle + 0.998\,|010\rangle + 0.005\,|100\rangle - 0.056\,|111\rangle\,, \\ |\phi_3\rangle_{x=0.7} &= -0.015\,|001\rangle + 0.005\,|010\rangle + 0.985\,|100\rangle + 0.169\,|111\rangle\,. \end{aligned}$$

For this thesis, we are always interested in an effective Hamiltonian associated with a certain number n of quasi-particles. This means in general, that H_{eff} should also fulfill:

$$[H_{\text{eff}}, Q] = 0 \qquad \Leftrightarrow \qquad H_{\text{eff}} = H_0 + H_1 + H_2 + \cdots\,, \tag{2.22}$$

with $Q = \sum_i n_i$ counting the number of quasi-particles of the whole system. For calculating the energy gap, a decomposition in form of $H_{\text{eff}} = H_0 + H_1 + H_{\text{rest}}$ is sufficient, since only information about the ground state and the first excitation is necessary. Here, it is important to note, that from now on, we denote the $T^{-1}HT$ as H_{eff}, since T constructs both the 0 and 1QP block. For the ground state and first excitation it leads to

$$H_0 \coloneqq E_0 \mathbb{1} \tag{2.23}$$

$$H_1 \coloneqq \sum_{ij} t_{ij} b_j^\dagger b_i \,. \tag{2.24}$$

The coefficients t_{ij} contains the desired information about all hopping processes from site i to site j. The generalization for H_n can be written as:

$$H_n \coloneqq \sum_{i_1 \cdots i_n j_1 \cdots j_n} t_{i_1 \cdots t_n j_1 \cdots j_n} b_{j_n}^\dagger \cdots b_{j_1}^\dagger b_{j_n} \cdots b_{j_1} \left|0\right\rangle . \tag{2.25}$$

From eq. (2.24) it is obvious that not only H_1 acts on Ω_0 (model space of 1QP), but also H_0. To extract only 1QP information, one has to subtract the ground-state contribution:

$$\begin{aligned} H_0|_0 &\coloneqq H_{\text{eff}}|_0, \\ H_1|_1 &\coloneqq H_{\text{eff}}|_1 - H_0|_1, \end{aligned} \tag{2.26}$$

with $H_0|_0$ and $H_1|_1$ denoting the 0QP and 1QP contribution which only acts on the 0QP and 1QP basis states respectively. This scheme can also be easily extended to higher particle states. The difference between H_1 and $H_1|_1$ is crucial in the context of cluster-additivity as we will see in the next section.

2.2. Linked cluster expansion and cluster additivity

The aim of the methods presented in this thesis is to calculate physical quantities in the thermodynamic limit (system size $N \to \infty$). One direct approach of extracting information in this limit is *exact diagonalization* (ED) of sufficient large finite systems. Here, *sufficiently large* means that the size has to be chosen large enough to capture most of the physical processes in the thermodynamic limit with the desired precision. However, a major downside of this straightforward method is, that the Hilbert space often grows exponentially with system size N, which leads to computational memory problems. For example, a system with 300 spins has a Hilbert space of $\dim(\mathcal{H}) = 2^{300}$, which reaches the number of atoms in the visible universe ($\mathcal{O}(10^{80})$). Although techniques such as using sparse matrices or exploiting system symmetries can reduce memory requirements, the realizable system sizes are generally limited to relatively small ones.
Due to this problem, we use a cluster expansion to calculate the energy gap, which shows also better convergence behaviour compared to ED calculations. The basic idea behind this kind of ansatz is to perform a series expansion based on finite clusters of the system. Hereby, the physical quantity in the thermodynamic limit is decomposed into

contributions from smaller cluster sizes:

$$O(x) \overset{\text{therm. limit}}{=} \text{contribution of cluster 1} + \text{contribution of cluster 2} + \text{contribution of cluster 3} + \cdots \tag{2.27}$$

Regarding the desired precision, one only needs to perform calculations on specific clusters and to take only processes (contributions) up to a certain order into account. To simplify the cluster expansion, we focus here on so-called *linked-cluster expansion*, which means that we only consider linked clusters or graphs. A cluster C is called disjoint (not linked) if its corresponding Hamiltonian can be written as

$$H_C = H_A \otimes \mathbb{1} + \mathbb{1} \otimes H_B, \tag{2.28}$$

with $C = A \cup B$. Otherwise it is referred to as linked. By considering only local interactions between lattice sites, the system can be represented as a graph, where the vertices correspond to lattice sites and the edges represent possible interactions between them. A linked cluster is a graph, where every point i is connected with every other point j by at least one path. Consequently, if such a path does not exist for two points or vertices, the graph is called disjoint.
Before proposing conditions on linked-cluster expansions, we note, that two types of linked-cluster expansion can be distinguished: perturbative and non-perturbative ones. In the first type, perturbation theory is applied to each cluster and the resulting series is truncated based on the perturbative order. In the second type, exact calculations on the linked subgraphs (*numerical linked cluster expansion*, NLCE) are performed. Therefore the truncation (taking only subgraphs up to length N) is determined by the correlation length. Details can be found in section 2.3.

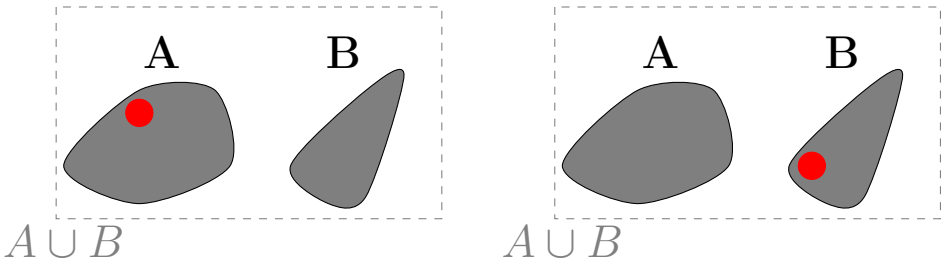

Figure 2: Illustration of a cluster $A \cup B$ consisting out of two disjoint subclusters A and B. For states with one excitation, the excitation (marked as red dot) is either on cluster A (left side) or on cluster B (right side).

To perform only calculations on linked clusters, the operator $O(x)$ of physical quantity under consideration has to satisfy *cluster additivity*, which means that the contribution of two disjoint clusters $A \cup B$ can be expressed as the sum of the contributions from cluster A and B:

$$O(A \cup B) = O(A) + O(B). \tag{2.29}$$

Thus, contributions from disjoint clusters vanish in the expansion. Cluster-additivity is always fulfilled for extensive quantities, such as the ground-state energy E_0, because these quantities scale with the system size N. Therefore, they can be decomposed into its individual contributions per lattice site, as in $O = \sum_{i=1}^{N} O_i$ for O an extensive quantity and O_i the contribution per lattice site i. The ground-state energy provides a clear example, as $H_0 = \mathbb{1}E_0$. Consequently, for two disjoint clusters A and B, one obtains:

$$E_0(A \cup B) = \langle 0| H^{A\cup B} |0\rangle = \langle 0| H^A \otimes \mathbb{1} |0\rangle + \langle 0| \mathbb{1} \otimes H^B |0\rangle = E_0(A) + E_0(B) \quad (2.30)$$

which precisely satisfies the definition of cluster additivity.
For quantities such as the effective Hamiltonian $H_{\text{eff}}|_1$ cluster-additivity does not hold.

In a 1996 paper [25], Gelfand described that by subtracting the ground-state energy, one obtains a cluster-additive quantity.
To understand this better, we briefly describe the idea presented by Gelfand: Considering a cluster $A \cup B$ consisting out of two disjoint clusters A and B. The excitation can be located either in cluster A or in cluster B (see fig. 2):

$$|1\text{QP}, A \cup B\rangle_A = |1\text{QP}, A\rangle \otimes |0\text{QP}, B\rangle \quad \text{or} \quad |1\text{QP}, A \cup B\rangle_B = |0\text{QP}, \text{A}\rangle \otimes |1\text{QP}, \text{B}\rangle \quad (2.31)$$

Due to the missing connection between the graphs, an excitation cannot move from A to B. This means, by starting with an excitation on cluster A, any resulting state will have no overlap with the state of an excitation at B:

$$P_{1,A} |1\text{QP}, A \cup B\rangle_B = 0 \quad (2.32)$$

with $P_{1,A}$ the projector onto the 1QP states on cluster A. From these physical conditions, in which no hopping between the disjoint clusters is allowed, the corresponding effective Hamiltonian of the disjoint cluster $C = A \cup B$ can be written into the following form:

$$P_{1,C} H^C_{\text{eff}} P_{1,C} = (H^A_{\text{eff}}|_1 + E_0(B)) \oplus (H^B_{\text{eff}}|_1 + E_0(A)), \quad (2.33)$$

with $H^A_{\text{eff}}|_1$ and $H^B_{\text{eff}}|_1$ being the effective Hamiltonian of cluster A and B, restricted to the 1QP sector, respectively. It is important to note that eq. (2.33) is not fulfilled for every transformation T, it is instead a requirement on T, derived on our physical boundary conditions. Obviously, eq. (2.33) is not cluster-additive because H^C_{eff} is not block-diagonal in terms of the disjoint clusters. By subtracting $E_0(C) = E_0(A) + E_0(B)$, one gets

$$H^C_{\text{eff}} - E_0(C) = (H^A_{\text{eff}} - E_0(A)) \oplus (H^B_{\text{eff}} - E_0(B)), \quad (2.34)$$

which satisfies the cluster-additivity condition. Consequently, by finding an appropriate transformation T that fulfills eq. (2.33), we can determine the energy gap based on a linked cluster expansion of $H^C_{\text{eff}} - E_0(C)$. This highlights the importance of this statement for our project, as we will mainly focus on calculating the energy gap of various systems. In [23], cluster additivity was generalized to multiparticle excitations and the condition of cluster-additivity was rewritten as:

$$H_{\text{eff}}(A \cup B) = H_{\text{eff}}(A) \otimes \mathbb{1}_B + \mathbb{1} \otimes H_{\text{eff}}(B). \quad (2.35)$$

In other words, if an effective Hamiltonian takes this form, it can always be decomposed into cluster-additive parts (e.g., subtraction of the ground-state energy from the 1QP block), and a linked-cluster expansion can be applied. In particular, only the quantities on the right side of eq. (2.26) are cluster additive, the restricted Hamiltonian $H_{\text{eff}}|_n$ is not. An comprehensive review for higher excitations can be also found in [24].

Figure 3: Cluster expansion of a linear chain.

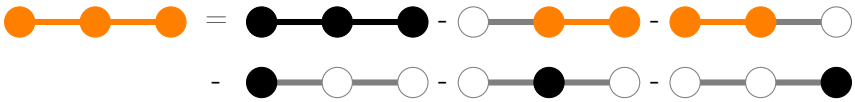

Figure 4: Schematic representation how to calculate the reduced contribution of a cluster with three sites. The color red marks the reduced graphs.

After having shown that $H_1|_1$ a cluster-additive quantity, the next question is how to calculate the gap in terms of a cluster-expansion. The procedure is similar to the ground-state energy (detailed formulation in [26]): when calculating the contribution from cluster C, one has to subtract all contributions from smaller subgraphs C' that are already contained in C ($C' \subset C$) to avoid double counting the same processes:

$$\tilde{H}'_{\text{eff,C}} = H'_{\text{eff,C}} - \sum_{C' \subset C} \tilde{H}'_{\text{eff,C}'} \tag{2.36}$$

This relation can be solved iteratively. For example, fig. 3 shows the decomposition of the linear chain. To calculate the contributions of C_3 to the energy gap in the thermodynamic limit, one first calculates the cluster-additive Hamiltonian $H'_{\text{eff,C}_3}|_1 = H_{\text{eff,C}_3}|_1 - E_0(C_3)\mathbb{1}$. Afterwards, all lower contributions (hopping processes) present on smaller graphs are subtracted. For the given case, the clusters C_1 and C_2 are subtracted by embedding them onto C_3 (see fig. 4)

$$\begin{aligned}\tilde{H}'_{\text{eff,C}_3}|_1 = H'_{\text{eff,C}_3}|_1 &- \tilde{H}'_{\text{eff,C}_2}|_1 \otimes \mathbb{1} - \mathbb{1} \otimes \tilde{H}'_{\text{eff,C}_2}|_1 \\ &- H'_{\text{eff,C}_1}|_1 \otimes \mathbb{1}_2 - \mathbb{1}_2 \otimes H'_{\text{eff,C}_1}|_1 - \mathbb{1} \otimes H'_{\text{eff,C}_1}|_1 \otimes \mathbb{1}\end{aligned}$$

with $\tilde{H}'_{\text{eff,C}_2}|_1 = H'_{\text{eff,C}_2}|_1 - H'_{\text{eff,C}_1}|_1 \otimes \mathbb{1} - \mathbb{1} \otimes H'_{\text{eff,C}_1}|_1 = \sum_{i,j\in\{0,1\}} \tilde{t}_{ij} b_i^\dagger b_j$ and $\mathbb{1}_2 = \mathbb{1} \otimes \mathbb{1}$. Afterwards, all reduced contributions are embedded into the entire infinite lattice to restore translational invariance. This is accomplished by applying a Fourier transform to the hopping terms. The Fourier transformed creation/annihilation operators are

$$b_{\vec{k}}^\dagger = \frac{1}{\sqrt{N}} \sum_i e^{-i\vec{k}\vec{r}_i} b_i^\dagger \qquad b_{\vec{k}} = \frac{1}{\sqrt{N}} \sum_i e^{-i\vec{k}\vec{r}_i} b_i \tag{2.37}$$

For example, for embedding $\tilde{H}'_{\text{eff,C}_2}$ into the infinite chain results into a cosine relation:

$$\tilde{H}'_{\text{eff,C}_2} = \sum_{i,j\in\{0,1\}} \tilde{t}_{ij} b_i^\dagger b_j \xrightarrow{\text{F.T.}} \sum_k \left(\tilde{t}_{0,1} 2\cos(k) + (\tilde{t}_{0,0} + \tilde{t}_{1,1})\right) b_k^\dagger b_k \tag{2.38}$$

For systems with only one translational invariant real axis, the series expansion for the gap up to cluster C_i can be calculated as:

$$\Delta_{\text{NLCE},C_i} = \Delta_{C_i} - \Delta_{C_{i-1}} \tag{2.39}$$

with Δ_{C_i} the gap determined by embedding $H_{\text{eff},C_i}|_1 - E_0(C_i)\mathbb{1}$ and Δ_{NLCE,C_i} the resulting gap of the cluster-expansion by considering all graphs up to cluster size C_i.
This relation saves both computational time and memory. Because, to calculate the energy gap for cluster sizes up to, for example, 5 spins, it is sufficient to compute the effective Hamiltonian for clusters with 4 and 5 spins only. Therefore, one overcomes the need to calculate and embed the contributions from smaller clusters.

2.3. Block transformation method PCAT

The transformation method PCAT (*projective cluster additive transformation*) published in 2024 by M. Hörmann and K. P. Schmidt [13] is one of many ways of extracting the effective Hamiltonian, which leads to the question why this methods is important. Although methods like MBOT (*multi block orthogonal transformation*) or the slightly modified version TBOT (*two block orthogonal transformation*) [27], already exist for calculating the effective Hamiltonian perturbatively, both methods have noteable downsides that limits their application The first disadvantage is the low efficiency of MBOT ([26]), which limits the ability to calculate high orders. In contrast, TBOT is much faster, but on the other hand the resulting effective Hamiltonian is not cluster additive in general. The latter point is crucial for performing a linked-cluster expansion. As we will understand in detail later, TBOT leads to a cluster-additive transformation only if the regarding blocks are separated from lower-lying excitations by symmetries. For example, the calculation of the 1QP block is cluster-additive if there is a symmetry that prevents coupling to the ground state. For the transverse-field Ising model, this is always the case due to the $\mathbb{Z}_2$ symmetry. To clarify this point, one can consider the following toy Hamiltonian [13]

$$H = \sum_i \sigma_i^z + x \sum_i \sigma_i^x \sigma_{i+1}^x + \mu \sigma_i^z \sigma_i^x + \mu \sigma_i^x \sigma_{i+1}^z. \tag{2.40}$$

Due to the term $\sigma_i^z \sigma_i^x + \sigma_i^x \sigma_{i+1}^z$ ground and excited states are connected. As stated in [23], for doing a linked-cluster expansion the following condition has to hold:

$$T_{\text{TBOT}}^\dagger H_{A\cup B} T_{\text{TBOT}} = H_{\text{eff},A\cup B} = H_{\text{eff},A} \otimes \mathbb{1}_B + \mathbb{1}_A \otimes H_{\text{eff},B} \tag{2.41}$$

with T_{TBOT} the transformation determined by TBOT.
To illustrate it further, we examine the system displayed in fig. 5. The Hamiltonian consists of two disconnected three-site clusters. If the above statement holds, no hopping

process should appear between the subclusters ($H_{\text{eff},A\cup B}$ stays block-diagonal with respect to the clusters A and B). By applying TBOT, we obtain the effective Hamiltonian for the case $\mu = 1$ in order $\mathcal{O}(6)$ as follows:

$$H_{\text{toy}}^{(6)} = \begin{pmatrix} -1.93 & 0 & 0.09 & -0.05 & 0 & -0.05 \\ 0 & -0.23 & 0 & 0 & 0.094 & 0 \\ 0.09 & 0 & -1.93 & -0.05 & 0 & -0.05 \\ -0.05 & 0 & -0.05 & -1.93 & 0 & 0.09 \\ 0 & 0.09 & 0 & 0 & -0.23 & 0 \\ -0.05 & 0 & -0.05 & 0.09 & 0 & -1.93 \end{pmatrix} \tag{2.42}$$

The colored areas mark the parts which are associated with cluster A and B respectively. As it can be seen, non-zero off-diagonal elements arise which represent hopping processes between the two disconnected clusters. In [13] it is shown, that the transformation can be modified to restore cluster-additivity, which is the origin of its name PCAT. Before recapitulating the reasons why PCAT is cluster-additive, we first want to give a general perspective on block-diagonal transformations on finite systems by using the exact eigenstates.

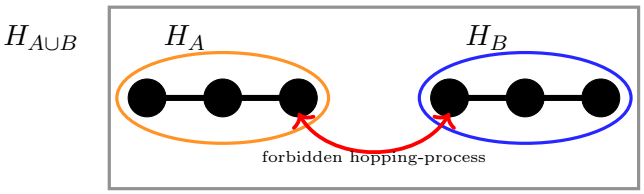

Figure 5: Example set-up of a system $H_{A\cup B}$ consisting out of two dislinked clusters A and B.

2.3.1. Block diagnalizsation of matrices via eigenvectors

In principle, the block-diagonalization of a matrix can be performed either perturbatively (as with TBOT/MBOT routines and Schrieffer-Wolff transformation [14]) or by applying continuous unitary transformation (CUT) methods on finite systems. Here we use a unitary transformation T constructed by the exact eigenvectors of the system. The transformation is introduced in all detail by [28]. For completeness and because there is still the unsolved question how to modify T to fulfill cluster additivity beyond the perturbative limit, the transformation is introduced in depth in the following.

The transformation of a given matrix into a block-diagonal form is generally not a well-defined requirement because, without further constraints, many transformations can be used. However, before specifying these constraints, one can already state the general structure of T by splitting T into a product of two matrices: $T = AB$. To see this, we assume, that there exists a transformation T that brings H into block form $H_{\text{block}} = T^\dagger H T$. From this, one can write the secular (or characteristic) equation as

$$HX = X\Lambda, \tag{2.43}$$

with the matrix $X = (|\phi_1\rangle, |\phi_2\rangle, \cdots)$ containing the eigenvectors ϕ_i of H and the diagonal matrix Λ containing the corresponding eigenvalues λ_i. The condition $XX^\dagger = \mathbb{1}$ is still fulfilled, if each eigenvector ϕ_i is multiplied by a phase factor α_i. Writing down the secular equation for H_{block} leads to

$$H_{\text{block}} F^\dagger = F^\dagger \Lambda, \tag{2.44}$$

with the matrix $F = (|\psi_1\rangle, |\psi_2\rangle, \cdots)$ containing the eigenvectors $|\psi_i\rangle$ of the transformed matrix. Plugging $\Lambda = X^\dagger H X$ in the last equation leads to

$$T = XF. \tag{2.45}$$

Consequently, the transformation consists of one part that diagonalizes the matrix and a second part that constructs the corresponding blocks. But still, the exact form of F remains arbitrary. As proven in [28], the condition of the least action, namely

$$\|T - \mathbb{1}\| = \text{minimal}, \tag{2.46}$$

leads to a unique form of T (for T being unitary), with $\|\cdot\|$ being an Euclidean norm. This condition ensures that the transformation changes the initial Hamiltonian only as much as necessary. The transformation can be constructed using the exact eigenstates of the system. For the n-particle block the transformation is given as

$$T_n = \sum_{k \in s_n} X_{i,k} \left(X_{s_n}^{P_n \dagger} \left(X_{s_n}^{P_n} X_{s_n}^{P_n \dagger} \right)^{-1/2} \right), \tag{2.47}$$

where the index set s_n contains the indices of the n-QP states. The matrix $X_{s_n}^{P_n}$ is defined as

$$X_{s_n}^{P_n} = P_n X_{s_n} P_n, \tag{2.48}$$

with P_n the projector into the unperturbed n-QP eigenstates. Thus, $X_{s_n}^{P_n}$ is a square matrix (for the 1QP sector, it would be an $N \times N$ matrix, with N the number of 1QP states). The reason why the transformation can be constructed using only the eigenstates of the system can be motivated by the fact, that all information of H is contained in its eigenvectors and eigenvalues. Since the block-structure is given by H_0 (or Ω_0), the only quantity which determines T_n are the corresponding eigenvectors.
Before explaining why the transformation is only cluster-additive for certain cases and how this issue is fixed by PCAT, we want to give some additional notes regarding eq. (2.47) and its relation to other transformations. As shown in [13], the same transformation can be also obtained by rewriting the effective Hamiltonian eq. (2.19) [1]

$$T_{\text{deCloizeaux}} = \bar{P} P (P \bar{P} P)^{-0.5} \tag{2.49}$$

into an formulation based on eigenstates. This can be done by expressing the projectors in terms of

$$P = \sum_{k \in s_{\Omega_0}} X_{0,i,k} X_{0,k,j}^\dagger \quad \text{and} \quad \bar{P} = \sum_{k \in s_{\Omega_0}} X_{i,k} X_{k,j}^\dagger, \tag{2.50}$$

[1] Note that $(P_0 P P_0)^{-0.5} = P_0 (P_0 P P_0)^{-0.5}$

with X_0 denoting the unperturbed eigenstates from the model space, and s_{Ω_0} the set of indices of the corresponding states under consideration. Furthermore, the transformation for decoupling only two spaces is equivalent to the Schrieffer-Wolff transformation. In [14] (eq. (26) and (27)) , it was shown that the Schrieffer-Wolff transformation can be written as

$$T_{\mathrm{SW}} = \sqrt{(2P - \mathbb{1})(2\bar{P} - \mathbb{1})} = \sqrt{(P - Q)(\bar{P} - \bar{Q})}. \tag{2.51}$$

That this formulation is equivalent to $T_{\mathrm{deCloizeaux}}$ (eq. (2.49)) is e.g. presented explicitly by M. Hörmann in [13]. This can be also seen from the fact, that both eq. (2.47) and T_{SW} have minimal norm. Since $\bar{P}$ is often not known, T_{SW} is determined perturbatively. In the next section the transformation is used to explain why the transformation is only cluster-additive for certain cases and how this issue is fixed in the framework of PCAT.

2.3.2. Cluster-additivity of PCAT

Before we describe the method of PCAT in detail, it is important to understand why the minimal transformation T is not cluster-additive in general (T is equal to the perturbative transformation of TBOT, since both have minimal norm [13]). To illustrate this, we consider the first excitation from the toy Hamiltonian in eq. (2.40), which is also used in the original PCAT paper. As before, we consider two disjoint clusters A and B (see e.g. fig. 5), such that the total Hamiltonian becomes:

$$H = H_A + H_B \qquad \text{with } [H_A, H_B] = 0. \tag{2.52}$$

Since the excitation is either on cluster A or on cluster B, the 1QP states can be written as:

$$|\phi_i\rangle_{1,A\cup B} = |\phi\rangle_{1,A} \otimes |\phi\rangle_{0,B} \tag{2.53}$$

$$\text{or } |\phi_i\rangle_{1,A\cup B} = |\phi\rangle_{0,A} \otimes |\phi\rangle_{1,B} \tag{2.54}$$

for $i \in \{1, \cdots, N\}$ denoting the possible N 1QP-states.
For the case $\mu = 0$, the ground state and first excitation are separated by parity symmetry, which means:

$$\langle\phi_i|_{1,A} P_{1,A} |\phi_j\rangle_{0,A} = 0 \quad \text{and} \quad \langle\phi_i|_{1,B} P_{1,B} |\phi_j\rangle_{0,B} = 0 \qquad \forall i, j \in [1, \cdots, N], \tag{2.55}$$

with $P_{1,A}$ and $P_{1,B}$ the projector onto the unperturbed 1QP states of cluster A and B, respectively. The operator P_1 acting on $A \cup B$ can be decomposed as:

$$P_1 = P_{0,A} \otimes P_{1,B} + P_{1,A} \otimes P_{0,B} \qquad \text{and} \qquad (P_{0,A} \otimes P_{1,B})(P_{1,A} \otimes P_{0,B}) = 0. \tag{2.56}$$

The projectors $P_{n,A}$ / $P_{n,B}$ ($n \in \mathbb{N}$) project onto the unperturbed n-particle eigenstates of cluster A and B, respectively. As discussed in section 2.3.1, knowing all the eigenstates and the block-structure, one has all information needed to construct T. For illustration,

we consider only two eigenvectors $|\phi_1\rangle = |\phi_1\rangle_{1,A\cup B}$ and $|\phi_2\rangle = |\phi_2\rangle_{1,A\cup B}$ where the first having an excitation on cluster A and the second on cluster B:

$$X_{s_1}^{P_1} = \begin{pmatrix} | & | \\ |\phi_1\rangle_{s_1} & |\phi_2\rangle_{s_1} \\ | & | \end{pmatrix}. \tag{2.57}$$

The subscript s_1 denotes that we only consider the corresponding N entries of each column which belongs to the 1QP block (s_1 is determined by H_0 or Ω_0). Consequently, $X_{s_1}^{P_1}$ is an $N \times N$ matrix, which becomes block-diagonal with respect to the associated clusters because

$$\begin{aligned} \langle\phi_1| P_1 |\phi_2\rangle &= (\langle\phi|_{1,A} \otimes \langle\phi|_{0,B})(P_{0,A} \otimes P_{1,B} + P_{1,A} \otimes P_{0,B})(|\phi\rangle_{0,A} \otimes |\phi\rangle_{1,B}) \\ &= \underbrace{\langle\phi|_{1,A} P_{0,A} |\phi\rangle_{0,A}}_{=0} \cdot \underbrace{\langle\phi|_{0,B} P_{1,B} |\phi\rangle_{1,B}}_{=0} + \underbrace{\langle\phi|_{1,A} P_{1,A} |\phi\rangle_{0,A}}_{=0} \cdot \underbrace{\langle\phi|_{1,0} P_{0,B} |\phi\rangle_{1,B}}_{=0} \\ &= 0. \end{aligned}$$

Hence, eigenvectors with one excitation on cluster A have no overlap (i.e. are orthogonal in the considered projected subspace) to all other eigenvectors with an excitation on cluster B. This results into the desired structure:

$$X_{s_1}^{P_1} = \begin{pmatrix} |\Psi\rangle_A & \\ & |\Psi\rangle_B \end{pmatrix} \Rightarrow \left(X_{s_1}^{P_1\dagger} \left(X_{s_1}^{P_1} X_{s_1}^{P_1\dagger} \right)^{-1/2} \right) = \begin{pmatrix} \text{Cluster A} & \\ & \text{Cluster B} \end{pmatrix}$$

Remembering, that only $X_{s_1}^{P_1\dagger}\left(X_{s_1}^{P_1} X_{s_1}^{P_1\dagger}\right)^{-1/2}$ is responsible for the structure inside the 1QP block (the other part of T only brings the matrix in diagonal form). From this it follows, that the 1QP block of the effective Hamiltonian can be written as the sum of the corresponding cluster contributions:

$$P_1 T^\dagger H T P_{1,A} = P_{1,A} \otimes P_{0,B}(T^\dagger H T) P_{1,A} \otimes P_{0,B} \oplus P_{0,A} \otimes P_{1,B}(T^\dagger H T) P_{0,A} \otimes P_{1,B} \tag{2.58}$$

$$= (P_{1,A} H_{\text{eff},A} P_{1,A} + E_0(B)) \oplus (P_{1,B} H_{\text{eff},B} P_{1,B} + E_0(A)), \tag{2.59}$$

with $P_{1,A} \otimes P_{0,B} T^\dagger H T P_{0,A} \otimes P_{1,B} = 0$, due to the block structure of $X_{s_1}^{P_1}$. This leads directly to cluster-additivity when the ground-state energy $E_0(C)$ is subtracted.
In general, this symmetry protection is not always given, especially for higher quasi-particle blocks. A coupling between the ground-state and the first-excitation is in the example Hamiltonian the case for $\mu \neq 0$, as it can be seen by $\langle\phi_1| P_1 |\phi_2\rangle \neq 0$. Consequently, cluster-additivity is not fulfilled in general. To achieve cluster-additivity for such systems, one has to modify the eigenvectors appropriately. This is also in alignment with the previous section about the transformation in general, where the only knowledge

about the system, besides the sizes of the individual blocks, are the eigenvectors. Concretely, to restore cluster-additivity, one has to subtract from the corresponding entries of the 1QP eigenvectors the ground-state contributions:

$$|\tilde{\Psi}\rangle_1 = |\Psi\rangle_1 - \frac{\langle 0|\Psi\rangle_1}{\langle 0|\Psi\rangle_0}|\Psi\rangle_0\,, \tag{2.60}$$

with $|\Psi\rangle$ and $|\Psi\rangle_0$ the eigenvector associated with an excitation and the ground state, respectively. The state $|0\rangle \in \mathcal{H}_0$ denotes the unperturbed ground state. This scheme is unique as long as $P_0|\Psi\rangle_0 \neq 0$. However, due to this subtraction procedure, the resulting vectors are no longer orthogonal and normalized anymore. As before, the eigenvectors for the disconnected cluster are written

$$|\tilde{\phi_i}\rangle_{1,A\cup B} = |\tilde{\phi}\rangle_{1,A} \otimes |\tilde{\phi}\rangle_{0,B} \tag{2.61}$$

$$\text{or } |\tilde{\phi_i}\rangle_{1,A\cup B} = |\tilde{\phi}\rangle_{0,A} \otimes |\tilde{\phi}\rangle_{1,B}, \tag{2.62}$$

but now with the modified vectors. And we get for the transformation:

$$\tilde{X}^{P_1}_{s_1} = \left(\begin{array}{cc} |\Psi\rangle_A & \\ & |\Psi\rangle_B \end{array} \right) \Rightarrow \left(\tilde{X}^{P_1\dagger}_{s_1} \left(\tilde{X}^{P_1}_{s_1} \tilde{X}^{P_1\dagger}_{s_1} \right)^{-1/2} \right) = \left(\begin{array}{cc} \text{Cluster A} & \\ & \text{Cluster B} \end{array} \right)$$

This can be clearly seen by studying two arbitrary modified eigenstates $|\phi_1\rangle = |\phi_1\rangle_{1,A\cup B}$ and $|\phi_2\rangle = |\phi_2\rangle_{1,A\cup B}$, with the excitation on cluster A / B, respectively. The resulting matrix

$$\tilde{X}^{P_1}_{s_1} = \begin{pmatrix} | & | \\ |\tilde{\phi_1}\rangle_{s_1} & |\tilde{\phi_2}\rangle_{s_1} \\ | & | \end{pmatrix} \tag{2.63}$$

becomes block-diagonal

$$\langle \tilde{\phi_1}|P_1|\tilde{\phi_2}\rangle = 0, \tag{2.64}$$

with

$$P_1 = P_{0,A} \otimes P_{1,B} + P_{1,A} \otimes P_{0,B} \qquad \text{and} \qquad (P_{0,A} \otimes P_{1,B})(P_{1,A} \otimes P_{0,B}) = 0. \tag{2.65}$$

This can be checked, by applying P_1 to the states

$$P_1|\phi_1\rangle = P_{0,A}|\tilde{\phi_1}\rangle_{A,1} \otimes P_{1,B}|\tilde{\phi_1}\rangle_{B,0} + P_{1,A}|\tilde{\phi_1}\rangle_{A,1} \otimes P_{0,B}|\tilde{\phi_1}\rangle_{B,0} \tag{2.66}$$

$$= (P_{1,A} \otimes P_{0,B})|\tilde{\phi_1}\rangle \tag{2.67}$$

$$P_1|\phi_2\rangle = P_{0,A}|\tilde{\phi_2}\rangle_{A,0} \otimes P_{1,B}|\tilde{\phi_2}\rangle_{B,1} + P_{1,A}|\tilde{\phi_2}\rangle_{A,1} \otimes P_{0,B}|\tilde{\phi_2}\rangle_{B,1} \tag{2.68}$$

$$= (P_{0,A} \otimes P_{1,B})|\tilde{\phi_2}\rangle. \tag{2.69}$$

Consequently, the states are orthogonal with respect to the projection P_1 into the 1QP states. This leads to the above proposed block-diagonality and further ensures cluster-additivity. Note that only the states of the matrix F (eq. (2.45)) have to be modified, since only they determine the structure inside each block.
So far, only the first excitation has been considered, but in principle the subtraction scheme of PCAT can also be applied to higher orders to restore cluster-additivity. For example, for the 2QP block, one would have to do following adjustments:

$$\left|\tilde{\Psi}\right\rangle_2 = |\Psi\rangle_2 - \frac{\langle 0|\Psi\rangle_2}{\langle 0|\Psi\rangle_0}|\Psi\rangle_0 \tag{2.70}$$

$$- M^{-1}P_1|\Psi\rangle_2\,, \tag{2.71}$$

with $M = P_1\tilde{X}P_1$ and $\tilde{X}$ the matrix containing the modified eigenvectors regarding the 1QP block. The formal description for a generalized n-particle excitation can be found in the original publication [13]. Nevertheless, to illustrate the further procedure, fig. 6 shows how the scheme continues for higher particle states. The idea is, that for the nQP state, one has to find a linear combinations of all lower number states, such that:

$$P_i|nQP\rangle = 0 \qquad \forall i \in \{0, \cdots, n-1\}. \tag{2.72}$$

Because the transformation can be written as

$$T = \sum_n T_n, \tag{2.73}$$

it is only necessary to subtract the corresponding blocks, e.g. if one is only interested in the energy gap, only subtraction of the ground-state is required.
We want to emphasize again that only the resulting effective Hamiltonian becomes cluster-additive, while the transformation T itself is not. Instead, T is cluster-multiplicative. Since we can write:

$$H_{\text{eff},A\cup B} = T^\dagger H T \stackrel{!}{=} H_{\text{eff},A}\otimes\mathbb{1}_B + \mathbb{1}_A\otimes H_{\text{eff},B} \tag{2.74}$$

and

$$T^\dagger H T = T^\dagger(H_A\otimes\mathbb{1}_B + \mathbb{1}_A\otimes H_B)T = T^\dagger(H_A\otimes\mathbb{1}_B)T + T^\dagger(\mathbb{1}_A\otimes H_B)T, \tag{2.75}$$

it follows that $T = T_A\otimes T_B$. Furthermore, every unitary transformation can be expressed as $T = e^S$, where S is the generator (anti-Hermitian matrix). In contrast to T, S fulfills cluster-additivity:

$$e^{S_C} = T = T_A\otimes T_B = e^{S_A}\otimes e^{S_B} = e^{S_A\oplus S_B} = e^{S_A\otimes\mathbb{1}_B + \mathbb{1}_A\otimes S_B}, \tag{2.76}$$

with $\oplus$ the Kronecker sum and $C = A\cup B$. Consequently $S_C = S_A\otimes\mathbb{1} + \mathbb{1}\otimes S_B$ is cluster additive. This circumstance will be important later (see section 3).

One can apply the method of PCAT directly using the exact eigenvectors. Alternatively, the scheme can be used to overcome the cluster-additivity problem of TBOT.

Therefore, one calculates the orthogonal transformation $O^{(n)}$ from TBOT up to order n and uses its entries (columns) as the corresponding eigenvectors. Since this is a perturbative approach, Taylor expansions are used throughout the calculation. This method is used in section 4.2.2 for calculating the series expansion of the energy gap of TFIM on a spin-ladder in the low-field regime.

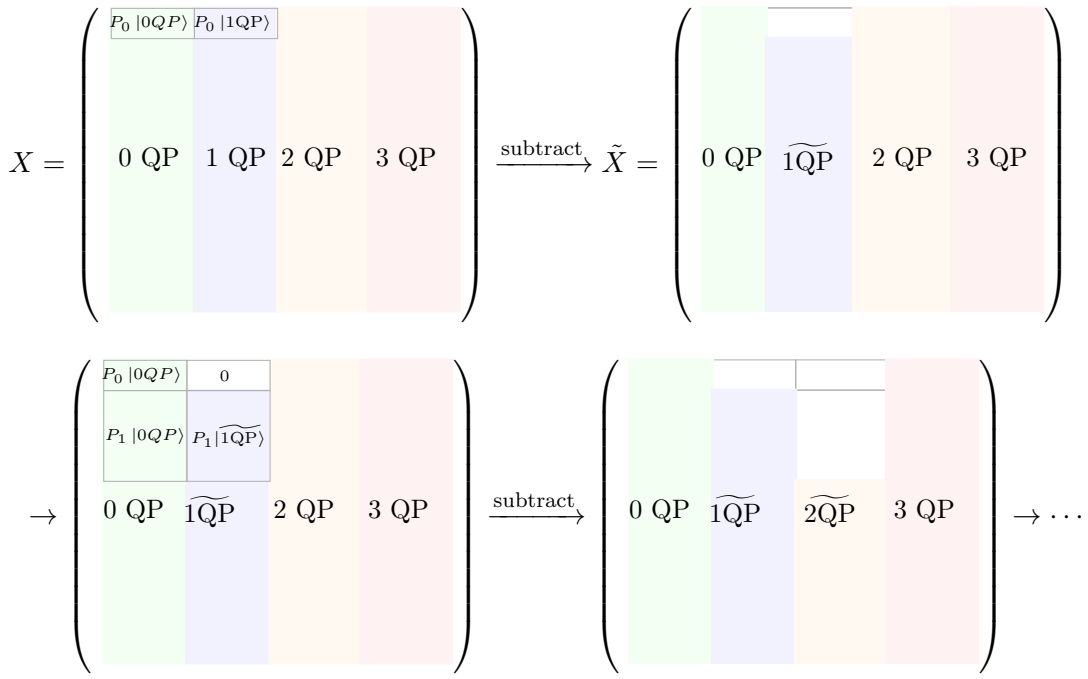

Figure 6: Schematic illustration of PCAT subtraction scheme to achieve a cluster-additive effective Hamiltonian across all blocks. At first, one has to subtract the 0QP contribution from the 1QP vectors such that the $P_0\,|1\mathrm{QP}\rangle = 0$, with $|1\mathrm{QP}\rangle$ denoting an arbitrary 1QP state. As a next step, the same procedure is applied to the 2QP states. However, one also has to subtract the 1QP contributions. A linear combination of all 1QP states from each 2QP state is subtracted, such that $P_1\,|2\mathrm{QP}\rangle = 0$. This scheme is continued for all states. Note that subtraction between two different particle states is only necessary if the states belong to the same symmetry block. For example, in the TFIM model with $\mathbb{Z}_2$ symmetry, subtraction is only necessary between odd and even particle numbers.

2.4. CUT Method

In section 4, we will not only apply PCAT to various models but also use another well-known method, namely continuous unitary transformations (CUT). This method is based on continuously transforming the Hamiltonian. In addition, we will present ideas, which

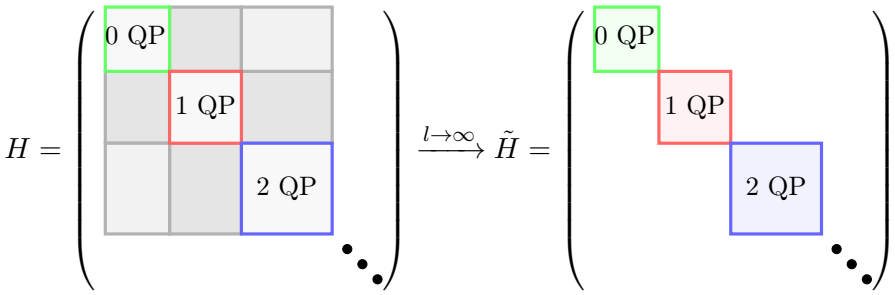

(2.77)

Figure 7: Schematic depiction of the general idea behind CUT-methods. Left: The initial matrix, which is not in block shape. Right: The Matrix becoming block-shaped for the limit $l \to \infty$. Here, the block-form corresponds to a particle conservation.

combine both methods to gain better physical insights. Therefore, the key concepts and ideas behind CUT methods will be provided in the following.

The method of CUT is a widely used method for block-diagonalizing Hamiltonians using a so-called flow equation approach. The main difference between CUT methods and schemes like TBOT and PCAT is that CUT methods can be often applied directly in the thermodynamic limit.
As a first step, an general overview about the basic ideas behind the CUT method is provided (based on [29] and [30]). Next, two concrete CUT based methods are introduced in more detail.

As for every method shown so far, the challenge is to transform a given Hamiltonian $H = H_0 + xV$ into the form of an effective Hamiltonian H_{eff}. Concretely, we want to change the basis in such a way, that the different subspaces of interest decouple. In the framework of CUT methods, this is achieved continuously by defining a unitary transformation $U(l)$, which depends on a continuous parameter l ($l \in \mathbb{R}^+$). Consequently, the transformed Hamiltonian also depends on l:

$$H(l) = U^\dagger(l) H U(l) \qquad \text{with } U(l)^\dagger = U(l)^{-1}. \tag{2.78}$$

The general two boundary conditions for $U(l)$ are as follows: First, for $l = 0$, the transformation should be the identity, i.e.

$$H(l=0) \stackrel{!}{=} H_0 \longleftrightarrow U(l=0) = \mathbb{1}. \tag{2.79}$$

Secondly, as $l \to \infty$, one obtains the effective Hamiltonian

$$H_{\text{eff}} = H(l \to \infty). \tag{2.80}$$

This means that after an infinite number of infinitesimal rotations, all targeted subspaces are decoupled.
In general, every unitary transformation can be expressed as an exponential of an anti-Hermitian operator. Here, we use following expression:

$$U(l) = \mathcal{T}_l \exp\left\{ \int_0^l \eta[H(l)] \right\} \qquad \text{with } \eta(l)^\dagger = -\eta(l), \tag{2.81}$$

with $\mathcal{T}_l$ the l ordering operator. The anti-Hermitian operator η is also called the generator of the transformation. In this context, the generator is a superoperator because it directly depends on the Hamiltonian under study. Consequently, instead of finding the transformation U directly, one has to choose an appropriate generator. Here, *appropriate* means that the off-diagonal elements (i.e., the couplings strengths between the subspaces) should vanish for $l \to \infty$. Based on eq. (2.81), the transformation can be formulated via a flow-equation

$$\frac{\mathrm{d}}{\mathrm{d}l} H(l) = \left[-U^\dagger(l) \frac{\mathrm{d}U(l)}{\mathrm{d}l}, H(l) \right] = [\eta(l), H(l)]. \tag{2.82}$$

As can be seen, after choosing a generator, one only has to solve the system of differential equations. In principle, the set of differential equations is not closed. This means that one has to apply a truncation scheme additionally. As pointed out in [29], the method can be described in three steps:

1. Choose appropriate generator η and truncation scheme
2. Calculate $[\eta, H]$ multiple times for setting up the flow equations
3. Solve differential equations

2.4.1. Directly evaluated epCUT (deepCUT)

A prominent example of CUT methods is the deepCUT method, which will be briefly introduced here. A detailed description can be found in the original paper by Krull et. al [12] and in [31], where the method is used to calculate the energy gap and critical exponents of a bi-layer system.
The whole method makes use of second quantization by expressing the Hamiltonian and generator as a sum of corresponding monomials:

$$H(l) = \sum_i h_i(l) A_i \qquad \text{and} \qquad \eta(l) = \sum_i \eta_i(l) A_i = \sum_i h_i(l) \eta[A_i]. \tag{2.83}$$

Each monomial A_i consists of an unique ordered product of creation and annihilation operators. The generator can be then written as:

$$\eta = \mathrm{sign}(\Delta E_i) A_i, \tag{2.84}$$

with ΔE_i the energy difference with respect to H_0 caused by A_i (quasi-particle generator). By plugging both into the flow-equation yields:

$$\sum_i \partial_l h_i(l) A_i = \sum_{jk} h_j(l) h_k(l) [\eta[A_j], A_k], \tag{2.85}$$

$$\rightarrow \partial_l h_i = \sum_{jk} D_{ijk} h_j(l) h_k(l). \tag{2.86}$$

The single coefficients D_{ijk} are determined by:

$$[\eta[A_j], A_k] = \sum_i D_{ijk} A_i. \tag{2.87}$$

Up to this point, the general CUT scheme has been expressed into second quantization. Regarding to point 2 of the general CUT recipe, we want to specify the truncation of the flow-equation, which is the main difference between all CUT methods in general. For this purpose, we define the minimal and maximum order of the monomials. The minimal order $O_{\min}(A_i)$ of A_i is defined as the order at which A_i arise for the first time. For example, first-order monomials arise from:

$$[\eta[V], H_0] \tag{2.88}$$

and for second-order monomials, one has to calculate commutators like:

$$[\eta[V], V] \qquad [[\eta[V], V], H_0] \qquad [[\eta[V], H_0], [\eta[V], H_0]]. \tag{2.89}$$

The maximum order $O_{\max}(A_i)$ is defined by the following iterative relation

$$O_{\max}(A_j) = \max_{\{i,k | D_{ijk} \neq 0 \vee D_{ikj} \neq 0\}} \{O_{\max}(A_i) - O_{\min}(A_k)\}, \tag{2.90}$$

with the initial conditions

$$O_{\max}(A_i) = \begin{cases} n & \text{if } A_i \text{ targeted} \\ 0 & \text{else} \end{cases} \tag{2.91}$$

Finally, the rules for truncating the flow-equation can be written as:

1. All monoms which satisfy $O_{\min} > O_{\max}$ are discarded
2. All terms D_{ijk} with $O_{\max}(A_i) < O_{\min}(A_j) + O_{\min(A_k)}$ are neglected

The set of differential equations is then solved. The general idea behind this is to extend the formalism of epCUT, which does a series expansion within the terms h_i. In this way, deepCUT is exact up to a given order n. It also have the advantage over epCUT of a greater range of convergence. Compared to NLCE, it becomes apparent that epCUT / deepCUT calculates the targeted quantity directly in the thermodynamic limit, overcoming problems associated with effects using finite clusters in the NLCE framework.
In section 5.1.3, deepCUT is used to calculate the dispersion of the bound-state to compare it with NLCE and the analytic solution.

2.4.2. OS-CUT

Another example of a CUT method is the *one-step CUT* (OS-CUT) method, which is described in [32]. First, we will present the basic idea of the method. As a second step, we will present an idea of M. Hörmann on how this CUT method can be used in combination with PCAT and NLCE.
The idea behind OS-CUT [32] is that every unitary transformation U can be written as $U = e^S$ with $S = \log U$ an anti-Hermitian operator. By introducing a continuous parameter θ (formerly l in the previous subsections), the transformation can be written as [32]:

$$H(\theta) = e^{-\theta S} H e^{\theta S} \qquad \text{with } \theta \in [0, 1]. \tag{2.92}$$

For $\theta = 0$, one gets the initial Hamiltonian. But instead of going to infinity, the effective Hamiltonian is obtained for $\theta = 1$. It can be easily verified that eq. (2.92) is the solution of the flow equation

$$\frac{\mathrm{d}}{\mathrm{d}\theta} H(\theta) = -[S, H(\theta)]. \tag{2.93}$$

The main challenge is to determine the general form of S, which is not obvious for most systems. Nevertheless, this approach has turned out to be very useful in combination with PCAT. In the following section, the basic scheme of how this can be used is explained in more detail. In section 4, specific examples of systems where the method is applied are discussed.

By using the transformation from section 2.3, one can calculate the exact U for any finite cluster. Consequently, one also knows the S for that cluster as well ($S = \log U$). Of course, the matrix elements of S depend on the perturbation parameter x of the problem Hamiltonian $H = H_0 + xV$. Nevertheless, one can directly extract the general shape of the parameterized $S(x)$. For example, considering the Hamiltonian of a dimer:

$$\begin{array}{c} \begin{array}{cccc} \langle 00| & \langle 01| & \langle 10| & \langle 11| \end{array} \\ \begin{pmatrix} 0 & 0 & 0 & x \\ 0 & 2 & x & 0 \\ 0 & x & 2 & 0 \\ x & 0 & 0 & 4 \end{pmatrix} \begin{array}{c} |00\rangle \\ |01\rangle \\ |10\rangle \\ |11\rangle \end{array} \end{array}.$$

By calculating U via pCAT, one can determine the general form of S:

$$S = \begin{pmatrix} 0 & 0 & 0 & \alpha(x) \\ 0 & 0 & 0 & 0 \\ 0 & 0 & 0 & 0 \\ -\alpha(x) & 0 & 0 & 0 \end{pmatrix}. \tag{2.94}$$

In general, $\alpha(x)$ can be determined numerically for every x by calculating $\log U(x)$. For this minimal example, an analytic expression can also be easily obtained. As it is marked

in eq. (2.95), only the vectors associated to the 0QP and 2QP channels have to be rotated for diagonalization. By looking at the finite Hamiltonian

$$H_{\text{dimer}} = \begin{pmatrix} 0 & 0 & 0 & x \\ 0 & 2 & x & 0 \\ 0 & x & 2 & 0 \\ x & 0 & 0 & 4 \end{pmatrix}, \tag{2.95}$$

one sees, that only the subspace regarding to 0 and 2 quasi particles needs to be decoupled. The corresponding eigenvectors can be expressed as:

$$|\psi\rangle_{0\text{QP}} = \cos\frac{\theta}{2}|00\rangle + \sin\frac{\theta}{2}|11\rangle, \tag{2.96}$$

$$|\psi\rangle_{2\text{QP}} = -\sin\frac{\theta}{2}|00\rangle + \cos\frac{\theta}{2}|11\rangle. \tag{2.97}$$

From this form, the unitary transformation U takes the expected form of a rotation-matrix in two dimensions:

$$U = \begin{pmatrix} \cos\frac{\theta}{2} & \sin\frac{\theta}{2} \\ -\sin\frac{\theta}{2} & \cos\frac{\theta}{2} \end{pmatrix}. \tag{2.98}$$

Furthermore, we know:

$$e^S = \exp\left\{\begin{pmatrix} 0 & \alpha(x) \\ -\alpha(x) & 0 \end{pmatrix}\right\} = \begin{pmatrix} \cos\alpha & \sin\alpha \\ -\sin\alpha & \cos\alpha \end{pmatrix}. \tag{2.99}$$

By comparing eq. (2.98) and eq. (2.99), one obtains $\alpha = \frac{\theta}{2} = \frac{\arctan x}{2}$.
Since S is cluster-additive, equation eq. (2.92) can be evaluated in the thermodynamic limit. As a truncation scheme, we only include terms that not exceed order n. The resulting Hamiltonian $H(\theta)$ is plugged into the flow-equation again, but this time, the whole equation is integrated over θ, resulting in

$$H(1) - H(0) = -\int_0^1 [S, H(\theta)]\mathrm{d}\theta. \tag{2.100}$$

For the commutator $[S, H(\theta)]$, one allows terms, which belong to order $n+1$. Since $H(0) = H_0$, we can directly determine H_{eff} from $H(1)$. As will be shown in the examples, this scheme allows us to calculate higher orders using S from lower ones. This observation is in alignment with [33] and [34], which states, that one can get order of $2n+1$ of the energy by calculating the eigenstates up to order n.

2.5. Numerical implementation of modified OS-CUT

The modified OS-CUT method described in the previous section is based on determining S in second quantization and setting up as well as solving the differential equations. To simplify these steps, we want to describe a numerical method that also builds on the

OS-CUT scheme and was developed by M. Hörmann as well.
In the previous method, the quantity

$$\int_0^1 [S, H(\theta)] \tag{2.101}$$

was calculated in the thermodynamic limit for a given S. The goal now is to calculate the same quantity based on finite Hilbert spaces, or, in other words, to calculate the quantity using a cluster expansion. To achieve this, we consider a Hamiltonian H defined on N sites and a set of generators S_{C_i}. Each generator S_{C_i} is calculated from finite subclusters C_i. Since S_{C_i} is cluster-additive, it is possible to construct an S for the entire system with N sites by embedding the reduced generators $\tilde{S}_{C_i}$. From this S one obtains an approximate transformation for the effective Hamiltonian on the finite system. By using the general relation from the OS-CUT scheme:

$$H(\theta) = e^{-S\theta} H e^{S\theta} \tag{2.102}$$

$$\partial_\theta H(\theta) = [S, H(\theta)] \tag{2.103}$$

one obtains:

$$H_{\text{int}} = \int_0^1 e^{-S\theta} H e^{S\theta} \mathrm{d}\theta, \tag{2.104}$$

with H_{int} being cluster-additive, because S is cluster-additive. Therefore, the transformation $e^{-S\theta}$ results into an approximate transformation that is block-diagonal in terms of disjoint clusters. In a last step, one embeds S and H_{int} onto an larger cluster of size N' and calculates:

$$H_{\text{diff}} = [H_{\text{int,embedd}}, S_{\text{embedd}}], \tag{2.105}$$

with $H_{\text{int,embedd}}$ and S_{embedd} being the embedded quantities H_{int} and S on the system with size N'. Since every S_{C_i} is connected with a process on the real lattice up to a maximum length scale, one has to choose N' large enough to avoid unwanted boundary effects. As S and $H_{\text{int,embedd}}$ being cluster-additive, also H_{diff} is cluster-additive.
The method can be divided into three steps:

1. Calculate S_{C_i} and the corresponding reduced values $\tilde{S}_{C_i}$
2. Do an cluster-expansion of $H_{int,i}$ by embedding $\tilde{S}_{C_i}$ on the cluster with size N_i
3. Embed all $H_{int,i}$ onto an sufficient large cluster with size N' and calculate H_{diff}

2.6. Extrapolations

Describing a physical quantity by a perturbative series expansion often faces the issue that the region of interest lies outside the convergence radius of the series. For instance, we will mainly calculate the series expansion of the energy gap to determine the critical point x_c where the gap closes (indicating a second-order phase transition). Therefore, the radius of convergence of the series should be at least up to x_c, which is not always the

case. Since such problems are well known in perturbation theory, there are various ways of summing the series in order to extract further information. Well-known examples are the Euler summation and the Borel summation. The downside of these methods is, that one has to need to know all terms of the series, which we do not know for our systems. For our kind of problem a method, called *Padé extrapolation*, which approximates the (finite) series outside the convergence radius is used. In the following this kind of technique is explained more in detail. The section is based on [35] and [36].

Formally, a Padé extrapolation for a finite series $p(x) = \sum_{n=0}^{r} c_n x^n$ is defined as:

$$P[p,q](x) = \frac{P_p(x)}{Q_q(x)} = \frac{p_0 + p_1 x + \cdots + p_l x^p}{q_0 + q_1 x + \cdots + q_q x^q}, \tag{2.106}$$

with the coefficients $p_i, q_i \in \mathbb{R}$. The idea behind such an extrapolation is to rewrite the power series as a rational function, with the condition, that the Taylor expansion of $P[p,q](x)$ up to order $r = p+q$ matches the original series $p(x)$. This boundary condition can be expressed as

$$\frac{\mathrm{d}^k}{\mathrm{d}x^k} P[p,q]\Big|_{x=0} \stackrel{!}{=} \frac{\mathrm{d}^k}{\mathrm{d}x^k} p(x)\Big|_{x=0} = k! c_k \tag{2.107}$$

for every $k \in \{0, 1, \cdots, p+q\}$, which determines the coefficients p_i and q_i. The values of p and q can be chosen freely, as long as $p + q = r$ is satisfied. In principle, there is no rule which combination of p and q continues the series best. However, experience has shown that Padè extrapolations with q and p close to each other generally extrapolate the series better.

Due to the rewriting of the series as a rational function, singularities ($Q_q(x_s) = 0$) may appear. Since we are only considering second-order phase transitions, such singularities are unphysical (often called as defective). For the case that $x_s < x_c$, the specific Padè extrapolation can be discarded.

Another important extrapolation method is the so-called *dlog-Padé* method, which is closely related to the Padè extrapolation. The general definition is that the dlogPadè extrapolation is the above-defined Padè extrapolation of the logarithmic derivative of the initial series $p(x)$:

$$D(x) = \frac{\mathrm{d}}{\mathrm{d}x} \ln p(x) = \frac{p(x)'}{p(x)} \xrightarrow{\text{Pade extrapolation}} P[p,q]_D = \frac{P_p(x)}{Q_q(x)} \tag{2.108}$$

with P_p and Q_q defined as above. Due to the derivative in the numerator, one looses one information which leads to the condition of $p + q = r - 1$. The extrapolant of the initial series $p(x)$ can be written as

$$dP[p,q]_p(x) = \exp\left\{ \left(\int_0^x \frac{P_p(x')}{Q_q(x')} \mathrm{d}x' \right) \right\}. \tag{2.109}$$

The advantage of this way of determining the extrapolation is that it allows the extraction of critical exponents. For second-order phase transitions, it is known that a power-law behavior exists in the vicinity of the energy gap, as

$$\Delta \propto |x - x_c|^\theta, \tag{2.110}$$

with the critical exponent $\theta = z\nu$ as the product of the dynamical critical exponent z and the correlation length critical exponent ν. At the critical point x_c, the dlog-Padé faces a pole. Therefore, to determine x_c, one needs to evaluate the zeros of the polynomial $Q_q(x)$. In general, it is also possible for a non-physical pole to appear in the dlogPadè method.
To also extract the critical exponent θ, the function $f(x)$ is defined:

$$f(x) = \big(1 - \frac{x}{x_c}\big)^{-\theta}. \tag{2.111}$$

The derivative of $f(x)$ leads to

$$\frac{\mathrm{d}}{\mathrm{d}x} \ln f(x) = \frac{\theta}{x_c - x}, \tag{2.112}$$

with a pole at x_c. With that, the critical exponent is determined by

$$\theta = \frac{P_p(x)}{\frac{\mathrm{d}}{\mathrm{d}x} Q_q(x)}\Big|_{x=x_c}. \tag{2.113}$$

3. Avoided level crossings and exceptional points

3.1. General description

The main idea of NLCE is to use cluster-additivity to approximate physical quantities in the thermodynamic limit by calculating corresponding processes on finite clusters. The transformation T, which is used to bring the finite Hamiltonians into an effective form, is based on the exact eigenvectors of the system. This means that to calculate, for example, the hopping amplitudes for the first excitation, the exact eigenstates associated with this particle block are required. Because the change of the eigenvectors for sufficiently small steps Δx is smooth, one approach is to follow the eigenstates adiabatically. However, when performing calculations on finite systems, the problem of *artificial avoided level crossings* (see fig. 8) between different particle blocks can emerge. In this context, artificial means that these avoided crossings are artifacts of the finite system, as they do not exist in the infinite lattice. This effect can be motivated by the von-Neumann Wigner theorem [37], which generally states that states belonging to the same symmetry sector do not cross (non-crossing rule). For real symmetric matrices, at least two parameters are necessary to get a crossing, which is not satisfied in our problems since H depends only on $x \in \mathbb{R}$. These artificially avoided crossings do not exist in the thermodynamic limit, as the different states are protected by symmetries (different quantum numbers) or are sufficiently gapped [38]. Besides this, also non-artificial avoided-crossing can be present on clusters. In this case, the avoided-crssoing is connected to a fundamental physical property of the system in the thermodynamic limit [39].
Since our transformation depends on the choice of the *correct states*, the crucial question is what those correct states are. Here, the term *correct states* refers to states (not necessarily eigenstates) that carry the information about the processes of the corresponding particle dynamics in the thermodynamic limit. However, an adiabatic state generally does not fulfill this condition in the presence of an artificial avoided crossing. Consequently, to perform a cluster expansion for the target quantity, it is essential to identify the appropriate states. It is therefore of great interest to find a general solution to this problem, which has not yet been done. For this reason, the problem will be further discussed in more detail and under different points of views. Besides, some ideas are proposed that could be used to approach a workable framework.
In general, the problem of choosing the appropriate states is a common problem in the field of effective Hamiltonians. Especially in quantum chemistry, this issue is also known as intruder-state problem. The problem is always that there is a large coupling between the model space (space containing the states coming from the zero order of H, denoted as $H^{(0)}$) and the corresponding complementary, leading to divergence in the series expansion [40]. To get a better understanding, it is helpful to take a look at the first order of Rayleigh-Schrödinger perturabtion theory:

$$\left|n^{(1)}\right\rangle = \sum_i \frac{\langle\phi| V \left|n^0\right\rangle}{E^{(0)} - E_{\phi_i}} \phi_i = \sum_i M_i \phi_i \tag{3.1}$$

with $H^{(0)}\left|n^{(0)}\right\rangle = E^{(0)}\left|n^{(0)}\right\rangle$ and $H^{(0)}\left|\phi_i\right\rangle = E_{\phi_i}\left|\phi_i\right\rangle$. If $E^{(0)} - E_{\phi_i} \to 0$, a singularity is obtained, since $M_i \to \infty$ [41]. Of course, divergences appear normally at higher orders and cause a break-down of the perturbation series. The direct connection to the avoided crossing is, that there the overlap between the adiabatic n particle eigenstates with the m particle states increases. The reason is, that both eigenvectors form a superposition in the vicinity of an avoided intersection point. In other words, the weight of the intruder state (repulsed state) in the projected P-space got higher. In the case of the intruder states, Malrieu et. al. proposed in [40] an intermediate Hamiltonian, which contains not only exact eigenstates but also modified ones. In the more recent paper by Cöster et al. ([38]), the correct state was gained by modifying the CUT scheme such that an appropriate superposition of the intruder-state and the adiabatic state in the vincinity of the artificial avoided-crossing is chosen. Similarly, we attempted to find a way, how to choose the diabatic states at artificial avoided-level crossings, since they should contain the information about the system in the thermodynamic limit. However, it remains unclear, if performing a diabatic transition is sufficient to do NLCE beyond such avoided-crossings. As it is shown later, there are hints, that choosing the diabatic eigenstates may lead to fewer problems.
Especially for the type of problems of the form $H_0 + xV$, we can look at the avoided crossings from a different angle. As it turned out, the occurrence of avoided crossings is also closely related to singularities in the complex x-plane. In [42] it is shown that each point of level-repulsion is connected to such a singularity, called *exceptional point*. As mentioned above in the context of intruder states, these exceptional points limit the radius of convergence of the perturbative series, with the convergence radius $r = \min_i |x_{\mathrm{EP},i}|$ and $x_{\mathrm{EP},i}$ being all EPs in the system [43]. To obtain information in the perturbative case for $x > x_{\mathrm{EP}}$ one would be dependent on extrapolation methods like Padè extrapolations (see section 2.6). Consequently, by solving the problem with NLCE it would be possible to calculate e.g. the gap beyond the perturbative limit.

A mathematical definition of EPs is that they are the points in the complex plane where two or more eigenvalues and their corresponding eigenstates coalesce. For more than two eigenstates, these are denoted as EPs of order N, with N the number of the involved eigenstates. In the case of second order EPs, the mathematical definition can be expressed as

$$\det(H(x) - \lambda) = 0, \tag{3.2}$$

$$\partial_\lambda \det(H(x) - \lambda) = 0. \tag{3.3}$$

Consequently, near an EP, the corresponding eigenvalue and eigenvector takes the following form

$$E(x) = E_{\mathrm{EP}} + \sum_{m=1}^{\infty} c_m \sqrt{x - x_{\mathrm{EP}}}^m, \tag{3.4}$$

$$|\psi(x)\rangle = |\psi_{\mathrm{EP}}\rangle + \sum_{m=1}^{\infty} |\phi_m\rangle \sqrt{x - x_{\mathrm{EP}}}^m, \tag{3.5}$$

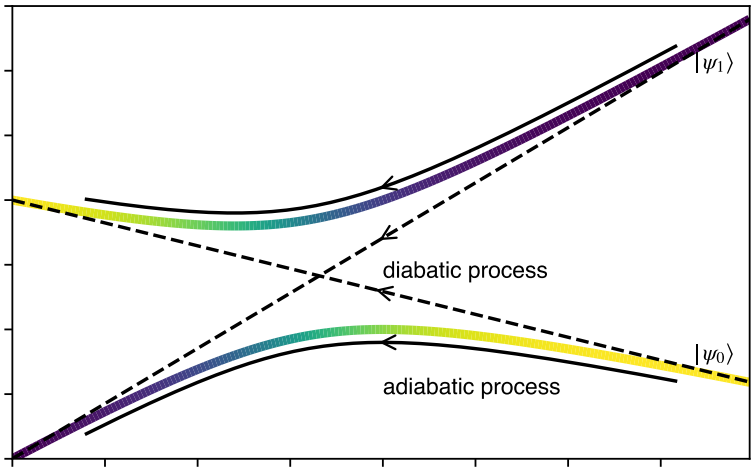

Figure 8: Illustrative sketch of an avoided-level crossing / level repulsion of a two level system. The dashed lines symbolizes the diabatic process, sketch similar to [44].

with $|\psi_{\mathrm{EP}}\rangle$ and E_{EP} denoting the state and energy at $x = x_{\mathrm{EP}}$. As can be seen, the energy has a characteristic square-root behaviour, $(E(x) - E_{\mathrm{EP}}) \sim \sqrt{x - x_{\mathrm{EP}}}$ (see fig. 10). Furthermore, at $x = x_{\mathrm{EP}}$, the matrix is no longer diagonalizable, since the matrix takes a Jordan-block structure:

$$\begin{pmatrix} E_{\mathrm{EP}} & 1 \\ 0 & E_{\mathrm{EP}} \end{pmatrix} \tag{3.6}$$

The generalization of higher order EPs can be found in [45]. Beside this, EPs also have topological properties, which we want to introduce by looking at a toy matrix:

$$H = \begin{pmatrix} 0 & V \\ V & -1 \end{pmatrix} \tag{3.7}$$

with $V = \frac{2}{\sqrt{2}}x$. Actually, this Hamiltonian corresponds to one symmetry sector of the XXZ model on a three-site chain. The corresponding eigenvalues and eigenvectors are

$$E_+ = -\frac{1}{2} + \frac{1}{2}\sqrt{1 + 4V^2}, \tag{3.8}$$

$$E_- = -\frac{1}{2} - \frac{1}{2}\sqrt{1 + 4V^2} \tag{3.9}$$

$$\tag{3.10}$$

and

$$v_+ = \begin{pmatrix} \frac{1+\sqrt{1+4V^2}}{2V} \\ 1 \end{pmatrix} \qquad v_- = \begin{pmatrix} \frac{1-\sqrt{1+4V^2}}{2V} \\ 1 \end{pmatrix}. \tag{3.11}$$

At the points $V = \pm\frac{i}{2}$, both eigenvalues have the same value $E_\pm = \frac{1}{2}$ and the eigenvectors also coalesce ($v_1 = v_2$), indicating that the system has two EPs at $V = (0, \pm\frac{i}{2})$ or

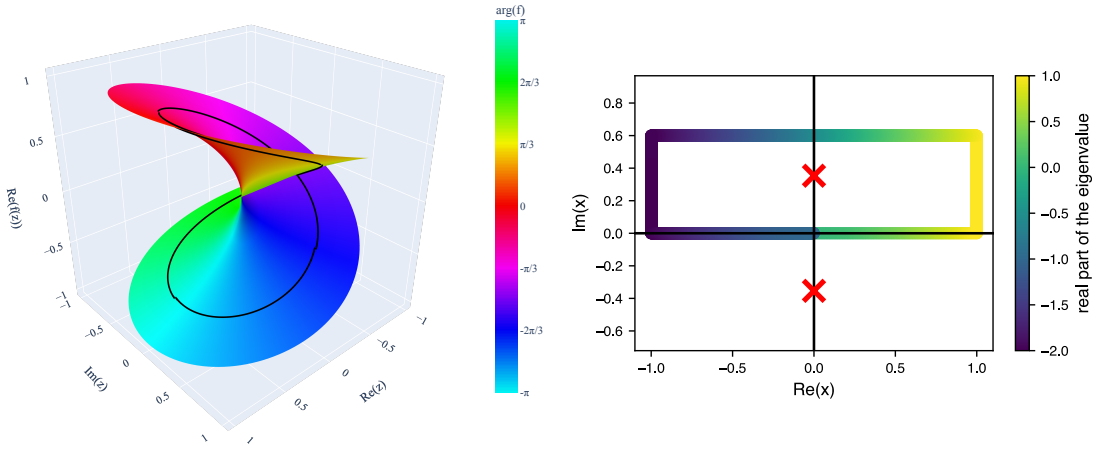

Figure 9: Left: Riemann surface of $\sqrt{x}$ with $x \in \mathbb{C}$. The black-line shows a circle around $(0,0)$ in the complex plane, plot generated based on [46]. Right: Path in the complex plane of the toy Hamiltonian. The real part of the eigenvalues are color coded and the location of the EPs are marked as red crosses.

$x = (0, \pm\frac{i}{\sqrt{8}})$. By encircling the EP adiabatically, the eigenvalues exchange (see fig. 9). This general (topological) property of EPs can be demonstrated here by defining the path as $V(\theta) \to \frac{i}{2} + Re^{i\phi}$ for $R > 0$. Plugging this into the square-root term, one obtains

$$\sqrt{1+4V^2} = \sqrt{4R^2 e^{\mathrm{i}2\phi} + \mathrm{i}4Re^{\mathrm{i}\phi}} \tag{3.12}$$

$$= 2\sqrt{R}e^{\mathrm{i}0.5\phi}\sqrt{\mathrm{i}}\sqrt{1-\mathrm{i}Re^{i\phi}}. \tag{3.13}$$

The last term here is a square-root term defined in the complex plane. Since the square-root is a multi-valued function, it is defined on the *Riemann surface* in such a way that it is holomorphic. In fig. 9, the Riemann surface is shown for the simple square-root function $\sqrt{z}$, with $z \in \mathbb{C}$ [47]. The phase of the function is encoded into the color and the black line denotes a circular path around the origin $(0,0)$. By following the line one sees, that after one round (2π), one reaches a point corresponding to the negative of its initial value. After going around once more, the function returns to the starting point. For eq. (3.12), this implies that the sign swaps after completing one loop, $\theta = 0 \to \theta = 2\pi$. Something similar can be observed for the eigenvectors. The eigenvectors of the Hermitian system $(x \in \mathbb{R})$ can be rewritten as

$$|\Psi_+\rangle = \cos\frac{\theta}{2}|0\rangle + \sin\frac{\theta}{2}|1\rangle \tag{3.14}$$

$$|\Psi_-\rangle = -\sin\frac{\theta}{2}|0\rangle + \cos\frac{\theta}{2}|1\rangle, \tag{3.15}$$

with $\theta = \arctan 2V$. By encircling the origin of arctan n-times, an additional offset of $n\pi$ emerges. As a result, encircling leads to $\theta \to \theta + \pi$ [48] and consequently $\cos(\theta/2) \to \pm\sin(\theta/2)$ and $\sin(\theta/2) \to \mp\cos(\theta/2)$. This means, that the eigenvectors switch and one eigenvector gets an additional (geometric) phase, known as the Berry phase [49]. In particular, one can display it as [50]

$$\begin{pmatrix} |\psi_1\rangle \\ |\psi_2\rangle \end{pmatrix} \xrightarrow{\circlearrowleft} \begin{pmatrix} |\psi_2\rangle \\ -|\psi_1\rangle \end{pmatrix} \xrightarrow{\circlearrowleft} \begin{pmatrix} -|\psi_1\rangle \\ -|\psi_2\rangle \end{pmatrix} \xrightarrow{\circlearrowleft} \begin{pmatrix} -|\psi_2\rangle \\ |\psi_1\rangle \end{pmatrix} \xrightarrow{\circlearrowleft} \begin{pmatrix} |\psi_1\rangle \\ |\psi_2\rangle \end{pmatrix}. \tag{3.16}$$

Consequently, one would need to go at least 4 times around an exceptional point to restore the initial states exactly.

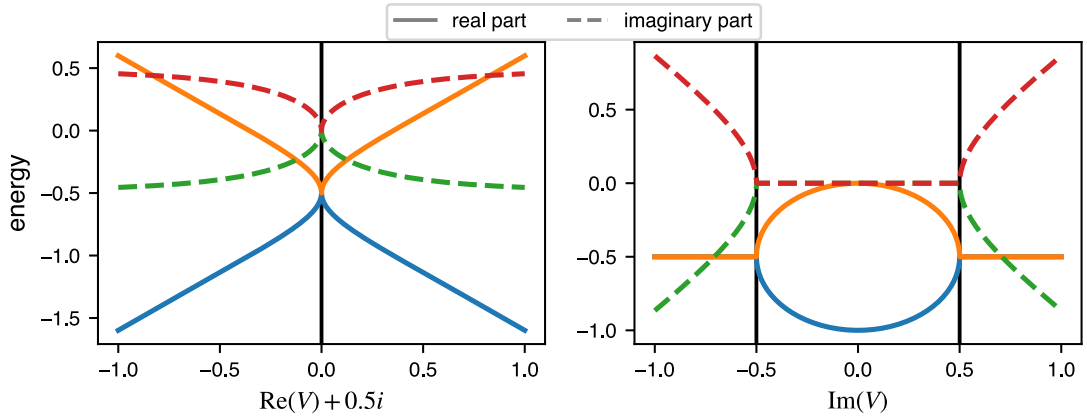

Figure 10: Energy spectra for the toy Hamiltonian (eq. (3.7)) for different x values. Left: square-root behaviour near the exceptional point $V = 0.5$i. Right: Spectra for $\mathrm{Re}(V) = 0$.

3.2. Embedding of S as an Ansatz

Overcoming the problem of artificial avoided level crossings is generally difficult, and a universal solution is not yet known. However, one can state that it requires either changes in the cluster expansion or changes regarding the transformation T itself. Here, we focus on the latter approach. Before going into details, we want to point out that K. Cöster ([38]) partially overcame the avoided crossing by also modifying the transformation. In his proposed approach, the CUT scheme was modified in a way that the decoupling between the different blocks was done up to a sufficient point to prevent the adiabatic transition. After that, further decoupling was done with a modified generator. Additionally, a weight $W_i = \langle i|i\rangle$ was introduced, where i labels the corresponding level. On the physical side, this weight unsures that for $x < x_{\mathrm{avoided-crossing}}$, most of the weight is on the adiabatic states. In the region around the artificial repulsion ($x \approx x_{\mathrm{avoided-crossing}}$), the weight gradually transfers to the corresponding diabatic state, until only the diabatic state is considered for $x > x_{\mathrm{avoided-crossing}}$. Since our transformation does not depend on

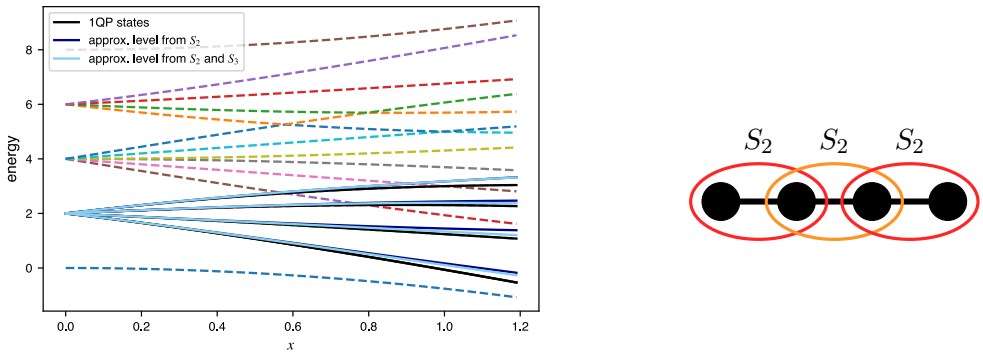

Figure 11: Approximating the energy levels by constructing T out of S from smaller clusters. The dotted lines in the spectra are obtained by ED calculations.

flow equations but rather on the exact states, we use a different approach, which follows the same idea of finding the correct diabatic transition.
To achieve this, we use information contained in $S = \log T$. The general idea is to calculate S for clusters that do not exhibit avoided crossings with respect to the particle blocks under investigation. Afterwards, the S is used to construct approximate eigenvectors by embedding S onto the cluster. This can be done because S fulfills cluster additivity (see section 2.3), so we can always write

$$S = S_A \otimes \mathbb{1} + \mathbb{1} \otimes S_B, \tag{3.17}$$

for A and B as disjoint clusters ($A \cap B = 0$). For example, for a 4-site cluster, the approximate S constructed from dimers can be written as follows (see also fig. 11):

$$S = S_2 \otimes \mathbb{1}_2 + \mathbb{1} \otimes S_2 \otimes \mathbb{1} + \mathbb{1}_2 \otimes S_2 \tag{3.18}$$

The effective Hamiltonian is approximated by $\tilde{H}_{\text{eff}} = e^{-S} H e^{S}$. Since S is only an approximation of T, the resulting Hamiltonian is not fully block-diagonal. Small off-diagonal coupling elements still exist, such that the Hamiltonian looks like

$$\tilde{H}_{\text{eff}} = \begin{pmatrix} \text{Block } H_A & H_{B,A} \\ H_{A,B} & \text{Block } H_B \end{pmatrix}, \tag{3.19}$$

with the off-diagonal coupling elements $H_{A,B}$ and $H_{B,A}$. Nonetheless, as shown in fig. 11, the resulting 1QP energy values approximate the actual ones quite well for small x values. Of course, using the trimer as well for constructing S would improve accuracy. As usual for embeddings, contributions from smaller clusters have to be subtracted to avoid double counting. In particular, this means for the given example:

$$S_{3,\text{red}} = S_3 - \mathbb{1} \otimes S_2 - S_2 \otimes \mathbb{1} \tag{3.20}$$

$$\Rightarrow S = S_{3,\text{red}} \otimes \mathbb{1} + \mathbb{1} \otimes S_{3,\text{red}} + S_2 \otimes \mathbb{1}_2 + \mathbb{1} \otimes S_2 \otimes \mathbb{1} + \mathbb{1}_2 \otimes S_2. \tag{3.21}$$

The way the approximate eigenvectors are used here is that they serve as an projector to determine the exact 1 QP eigenvectors without adiabatic tracking. The next section presents the results of embedding S into a system with avoided level crossings, demonstrated through a concrete example.

3.3. Example: linear cluster with additional spin

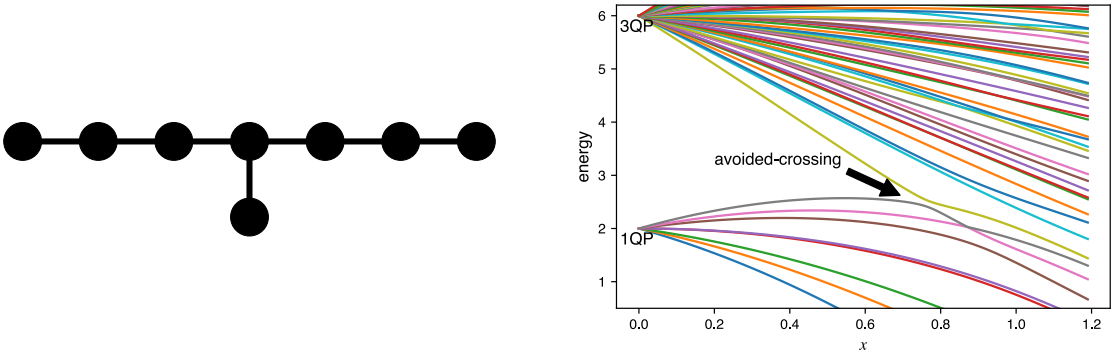

Figure 12: Left: cluster of a linear chain with an additional spin. Right: Corresponding spectra of the 1QP and 3QP block. The avoided crossing between these two blocks is marked by the arrow.

As described above, S can be used to approximate the energy levels and determine the diabatic transition in a systematic way. To study the behaviour of this idea in context of avoided crossings, we consider the finite system from fig. 12. As can be seen from the spectra (right side), a clear avoided-level crossing between the highest 1QP and the lowest 3QP band occurs for $x \approx 0.8$. If the states are followed adiabatically, the corresponding transformation will break down. To demonstrate this, one can calculate the energy spectra for the red-marked part of the transformation

$$T_n = \sum_{k \in s_n} X_{i,k} \left(X_{s_n}^{P_n \dagger} \left(X_{s_n}^{P_n} X_{s_n}^{P_n \dagger} \right)^{-1/2} \right), \tag{3.22}$$

with the matrix $X_{s_1}^{P_1}$ containing the 1QP entries of the corresponding states. The lowest eigenvalue (fig. 13) shows a fast decaying behaviour around the avoided-crossing, which would lead to divergent behaviour of the transformation. To get the diabatic states, we used the approximate 1QP states as a projector. In comparison, the diabatic transition prevents such a fast decay, which makes the transformation stable. That we actual obtained the diabatic transitions through the approximate transformation can be clearly seen in the energy spectra of the Hamiltonian: around the avoided crossing, the corresponding state jumps up to the diabatic ones (fig. 13).

To gain another perspective, one can also calculate the series expansion of the 1QP block via TBOT. By calculating it to high orders one can approximately determine the

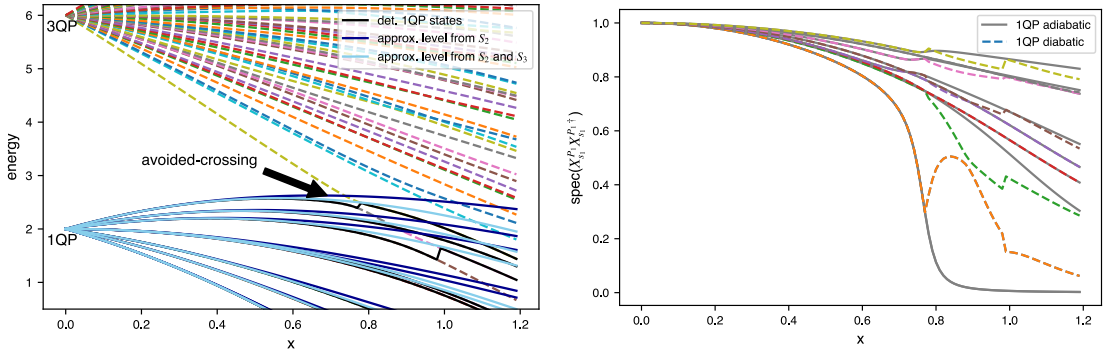

Figure 13: Left: Energy-spectra of the modified linear cluster. Both the corresponding approximated levels and the diabatic transition is shown. The dashed lines are the energy levels determined by ED calculations. Right: Energy spectra of $X^{P_1}_{s_1} X^{P_1}_{s_1}$ is shown for the adiabatic and diabatic states. For the latter one, the fast-decay could be avoided partly.

convergence radius of the corresponding series, as it is shown in fig. 14. Here, one can see, that the position where the series breaks down, corresponds well with the area of the diabatic transition determined by the embedding of S. In other words, this nicely illustrates what was mentioned above, namely that the convergence radius is determined by avoided level crossings which are associated with singularities in the complex plane (see fig. 14).

Here, we want to note that this only presents an idea of how a diabatic transition at an artificial avoided crossing can be achieved. However, to perform a cluster expansion, one would need a smooth transition, like in the gCUT scheme [38]. Thus, the discontinuity which is present by using the approximate states as a projector to the exact eigenstates is unsuitable. Nevertheless, it shows that using S is highly effective for identifying the most suitable eigenvectors, and it is hoped that this finding can be applied in a more general framework. Remaining questions are also if embedding of S also helps to distinguish between artificial avoided crossing and actual avoided crossings, which are determined by the system properties.

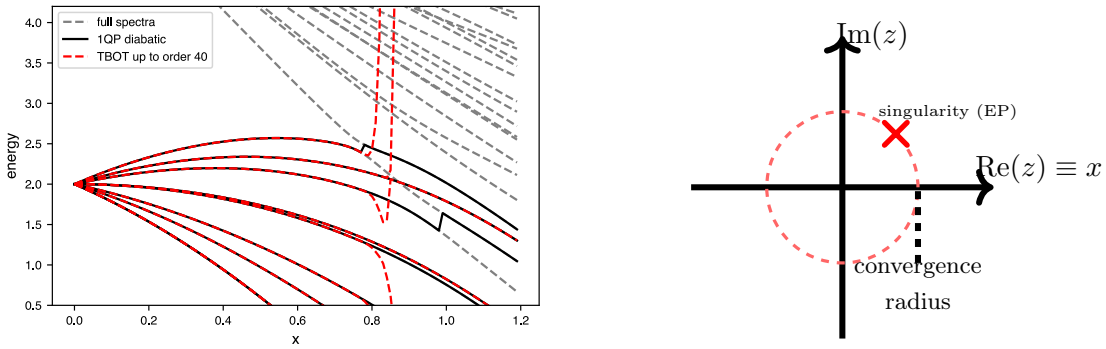

Figure 14: Left: Spectra of the modified cluster of a linear chain. The black lines shows the diabatic transition, the red curves show the result based on TBOT calculations up to order 40. As it can be seen, the series diverges around the avoided crossings / diabatic transitions. Right: schematic picture how the singularity in the complex plane influence the convergence radius.

4. Lattice Geometries

In the following, we studied the transverse field Ising model on different kinds of lattice stripes, namely the *linear chain*, *spin ladder*, *saw-tooth chain*, *triangular strip*, and *cross-stitch ladder*. Hence, we only consider systems with translational symmetry along one axis. In particular, the third and fourth kind of lattice was also studied in detail in the master thesis of Leon Schiller ([51]) by using pCUT. The general advantage of these types of systems is that the computational effort can be reduced by using a cluster expansion with regard to the unit cells of the respective cluster.

4.1. Linear Chain

As a first model, the TFIM on a linear chain is considered with the Hamiltonian in the high-field limit:

$$H = \sum_i \left(1 - \sigma_i^z\right) + x \sum_i \sigma_i^x \sigma_{i+1}^x, \tag{4.1}$$

which reads in second quanitziation (Mastsubara-Matsuda transformaion, see eq. (2.3))

$$H = \sum_i b_i^\dagger b_i + x \sum_i \left(b_i^\dagger b_{i+1}^\dagger + b_i^\dagger b_{i+1} + \text{h.c.}\right). \tag{4.2}$$

This model has the special property of being analytically solvable (integrable model) by mapping the hard-core bosons onto spinless fermions via a Jordan-Wigner transformation. The resulting Hamiltonian can then be solved by applying the Bogoliubov transformation (see detailed description in [52]). For the energy gap, one obtains:

$$\Delta(x) = 2 - 2x, \tag{4.3}$$

with a critical point (second-order phase transition) at $x_c = 1$. Indeed, the location of the critical point is a direct consequence of the system's *self-dualtiy*. This means that the particle description in the low-field limit (ordered phase) and in the high-field limit (disordered phase) can be mapped onto each other. In fig. 15 for both cases the elementary excitations are shown. The consequence of this mapping is that the Hamiltonian obeys the following relation

$$H(x) = xH(x^{-1}), \tag{4.4}$$

which directly leads to the critical point at $x_c = 1$ [53]. The fact that the energy dispersion is exact in first order makes it an ideal testing ground for the methods described in section 2, with regards to their convergence and the critical behaviour.
In the following, a few more comments will be made on some properties before the energy gap is calculated using NLCE. Secondly, results obtained with deepCUT and OS-CUT are presented, focusing on the difference to NLCE.

Figure 15: Left: domain wall as fundamental excitation in low-field limit. Right: spin flip as fundamental excitation

4.1.1. NLCE and critical behaviour

For the cluster expansion, we use the canonical choice as displayed in fig. 16. Since the energy gap is exact up to first order, all information about the energy gap is already present on the dimer (subgraph C_2). For perturbative methods like TBOT, this means that we only have to calculate the series on the dimer and that contributions from higher clusters would cancel out up to the corresponding order.
For applying NLCE, one can insert the eigenvectors of the subgraphs directly into eq. (2.47) without the subtraction scheme, since the ground state and first-particle excitation are protected by the $\mathbb{Z}_2$ symmetry. Unlike perturbative methods such as TBOT, NLCE leads to an energy gap that does not recover the exact result but converges to it as the number of subgraphs is increased, see fig. 17. Comparing it with ED, this results in a faster convergence, since smaller systems are sufficient to get a qualitatively better result, which underlines the strengths of the cluster expansion ansatz. The deviation between NLCE calculations and the exact solution originates from taking all orders from each cluster into account. Thus, terms are considered that would be discarded in a perturbative approach. This effect is enhanced by an imbalance between the order of the ground state and the excited state on each cluster. Concretely, the order of the excited states scales linearly with the number of bonds p, whereas the ground state scales with twice the number of bonds [53]. Considering a cluster with 5 sites, one would have contributions for the excitation energy up to order 4, but the ground-state energy up to order 8. In the framework of NLCE, this imbalance leads to additional terms that do not cancel out.

Figure 16: Cluster expansion of the linear chain.

As a next step, the scaling behaviour of NLCE is investigated in more detail, with a focus on extracting critical exponents. Knowledge of the critical exponents of a system is crucial, because based on them, it can be classified into universality classes. This classification is important, as models within the same universality class share common physical properties. Near phase transitions, physical quantities behave in terms of a power law, for example near the critical point x_c, the energy gap (mass gap) scales as

$$\Delta \propto |x - x_c|^{z\nu}, \tag{4.5}$$

with $z\nu$ the critical exponent. In addition to the vanishing energy gap, the correlation length ξ also diverges. Physically, this means that microscopic configurations are no longer important anymore, rather, the system can be characterized by macroscopic properties. The corresponding power-law behaviour is

$$\xi \propto |x - x_c|^{\nu}, \tag{4.6}$$

with the critical exponent ν. Both quantities, the energy gap and the correlation length are connected via:

$$\Delta \propto \xi^{-z}, \tag{4.7}$$

with z the dynamical critical exponent. In general, these power laws are only valid in the thermodynamic limit. However, even with calculations on finite system sizes, one can extract the critical exponent by using finite-size scaling. One of the main difference between a finite system and the thermodynamic limit with respect to the critical behaviour is that the correlation length remains finite and its value can be associated with the lattice size L. Based on eq. (4.8), one can write:

$$\Delta(x_c, L) \propto L^{-z}. \tag{4.8}$$

Consequently, for small energy gaps, larger system sizes are necessary to capture the relevant processes. Applying eq. (4.8) to the ED calculation, one obtains $z \approx 1$ (fig. 17), which is in alignment with the theoretical values of $z = 1 = \nu$ [4]. The gap calculated via NLCE should also be influenced by the finite correlation length, as the idea of NLCE is to truncate based on correlation lengths (take only processes up to a certain length scale into account). Therefore, the scaling of the NLCE data at both $x = 1$ and the critical value x_c is shown in fig. 17. As the length scale, the number of bonds of the largest included graph in the NLCE calculation is taken:

$$\mathcal{L}(\Delta_{C_i}) = i - 1, \tag{4.9}$$

where Δ_{C_i} represents the NLCE calculation with C_i the largest considered cluster with i sites. The general trend of the data points appears to be linear, but the resulting critical exponent (≈ -1.2) deviates significantly from the expected result of -1. The result also does not improve, if only the calculations with higher length scale are included. Therefore, it was tested what happens if different length scales are assigned to the data points. For this, it was assumed that

$$\mathcal{L}(\Delta_{C_i}) - \mathcal{L}(\Delta_{C_{i-1}}) = \text{const.} \qquad \forall i \in \mathbb{N}. \tag{4.10}$$

This means that the length scale of each NLCE calculation rises equally, if the next larger cluster is also included in the calculations. The hope was to find a relation that leads to an critical exponent of -1. However, it turned out that for the given set of points, any adjustment only leads to a linear behaviour with $m = -1$ for a subset of points. The points outside showed a deviation from the linear behaviour. To gain further insight, it would be helpful to calculate more data points. This also could gives information, if the

linear behaviour in fig. 17 extends or if it converges to another trend. Especially for this model, it is possible to do this extension to larger clusters, since one can map the system to a Hamiltonian of size $2N \times 2N$, with N the number of sites. Therefore, the issue of an exponential increasing Hilbert space is avoided. This highlights once more, why the linear chain is a good testing model to gain further insight into the method.

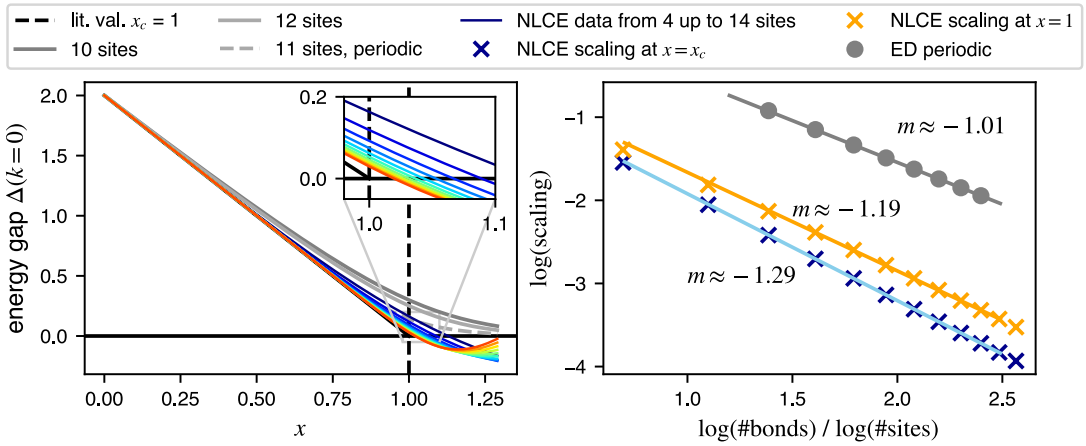

Figure 17: Left: Energy gap of the linear chain calculated with NLCE based on cluster sizes from 4 up to 14 spins. Additionally, the energy gap from finite clusters and of periodically coupled clusters are shown (grey). Right: Scaling behaviour of NLCE over the number of bonds. Hereby we tested the behaviour both at the point $x = 1$ and at x with $\Delta(x) = 0$ for each data set. For the latter, we took then the difference relative to $x = 1$. As a comparison, the scaling of periodically coupled clusters is shown with respect to the number of sites. For all points, we extracted the slope by a linear fit. The value of each gradient m is given in the plot.

4.1.2. CUT-Method: deepCUT

For illustrative purposes, the energy gap was also calculated via deepCUT up to second order. As explained in section 2.4.1, the first step is to determine a potential basis set of monoms A_i, which is then truncated in a later stage. The initial set of monomials is

$$\begin{aligned} A_0 &= \mathbb{1}, \\ A_1 &= b_i^\dagger b_i, \\ A_2 &= b_i^\dagger b_{i+1} + b_{i+1} b_i^\dagger, \\ A_3 &= b_i^\dagger b_{i+1}^\dagger + b_i b_{i+1}, \end{aligned}$$

with A_0/A_1 corresponding to order 0 and A_2/A_3 to the first-order contributions. To obtain the first-order terms, one has to calculate

$$[\eta[A_3], A_1] = [b_i^\dagger b_{i+1}^\dagger - b_i b_{i+1}, b_i^\dagger b_i] = -2A_3. \tag{4.11}$$

Since no new terms appear, all first-order terms are already given. The monoms of second-order are calculated following the same scheme

$$[\eta[A_2], A_3] = -2A_4 + 4A_5, \tag{4.12}$$
$$[\eta[A_4], A_1] = -2A_4, \tag{4.13}$$
$$[\eta[A_5], A_1] = -2A_5. \tag{4.14}$$

As the next step one has to discard all monoms which do not contribute to the targeted quantity. As described in section 2.4.1, one therefore calculates for every monom its minimal and maximal order. A monom is discarded if it fulfills following condition:

$$O_{\max}(A_i) < O_{\min}(A_i). \tag{4.15}$$

In table 1 all the monoms up to the second order are listed with their corresponding order. Consequently all terms except A_0, A_1 and A_3 are discarded. Since also the corresponding D_{ijk} components are discarded, the differential equations are reduced to:

$$\partial_l h_0(l) = 0 \to h_0 = 0, \tag{4.16}$$
$$\partial_l h_1 = 0 \to h_1 = 2, \tag{4.17}$$
$$\partial_l h_3 = 0 \to h_3 = x, \tag{4.18}$$

which leads to

$$H_{\text{eff}}(l \to \infty) = 2A_1 + xA_3. \tag{4.19}$$

After applying a Fourier-Transformation one obtains the analytic result of the energy gap. This is not surprising since one has truncated the basis properly.

Table 1: Basis terms

A_i	monom	$O_{\min}(A_i)$	$O_{\max}(A_i)$
A_0	$\mathbb{1}$	0	0
A_1	$b_i^\dagger b_i$	0	2
A_2	$b_i^\dagger b_{i+1}^\dagger + h.c.$	1	0
A_3	$b_i^\dagger b_{i+1} + h.c.$	1	2
A_4	$b_i^\dagger b_{i+2}^\dagger + h.c.$	2	0
A_5	$b_i^\dagger b_{i+1}^\dagger b_{i+1} b_{i+2}^\dagger + h.c.$	2	0

Table 2: Basis terms

A_i	monom
A_0	$\mathbb{1}$
A_1	$b_i^\dagger b_i$
A_2	$b_i^\dagger b_{i+1}^\dagger$
A_3	$b_i b_{i+1}$
A_4	$b_i^\dagger b_{i+1}$
A_5	$b_i b_{i+1}^\dagger$

4.1.3. CUT-Method: OS-CUT

As discussed in section 2.4.2, the OS-CUT method uses information obtained from finite clusters (namely the generator S) to evaluate the effective Hamiltonian directly in the thermodynamic limit. This is done for the linear chain based on information about the dimer and the trimer.

As the first step, we calculate the effective Hamiltonian based on the information from the dimer. As described in section 2.4.2, the generator $S = \log(T)$ takes the form:

$$S = \begin{pmatrix} 0 & 0 & 0 & \alpha(x) \\ 0 & 0 & 0 & 0 \\ 0 & 0 & 0 & 0 \\ -\alpha(x) & 0 & 0 & 0 \end{pmatrix} = \alpha \sum_i b_i^\dagger b_{i+1}^\dagger - b_i b_{i+1}, \tag{4.20}$$

with $\alpha = \frac{1}{2} \arctan x$. Similar to the deepCUT approach, the Hamiltonian is expanded in terms of monoms

$$H(\theta) = \sum_i h_i(\theta) A_i. \tag{4.21}$$

A complete basis set is obtained by calculating $[S, H(\theta)]$ and truncating the result so that no hopping process larger than the length scale included in S is considered. In general, the commutators have to be calculated until self-consistency is reached, i.e. no new terms arise that contribute to the flow equation. In the specific case, the commutator is self-consistent with the initial monoms

$$[S, H(\theta)] = -\alpha(h_3(\theta) + h_2(\theta)) + 2\alpha(h_3(\theta) + h_2(\theta))A_1 - 2\alpha h_1 A_2 - 2\alpha h_1 A_3, \tag{4.22}$$

which leads to the following differential equations:

$$\partial_\theta h_0 = \alpha(h_3 + h_2), \tag{4.23}$$
$$\partial_\theta h_1 = -2\alpha(h_3 + h_2), \tag{4.24}$$
$$\partial_\theta h_2 = 2\alpha h_1, \tag{4.25}$$
$$\partial_\theta h_3 = 2\alpha h_1, \tag{4.26}$$
$$h_4 = J = h_5, \tag{4.27}$$

with the initial conditions:

$$h_0(\theta = 0) = 0, \tag{4.28}$$
$$h_1(\theta = 0) = 2, \tag{4.29}$$
$$h_2(\theta = 0) = h_3(\theta = 0) = h_4(\theta = 0) = h_5(\theta = 0) = J. \tag{4.30}$$

In the next step, the commutator of $H(\theta)$ and S is integrated over the interval $[0, 1]$, leading to the effective Hamiltonian

$$H_{\text{eff}} = H_0 + \int_0^1 [S, H(\theta)] = 2b_i^\dagger b_i - x(b_i^\dagger b_{i+1} + h.c.), \tag{4.31}$$

and to the analytic solution of the energy gap. Hereby, the integration over the second commutation cancels out all higher terms. As we will also see for other models, this framework generally leads to better results. The reason of this empirical observation is not yet completely understood. As stated already in section 2.4.2, it is known, that the eigenstates of order n contains information about the energy in order $2n + 1$. From this perspective, this observation is not completely surprising. However, it is remarkable that the whole framework not only gives a very good approximation, it even gives us the exact result. Here, it should be noted that this is probably deeply related to the fact that the linear chain is analytically solvable and that the its energy gap is exact up to first order. Nevertheless, it demonstrates that the method selects the correct truncation at least for this specific case.
It is also important to mention that eq. (4.31) is independent of the value of α, i.e., only the structure of S is crucial for this system. To gain a better understanding, the same procedure was also applied to the generator with information up to 3 spins, which leads to an embedded S like:

$$S = \Sigma(S_2) + \Sigma(\tilde{S}_3), \tag{4.32}$$

with $\tilde{S}_3$ the reduced generator from 3 spins

$$\tilde{S}_3 = S_3 - S_2 \otimes \mathbb{1} - \mathbb{1} \otimes S_2. \tag{4.33}$$

The symbol Σ denotes, that the quantity is already embedded. For the reduced $\tilde{S}_{C3}$ for the three-site cluster, we obtain the following matrix representation:

$$S = \begin{bmatrix} 0 & 0 & 0 & -\beta & 0 & -\gamma & -\beta & 0 \\ 0 & 0 & 0 & 0 & 0 & 0 & 0 & -\beta \\ 0 & 0 & 0 & 0 & 0 & 0 & 0 & \gamma \\ \beta & 0 & 0 & 0 & 0 & 0 & 0 & 0 \\ 0 & 0 & 0 & 0 & 0 & 0 & 0 & -\beta \\ \gamma & 0 & 0 & 0 & 0 & 0 & 0 & 0 \\ \beta & 0 & 0 & 0 & 0 & 0 & 0 & 0 \\ 0 & \beta & -\gamma & 0 & \beta & 0 & 0 & 0 \end{bmatrix}, \tag{4.34}$$

with the real parameters γ and β, which can be determined numerically. Consequently, after embedding it into the thermodynamic limit, the complete S takes the following

form

$$S = \overbrace{\alpha \sum_i \left(b_i^\dagger b_{i+1}^\dagger - h.c.\right)}^{S_2} \tag{4.35}$$

$$+ \underbrace{\sum_i \left[\beta\left(b_i^\dagger b_{i+1}^\dagger - h.c.\right) - \gamma\left(b_i b_{i+1} - h.c.\right) + 2\gamma(b_i b_{i+1}^\dagger b_{i+1} b_{i+2} - h.c.)\right]}_{\tilde{S}_3}. \tag{4.36}$$

Similar to before, one has to obtain the basis set of A_i, to determine the differential equations as a next step. In appendix A.2, both the basis and the differential equations are given. As in the dimer case, the resulting Hamiltonian again leads to the analytic result of the energy gap. Interestingly, once again, only the structure of S is important, not the exact values of the parameters α, β and γ (which were chosen randomly in the interval $[-10, 10]$). Based on these observations, one can assume that this holds for all orders of S in this model. The exact reason why only the structure of the generator leads to the correct result for this specific model is yet unknown.

4.1.4. CUT method: OS-CUT numerical implementation

In the previous chapter, we used the idea of the OS-CUT method in combination with the generators S, calculated with PCAT, to set up a system of differential equations for determining the effective Hamiltonian. In this section, we apply the numerical version (see section 2.5). To do this, we use the generators S_2 and S_3, which are extracted from clusters with two and three sites:

$$S_2 = \log(T_2) \qquad S_3 = \log(T_3). \tag{4.37}$$

As before, the reduced generator is

$$\tilde{S_3} = S_3 - S_2 \otimes \mathbb{1} - \mathbb{1} \otimes S_2. \tag{4.38}$$

For N' we use a system of 11 spins as shown in fig. 18. This means that the Hamiltonian H is defined only on cluster sizes up to 7 sites, since S_3 corresponds to hopping processes involving two bonds. Therefore, for H on larger cluster sizes, boundary effects would significantly increase. In other words, one always has to chose N' appropriately large for the Hamiltonian H under study.

To calculate a cluster expansion of H_{diff}, we use system sizes of $N = 4, 5, 6$ and 7. Based on these results, we can calculate the energy gap (see fig. 19). The general observation is that one obtains an energy gap close to the analytic result without using information from large clusters (S is only considered up to cluster with 3 sites and, for the lower plots, 4 sites), similar to the previous section. Looking at the gap (left sides of fig. 19), one sees the effect of choosing N' to be too small in comparison to N: the gap shows a greater deviation than the calculations for smaller N, due to boundary effects. In the dispersion

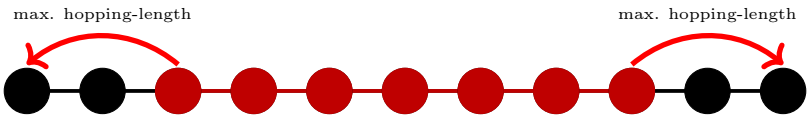

Figure 18: Illustrative sketch of the used system to calculate the gap with the modified OS-CUT method. The red part represents the system of size $N = 7$, which is embedded in the larger system with $N' = 11$. Since we only considered for the calculation only S up to 3 sites, it contains hopping processes up to two bonds.

at $x = 0.6$, one sees that the method leads to results near the analytic solutions for every k-value. However, an oscillating behaviour also appears, with minimal deviation to the analytic result around the gap ($k = 0$). Consequently, the integration process does not cancel the higher-order processes equally well for every mode, which is not surprising since only the gap is exact up to first order. Nonetheless, in comparison to ED and a standard numerical cluster expansion, these results are surprising and promising, since they are close to the perturbative solution while using information only from small clusters. As it can be seen in the plot, even NLCE calculations up to 11 spins result in a larger deviation. One downside of the method is that one has to use large N' if S is obtained from higher-order clusters. The resulting e^S is a computationally limiting factor without using further advanced techniques, since S is not limited on the model space (off-diagonal blocks are not zero).

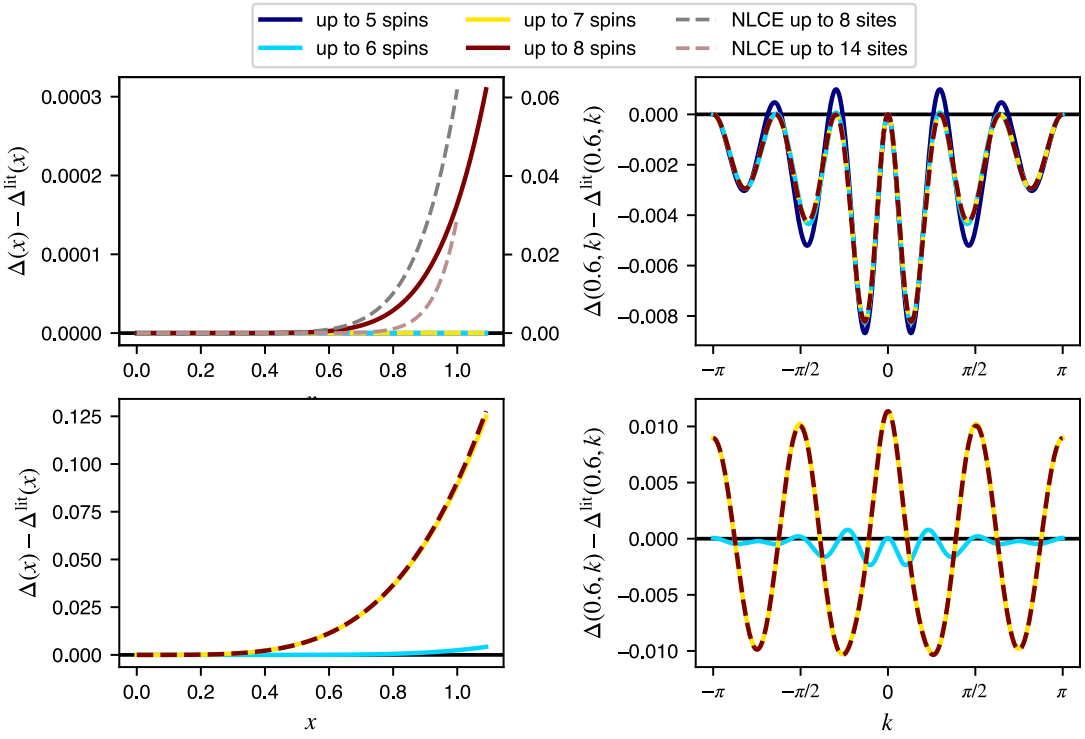

Figure 19: The plots show the numerical OS-CUT method for the linear chain. For the calculations, we set $N' = 11$. The top row shows the gap and the dispersion at $x = 0.6$ for an S based on the dimer and trimer. The lower row also included a cluster of 4 spins to calculate S.

4.2. Spin ladder

The first model discussed here, without a known analytic solution, is the spin ladder, as depicted in fig. 20. One feature of the ladder, compared to the one-dimensional chain, is the existence of a two-site unit cell highlighted in red, leading to two bands in the 1QP dispersion. Thus, the Hamiltonian can be rewritten as

$$H_{\mathrm{I}} = J \sum_i b^\dagger_{A,i} b_{A,i+1} + b^\dagger_{A,i} b^\dagger_{A,i+1} + b^\dagger_{B,i} b_{B,i+1} + b^\dagger_{B,i} b^\dagger_{B,i+1} + b^\dagger_{A,i} b_{B,i} + b^\dagger_{A,i} b^\dagger_{B,i} + \mathrm{h.c.},$$

$$H_{\mathrm{Field}} = h \sum_i \left(b^\dagger_{A,i} b_{A,i} + b^\dagger_{B,i} b_{B,i} \right),$$

with the hard-core boson operators $b_{A,i}/b_{B,i}$ which act on sites A/B of unit cell i.
As a local basis, we choose the standard eigenbasis of H_{Field}, denoted as:

$$\left| \begin{matrix} n_{B,1} & n_{B,2} & n_{B,3} & \cdots \\ n_{A,1} & n_{A,2} & n_{A,3} & \cdots \end{matrix} \right\rangle \qquad \text{with} \qquad n_{i,j} \in 0, 1 \tag{4.39}$$

with $n_{A,i}$ / $n_{B,i}$ denote if site A / B at unit cell i has an excitation.
In the following, the quantum phase transition coming from the high- ($h \gg J$) and low-field ($J \gg h$) limit is described.

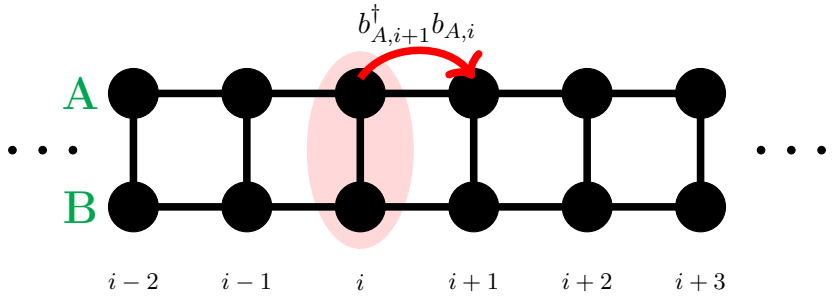

Figure 20: Sketch of the geometry of the spin ladder with a unit cell containing two sites (marked as red).

4.2.1. High-field limit

First, we calculate the energy gap in the high-field limit, so that the Hamiltonian can be rewritten as

$$H = \sum_{i, s \in A,B} b^\dagger_{s,i} b_{s,i} - x \left(\sum_{i, s \in A,B} b^\dagger_{s,i} b_{s,i+1} + b^\dagger_{s,i} b^\dagger_{s,i+1} + \mathrm{h.c.} + \sum_i b^\dagger_{A,i} b_{B,i} + b^\dagger_{A,i} b^\dagger_{B,i} + \mathrm{h.c.} \right),$$

with the perturbation $x > 0$ (ferromagnetic coupling). Generally, there are several ways to perform the cluster extension. For example, one can select an expansion in terms of finite chains, similar to the linear chain above. However, it should be noted that

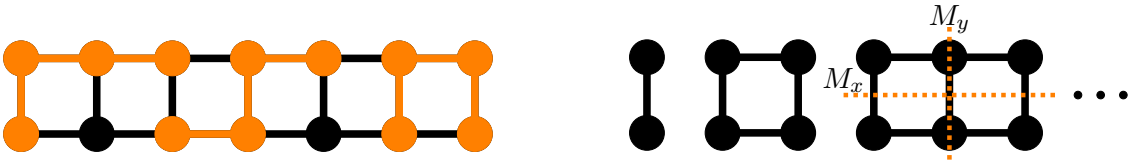

Figure 21: Left: Example embeddings of 4-site chains into a ladder. Right: First 3 subclusters for expansion in terms of unit-cells.

several different embeddings of one subcluster into the original lattice exist and have to be taken into account. In fig. 21, one sees three possible embeddings of a four-site subcluster into the lattice. With the increasing size of the subcluster, the number of possible embeddings also increases, and therefore, certain algorithms are often applied to calculate the different embeddings [54]. To overcome this, we chose an expansion in terms of unit cells, as shown in fig. 21. In addition, as with the chain, for NLCE calculations for the gap up to size of n dimers ($2n$ sites), only calculations on clusters with n and $n-1$ dimers are necessary (compare eq. (2.39)).
By performing a straightforward TBOT calculation, one obtains the following result for the gap up to order 8

$$\Delta(x) = -2 - 3x - 0.75x^2 - 0.75x^3 - 0.015625x^4 - 0.6875x^5 + 0.68164062x^6 \tag{4.40}$$
$$- 0.80615234x^7 + 1.42822266x^8, \tag{4.41}$$

which also directly leads to a good approximation of the literature value for the critical point $x_c = 0.54584$ ([55]), since the convergence radius of the series is sufficiently large (fig. 22). To achieve higher orders, one must increase the size of the respective system by one dimer.
In fig. 22 both the dispersion and the energy gap is shown for different NLCE calculations. As can bee clearly seen, NLCE converges well and gives better results than ED calculations with similar cluster sizes analogous to the linear chain. To study the convergence a bit further, fig. 23 shows the scaling of the energy gap at the literature value and of the obtained x_c value for each NLCE calculation. By fitting an exponential curve, the obtained critical value is close to the one known from the literature. However, as for the chain, one can not yet extract the critical exponent by a log-log plot over the spatial extension in x-direction (number of dimers minus one). The idea behind choosing this order was the assumption, that the contribution of the vertical extension vanishes for large systems. In comparison, ED calculations on periodic coupled systems lead to the expected value of -1 for the critical exponent. As for the chain, further research on larger systems is necessary, to gain a deeper insight. Since larger systems are easier to accomplish for the chain (mapping the system to Fermions to reduce the $2^N \times 2^N$ to a $2N \times 2N$ problem), the hope is that solutions found there, can be easily applied to other systems, like the ladder.

As a final step, the OS-CUT approach was applied to the ladder. For setting up the differential equations, we constructed the generator S based on the second cluster in the

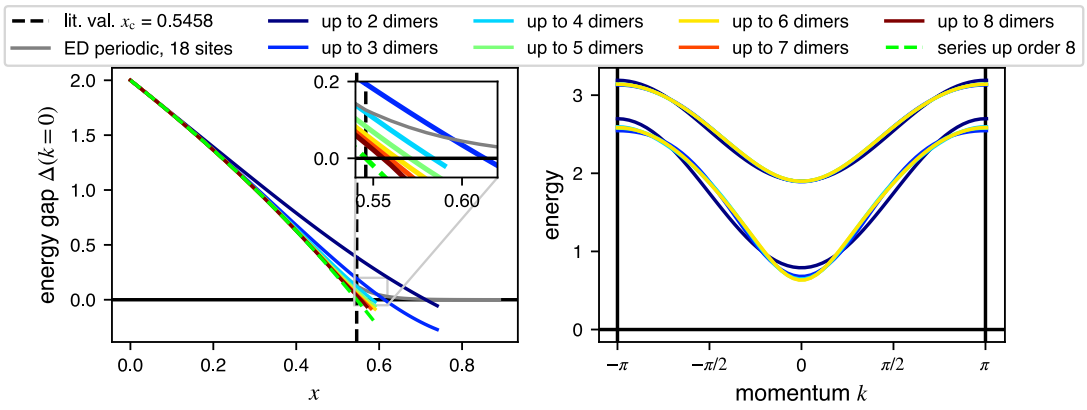

Figure 22: Left: ED, series up to order 8 and NLCE results for the energy gap. The literature value of $x_c = 0.5458$ is taken from [55], which is also well obtained by the series. Right: example of the lower lying band for different orders, with the gap at $k = 0$.

cluster-expansion in fig. 21. The details, like the exact form of this determined S as well as the differential equations can be found in the appendix. Here, we want to focus on the results, mainly the comparison to the NLCE calculations, given in fig. 24.

The left plot shows the results of the OS-CUT approach based on differential equations. For this approach the S from the cluster with 4 spins is embedded into the infinite system and the differential equations

$$\partial_\theta H = [S, H] \qquad \theta \in [0, 1]$$

are solved. The energy gap from the resulting effective Hamiltonian (green solid line) fits the NLCE data up to 2 dimers well. This is in alignment with the expectation, since $H(\theta) = e^{-S} H e^{S}$ is a solution of the flow equation. However, by calculating $\int_0^1 [S, H]$, one obtains the actual energy gap of this approach. The corresponding critical value shows an improvement compared to the NLCE calculations up to 4 spins. In fact, the resulting value is close to that obtained from NLCE calculations up to 4 and 5 dimers. This is expected because S contains higher orders from the energies, even though it is calculated from smaller clusters. This alone illustrates the potential of using S. However, until now, the idea is not implemented in a systematic framework that would allow efficient calculations of higher orders of S. In this context, it is worth mentioning that the obtained energy gap shows a remarkable deviation around $x = 0.3$ compared to the NLCE calculation. To understand this further, one would need to examine the convergence behaviour of the OS-CUT approach in more detail. Thus, the development of an efficient calculation scheme would be highly desirable.
The results from the numerical version are shown on the right side of fig. 24. Here, S is also determined from the cluster of 4 spins. Two points are worth mentioning here:

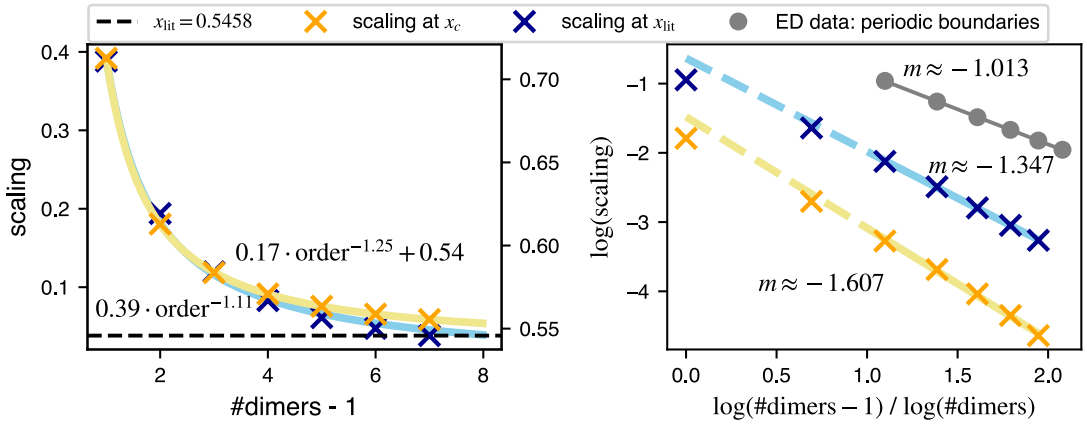

Figure 23: Scaling behaviour of the energy gap of TFIM on a spin ladder in the high-field limit. Left: Both the energy gap at the literature value (orange) and the critical point x_c for each NLCE calculation (blue) are shown over the number of dimers reduced by 1. For each set of points, an appropriate fit is done as denoted in the figure. Right: Both data sets of the left plot are presented into a log-log plot to extract the critical exponent by a linear fit. For the fit only the last 5 points are used to minimize possible effects of lower orders. The grey points show the scaling of ED calculations on a periodically coupled cluster at the literature value.

First, the resulting critical point is closer to the literature. Moreover, the deviation from the NLCE calculations are very small for small x and increases slightly for larger values of x. Both observations differ from those of the previous approach. However, one has to take into account, that the truncation in both schemes is different. In the approach based on the differential equations, the truncation is done related to the arising hopping processes. In the numerical approach, more orders are taken into account because the exact states are used (for the approach using differential equations, a truncation scheme was already used to set up H). As a second point, one clearly sees, that by increasing N', the resulting critical point is closer to the literature value. This is also associated with the truncation in this approach. As mentioned in section 2.5, N' has to be chosen large enough so that the targeted hopping process fits within the cluster. In another view, one can say, that the reembedding in the system of size N' should mimic the thermodynamic limit. But for computational purposes, we only chose N' large enough with respect to the targeted processes.
In general, both ways of using S show high potential for calculating single-particle properties. An interesting but not yet studied question is whether one can extract the critical exponents from this scheme. To test this, one has to find an efficient way to calculate higher orders, which is generally necessary to obtain more insights into these two schemes.

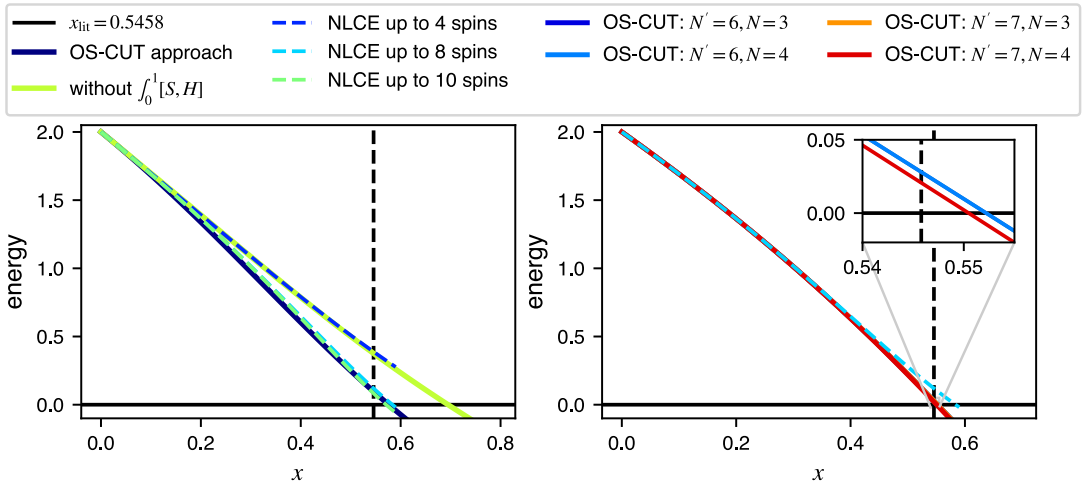

Figure 24: Energy gap determined based on the modified OS-CUT approach in comparison to NLCE results. Left: The gap is calculated by solving the differential equations and S is determined from clusters up to 2 dimers. The lime-green line, labeled as $\int_0^1 [S, H]$, represents the gap extracted directly from the differential equations ($\partial H = [S, H]$). Right: Here, the idea of M. Hörmann is applied to use the framework of OS-CUT for numerical calculations. The values N and N' correspond to the notation in section 2.5. As it can be seen, the resulting critical value is close to the literature value.

4.2.2. Low-field phase

In the previous section, we calculated the energy gap starting in the high-field phase. The advantage in this limit is the well-defined particle picture of the treated model. In this section, the external field is treated as the perturbation (low-field limit). In comparison to the high-field limit, the particle picture has to be adjusted, as the fundamental excitations now consist of bonds with alternating spins in the antiferromagnetic case or equally aligned spins in the ferromagnetic case. Therefore, it is possible to rewrite the entire Hamiltonian into a bond picture, with the associated mapping

$$\tilde{\sigma}^z_\beta = \tilde{\sigma}^z_{<i,j>} = \sigma^z_i \sigma^z_j, \tag{4.42}$$

$$\tilde{A}_s = \prod_{\beta \in s(i)} \tilde{\sigma}^x_\beta, \tag{4.43}$$

which is based on [56]. The index β enumerates the bonds of neighbouring sites. The new operator $\tilde{A}_s$ arises from the fact that a spin-flip at any site i changes the value of the adjoining bonds, denoted as the set $s(i)$ (see fig. 29). The resulting Hamiltonian can then be written as:

$$H = x \sum_i \sigma^x_i + \sum_{<i,j>} \sigma^z_i \sigma^z_j \xrightarrow{\text{mapping}} \sum_\beta \tilde{\sigma}^z_\beta + x \sum_s \tilde{A}_s. \tag{4.44}$$

However, for the following discussion, we remain in the spin picture, while keeping in mind that the energy is determined by the bonds. For the calculation on finite clusters, we also use a fixed environment, as seen in fig. 29. This ensures that a spin-flip at mutual ends of the clusters excites 3 bonds instead of 2, as would be without the spin environment. Additionally, by choosing these environments, the system is split into two different symmetry blocks, since mapping one system onto the other would require an infinite number of spin flips. Therefore, we can use this to choose two different low-lying excitations.

Before presenting the results of the calculations, we will first give an overview of some low-energy states. Fig. 25 shows a schematic sketch of the unperturbed energy ($x = 0$) of the first 5 excitations. Due to the lattice geometry, it is impossible for the spins to align in such a way that only one excited bond exists. Consequently, the domain wall (DW) excitation (see fig. 26) describes the lowest excitation, since only two bonds are excited. Since two domains walls can be separated by an arbitrary number of sites without influencing the energy, there exists a continuum of these excitations, with 4 excited bonds each. Here, one

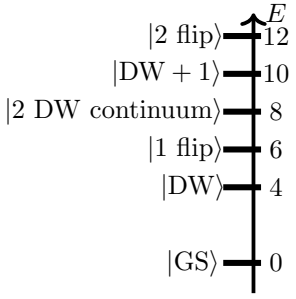

Figure 25: Schematic representation of low lying unperturbed energy levels.

also has to consider that the same energy can also be achieved by two horizontally neighboring spins (see fig. 28).
Above the domain-wall excitation, one finds a configuration with only one flipped spin (see fig. 29). The same energy can be obtained by an appropriate domain wall. Since both states are protected by symmetry (the latter is not present in a periodically coupled system), we will focus only on the one spin-flip excitation here. Examples of higher-lying states include domains walls shaped like those in fig. 28, or two spin flips which are sufficiently far apart. Of course, there are more higher lying excitations, but here we want to focus on the two lowest excitations, namely the domain wall and the one-spin-flip exciation.

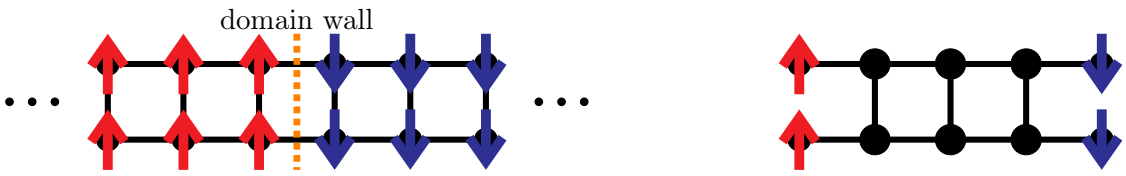

Figure 26: Left: Lowest excitation in antiferromagnetic case are domain walls. Right: Example of a cluster with suited environment to calculate domain walls energy gap with NLCE in the spin-picture.

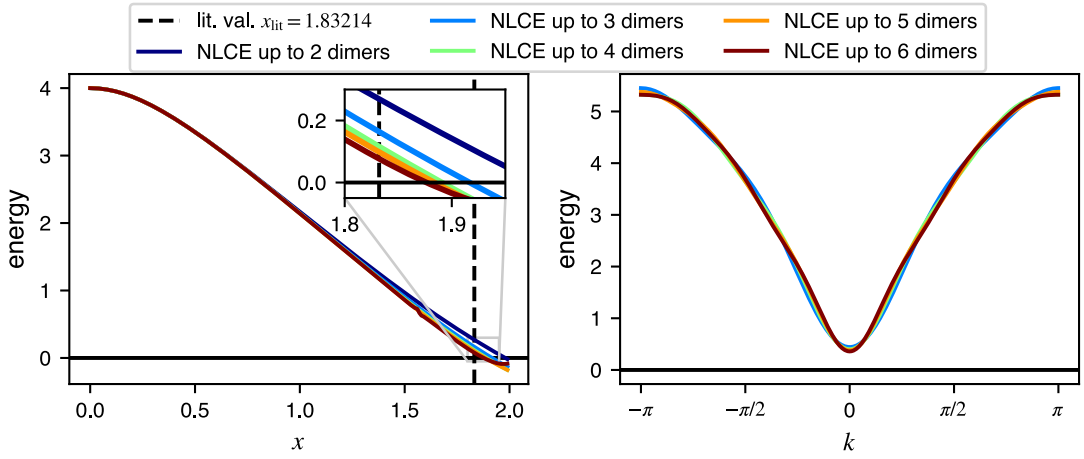

Figure 27: Left: Energy gap for the domain wall. The discontinuity of the brown curve originates from numerical errors. The literature value for the critical point $x_c = 1.83214$ is taken from [55]. Right: Dispersion based on NLCE calculations for $x = 1.7$. The dispersion consists only out of one band, since the two excited bonds of the domain-wall always appear vertical as a pair.

The first excitation under investigation is the domain-wall excitation. Since this excitation is the lowest in the low-field limit, it is suggested that this phase is the counterpart

to the 1-flip excitation in the high-field limit, i.e., we expect that the energy gap closes at the same critical value. This is in agreement with the NLCE data shown in fig. 27. For the calculations of the hopping terms, a cluster with a flipped environment on both sides is used, as shown in fig. 26. One has to note that the ground state is calculated on a cluster with an equally aligned background (fig. 29), which shows that both states are protected by symmetry. In other words, an infinite number of spin flips would be required to map the states onto each other:

$$\langle \mathrm{GS}| \prod_{i=0}^{N} \sigma_i^x |\mathrm{DW}\rangle = 0 \qquad \text{if} \quad N < \infty, \tag{4.45}$$

with i denotes the lattice sites. From a different point of view, this can be also seen by considering the state of two vertical domain walls and the state of one domain wall. Both states are separated by the symmetry $P = \prod_i \sigma^z_{A,i}\sigma^z_{B,i+1}$ (with $P^2 = \mathbb{1}$). Since the ground state and the state of two domain-walls are connected by A, it follows that the ground state and the domain wall belongs to separated spaces. By similar arguments, the same holds for the domain-wall and the state $|1\text{ flip}\rangle$, which becomes important when studying the one-spin-flip excitation.

The second mode under study is the one-spin-flip excitation aka the excitation of three bonds (see fig. 29). Because ground-state (all spins down) and one-spin flip excitation are directly coupled by the perturbation V (not protected by symmetry), one has to apply the subtraction scheme form PCAT (see section 2.3) to reach cluster additivity. To emphasize the importance of this, one can compare it with the TBOT results for the system of two distinct clusters, as shown in fig. 30. The effective Hamiltonian obtained by TBOT in order 6 takes the form

$$H^{(6)}_{\mathrm{TBOT}} = \begin{pmatrix} -0.28627 & -0.22531 & -0.22531 & -0.16152 & -0.00116 & -0.00116 \\ -0.22531 & -0.28627 & -0.16152 & -0.22531 & -0.00116 & -0.00116 \\ -0.22531 & -0.16152 & -0.28627 & -0.22531 & -0.00116 & -0.00116 \\ -0.16152 & -0.22531 & -0.22531 & -0.28627 & -0.00116 & -0.00116 \\ -0.00116 & -0.00116 & -0.00116 & -0.00116 & -0.15566 & -0.15638 \\ -0.00116 & -0.00116 & -0.00116 & -0.00116 & -0.15638 & -0.15566 \end{pmatrix}.$$

The off-diagonal elements represents the forbidden hopping processes between the disjoint clusters. In comparison, PCAT leads to a cluster-additive form:

$$H^{(6)}_{\mathrm{PCAT}} = \begin{pmatrix} -0.28724 & -0.22531 & -0.22531 & -0.16152 & 0 & 0 \\ -0.22531 & -0.28724 & -0.16152 & -0.22531 & 0 & 0 \\ -0.22531 & -0.16152 & -0.28724 & -0.22531 & 0 & 0 \\ -0.16152 & -0.22531 & -0.22531 & -0.28724 & 0 & 0 \\ 0 & 0 & 0 & 0 & -0.15664 & -0.15638 \\ 0 & 0 & 0 & 0 & -0.15638 & -0.15664 \end{pmatrix}$$

This illustrates once more the importance of PCAT, which enables us to calculate the energy gap in an efficient way. The corresponding series expansion up to order 18 for

both bands at the band-gap momentum $k = 0$ is:

$$\begin{aligned}\omega_1(x, k=0) =& 6 - x^2 + 0.34722222x^4 - 0.20174897x^6 + 0.1446651x^8 \\ & - 0.11126578x^{10} + 0.08674759x^{12} - 0.06613306x^{14} \\ & + 0.04687068x^{16} - 0.02750241x^{18} \\ \omega_2(x, k=0) =& 6 - 1.66666667x^2 + 0.64351852x^4 - 1.45843621x^6 + 2.65635549x^8 \\ & - 5.94868019x^{10} + 13.66877106x^{12} - 32.85237879x^{14} \\ & + 81.18677197x^{16} - 205.43637075x^{18}\end{aligned}$$

In fig. 31, both the NLCE data and the series are shown in comparison to ED results. As can be seen, the NLCE calculation breaks down around $x \approx 1$, which approximately corresponds to the convergence radius of the series. Since there are several higher-lying states, the exact physical reason for this divergence cannot be determined without further investigation. However, it can be assumed that the one spin-flip state decays into the domain-wall continuum. Evidence for this is that the lower band of the domain-wall continuum intersects with the one-flip dispersion. As mentioned, further investigations, for example via ED, are necessary. Overall, one observes that the NLCE data describes the perturbative limit well, but fails to provide information beyond that. A similar case is seen in section 5.1.1, where the decay of k-modes also influence the perturbative results for other k-modes.

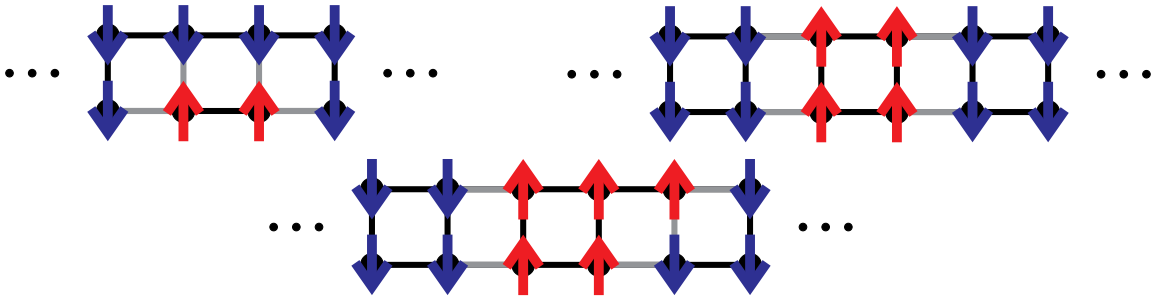

Figure 28: Top row: Schematic representation of states with four excited bounds. The state of the right side are two domain walls. Lower row: State with 5 excited bonds.

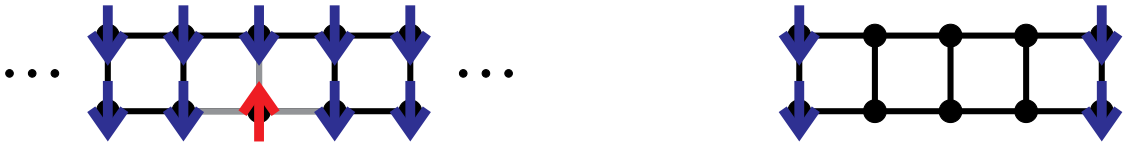

Figure 29: Left: State with one spin-flip. The corresponding excited bonds are marked in grey. Right: Cluster with an fixed environment. Such a cluster is used, to calculate the hopping terms of the one spin-flip.

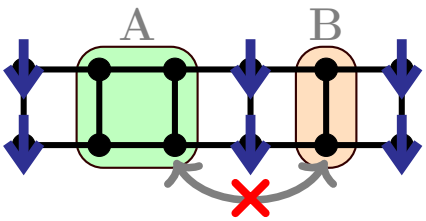

$$H_{\text{eff,1QP}} = P_1 T^\dagger H T P_1 = \begin{pmatrix} H_{\text{eff,A}} & \\ & H_{\text{eff,B}} \end{pmatrix}$$

Figure 30: Left: Two disjoint clusters A and B. Right: Schematic representation of the corresponding effective Hamiltonian. Since the clusters A and B are disjoint, no hopping processes between them are allowed.

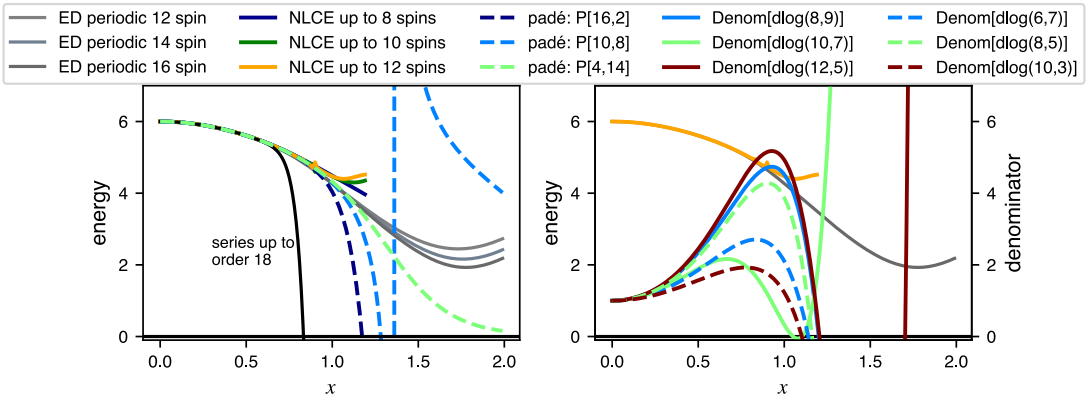

Figure 31: NLCE calculation for the one-spin-flip state. Left: The gap is compared to ED calculations and the series. Within the perturbative regime, the NLCE describes the system well. Beyond that, divergence occurs. Right: The denominator of the dlog-Padé extrapolation is plotted to investigate the singularities. As it can be seen, by considering higher orders of the series, the singularity moves slightly to the right.

4.3. Saw-tooth chain

The saw-tooth chain is particularly interesting in the antiferromagnetic case, as the effect of frustration arises due to its geometry. In general, frustration is an effect, when it is not possible to minimize all local energy conditions simultaneously [57]. In this particular case, this can be directly observed for the $h = 0$ limit: due to the antiferromagnetic coupling, neighbouring spins tend to align antiparallel. However, because of the triangular geometry of the strip, not all bonds can be in an antiferromagneic state. This is illustrated for an easy case in fig. 33, where no matter which direction the lower spin chooses, there will always be one bond with parallel-aligned spins. As a result, the ground state in the $h = 0$ limit is infinitely degenerated (one possible ground state is shown in fig. 33). This geometric frustration is also well-studied in other lattices, such as the triangular and kagome lattices (see e.g., [6]). In contrast to the saw-tooth chain, the

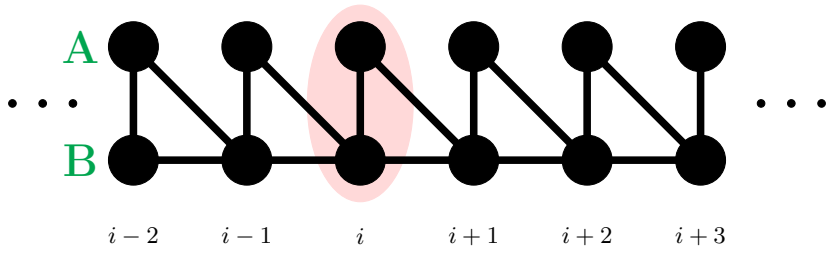

Figure 32: Saw tooth chain with red-marked unit cell.

triangular 2d lattice has a non-trivial quantum ordered-phases arising from the classical disordered case, which is known as order-by-disorder. In the saw-tooth chain (similar to the kagome lattice), one observes instead the effect of *disorder by disorder* (see [6] and [26]). This implies that in the saw-tooth lattice, a finite energy gap is always present.

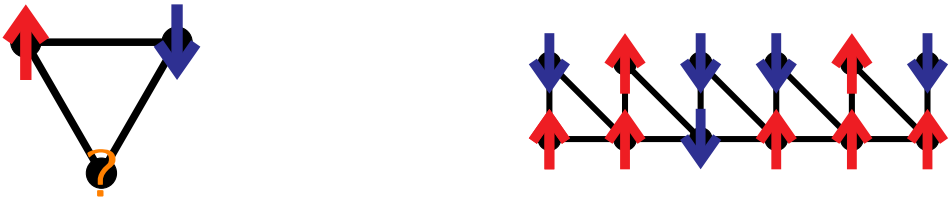

Figure 33: Left: Schematic illustration of geometric frustration. Right: Possible ground state in the $h = 0$ limit.

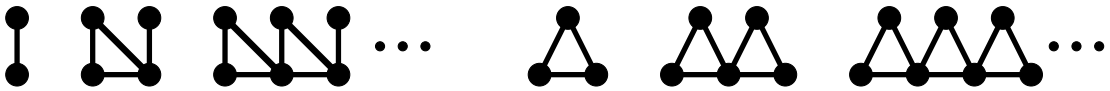

Figure 34: Left: Cluster expansion using dimers as fundamental building blocks. Right: Triangular cluster expansion.

For the NLCE calculation, we used two different cluster expansions, as shown in fig. 34. The left one is similar to the expansions used for the previous lattices. In comparison, the right side uses triangles as building blocks. By comparing the NLCE results for the energy gap (see fig. 35), it turns out that the unit-cell approach breaks down early due to avoided-level crossings. This issue can be partly repaired by using the $S = \log T$ from smaller clusters, to determine the diabatic eigenvectors (compare section 3.3), as seen in the inset of the plot: The adiabatic level begins to diverge, but the diabatic line shows a discontinuity, representing that the eigenstate changed towards the diabatic one. By considering only the left and the right part of the purple line, it seems, without further proof, that the right part represents a useful continuation. This illustrates clearly, how important it is, to use the correct states for constructing the transformation. As mentioned in section 3.3, such discontinuities as seen in our calculations are in general

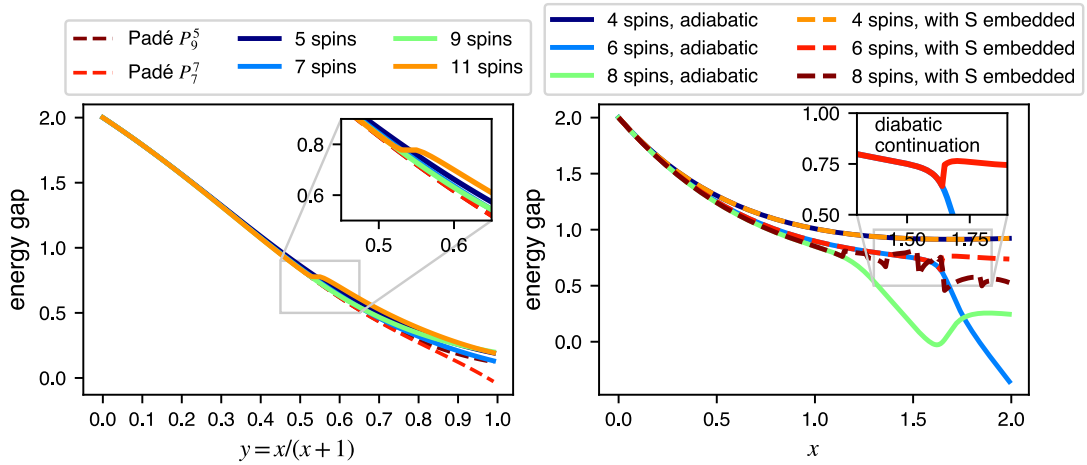

Figure 35: Left: NLCE data for triangular expansion. Right: NLCE data for unit-cell expansion. The inset boxes shows the sign of avoided crossing.

unsuitable for performing a cluster expansion. Therefore, one would need rather a superposition of eigenstates, as done in the gCUT approach. However, our data shows, that using S can be one building block for a more general framework.
By using the same S for larger clusters, one sees for this model that the transformation also breaks down in the non-perturbative regime. To overcome this, one probably would have to use an S based on a larger cluster. This underlines once more that this approach is itself not a working solution for the general problem of avoided level crossing.
In comparison, using the triangular expansion, the NLCE calculations lead to significantly better results. Note that, for displaying the data in fig. 35, an Euler transformation

$$x = \frac{y}{1-y} \tag{4.46}$$

is used to map x into the bounded interval $[0, 1]$. The first notable sign of an avoided crossing occurs in calculations which includes clusters with 11 spins (equivalent to the cluster consisting of 5 triangles). However, the NLCE data for smaller cluster sizes show similar behaviour as the Padé extrapolation (red-dotted line in the plot).

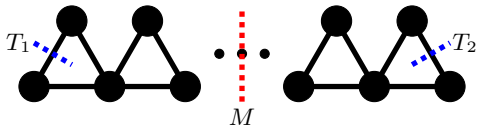

Figure 36: Illustration of three geometrical symmetries for every finite cluster in the triangular expansion.

In general, there are two possible reasons for this finding: First, the chosen clusters

behave more like the infinite lattice because they have similar symmetries, which effectively separate the corresponding states for small clusters. To illustrate this, we select three geometrical symmetries that every finite cluster has in common (see fig. 36). The corresponding symmetry operators have the following properties:

$$[T_1, T_2] = 0 = [M, T_1 T_2] \quad T_1^2 = T_2^2 = M^2 = \mathbb{1} \quad T_2 M = M T_1 \qquad T_1 M = M T_2 \tag{4.47}$$

The corresponding symmetry group is the dihedral group of order 8. One of its properties is that it has 5 distinct conjugacy classes, which means, in principle, that there is a representation of the group, that divides the Hamiltonian into 5 blocks. Since such a representation is not trivial to find (the group is not Abelian), we chose for our studies the Abelian subgroup generated by T_1 and T_2, which is also known as the *Klein four-group*. Consequently, by going into a common eigenbasis, the Hamiltonian can be written in a block structure, consisting of 4 blocks, which are denoted by $(-1, 1)$,$(-1, 1)$, $(1, -1)$ and $(1, 1)$, respectively. In fig. 37 the spectra of a subcluster of 5 and 7 spins is shown. The different colors correspond to the different blocks. Due to the symmetry, the highest level of the 1QP block has a higher distance to the lower bands of the 3QP states within the same symmetry block. This can be an explanation, why the resulting gap shows convergence for a large x interval. The general idea, that different cluster expansions can lead to better results than others is well known [58]. A second reason, which is not completely independent to the geometrical feature of the triangular clusters, is that the avoided crossings are very weak compared with the step size Δx used for the adiabatic tracking of the corresponding eigenvectors. For example, the unexpected behaviour of the orange curve in fig. 35 can be avoided by increasing the step size sufficiently, resulting in a gap closer to the Padé extrapolation. This means, that due to the larger step size, we automatically choose the diabatic transition.

A a final comment regarding the better convergence of the triangular expansion is the behaviour of the two 1QP energy band in the k-space (fig. 38). As the value of x increases, the lower band shows a strong convergence of the NLCE calculation, whereas the upper band deviates significantly. This may indicate particle decay in the higher band, which was supported by calculations based on the free particle approximation.

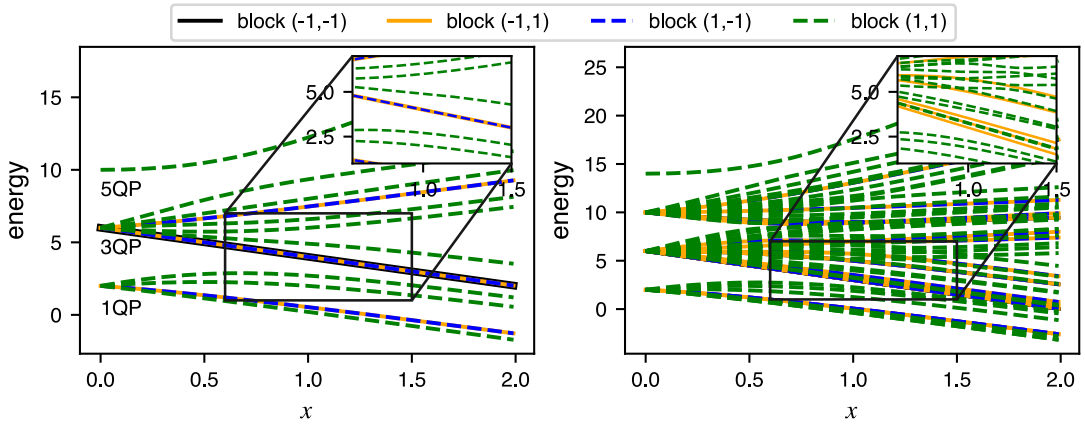

Figure 37: The spectra of finite clusters (left: 5 spins, right: 7 spins) in the triangular expansion. The colors mark the different symmetry blocks.

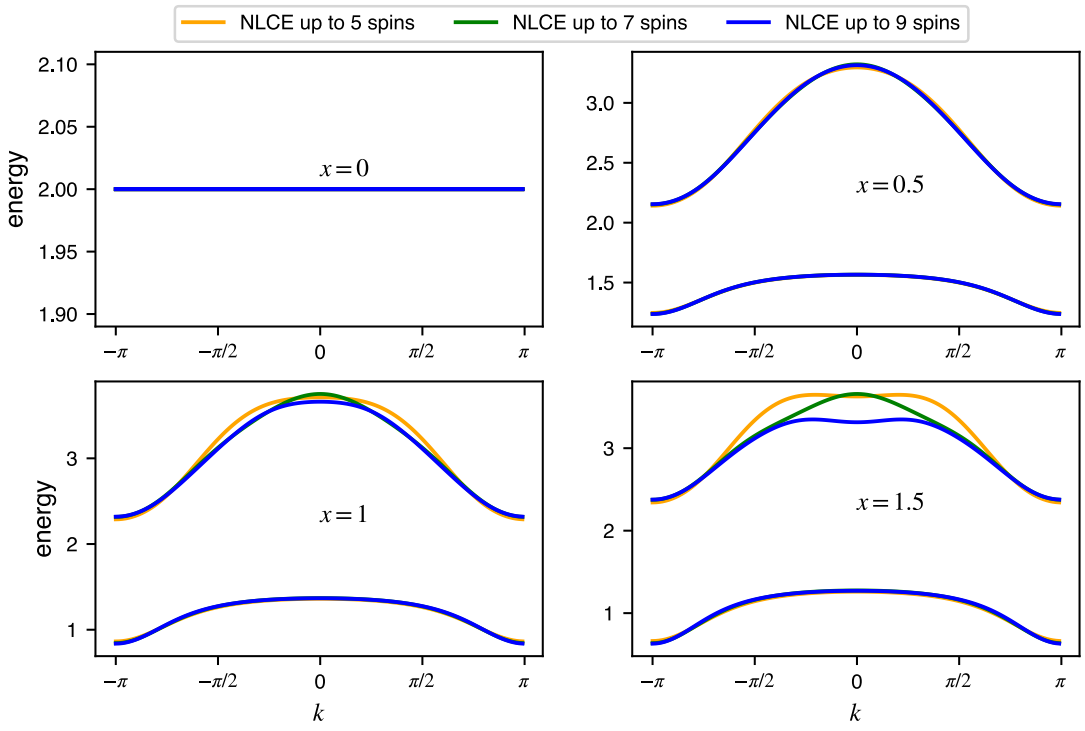

Figure 38: Energy dispersion for different values of x. It can be observed, that the lower band stays longer stable than the upper band.

4.4. ANNNI Model

In this section, the *axial next nearest neighbour Ising* model (short: ANNNI) is considered as a further example of a frustrated strip (see fig. 39) which nevertheless behaves quite differently from the saw-tooth chain. Therefore, some general features of the model are first introduced by primarily following [59] before discussing the calculations of the one-particle gap.

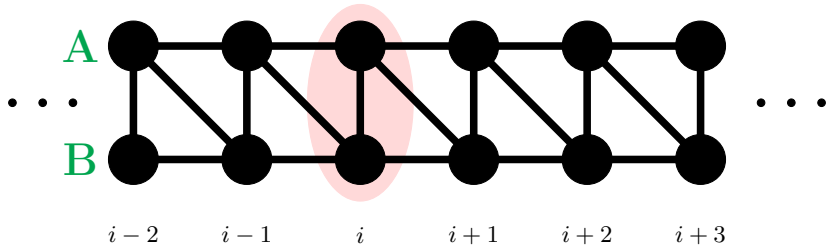

Figure 39: Lattice structure with next nearest neighbour couplings (ANNNI model). As for the other considered models, the strip has a two sited unit cell.

4.4.1. Frustration and Phase-diagram

As can be seen from the lattice geometry, the strip consists of triangles, which leads to frustration, as in the saw-tooth lattice. However, instead of having infinitely many ground-state configurations in the zero-field limit, the ladder has only 4 ground states, due to the additional bond which connects the free triangle site of the saw-tooth lattice. In fig. 40, the two ground-state configurations are shown, which are degenerate due to the $\mathbb{Z}_2$ symmetry. The finite number of ground-state configurations can also be seen numerically by the fact that the ground-state configurations do not scale with the lattice size N, as it is not an extensive quantity.

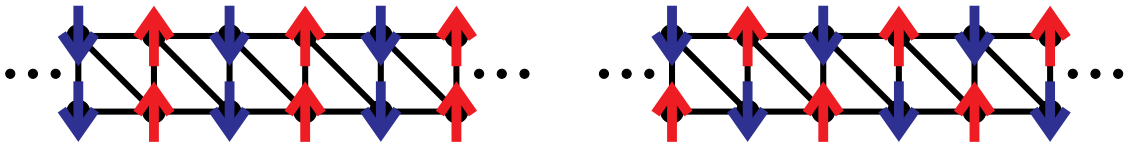

Figure 40: Schematic sketch of the ground states in the zero-field case ($B = 0$) of the ANNNI model. By taking the $\mathbb{Z}_2$ symmetry into account, the ground state is four-fold degenerate.

For introducing the phase diagram of the system, we write the general Hamiltonian as follows:

$$H = -J_1 \sum_{i}^{N-1} \sigma_i^x \sigma_{i+1}^x - J_2 \sum_{i=1}^{N-2} \sigma_i^x \sigma_{i+2}^x - B \sum_{i=1}^{N} \sigma_i^z. \tag{4.48}$$

Since the Hamiltonian is invariant under the transformation

$$J_1 \to -J_1 \qquad \sigma_i^x \to (-1)^i \sigma_i^x, \tag{4.49}$$

the sign of J_1 can be chosen arbitrarily, as the sign of B [60]. As is common in the literature (see e.g. [57],[60],[59]), we use the parameters $\kappa = -J_2/J_1$ and $h = B/J_1$. Before continuing the description of the phase diagram, we want to mention that the system can also be mapped ($\sigma_i^x \to \sigma_{i-1}^x \sigma_i^x$ and $\sigma_i^z \sigma_{i+1}^z \to \sigma_i^z$) to a dual Hamiltonian (XY model) with an in-plane field [61]. The advantage of the dual Hamiltonian is the avoidance of next-nearest-neighbour hopping elements. In the literature, perturbative calculations of the dual Hamiltonian regarding the energy gaps are given to provide more insight about the phase transitions.
The phase diagram is given in fig. 41. As can be seen, there are, in principle, 4 different phases: a ferromagnetic, a paramagnetic, a floating phase and an antiphase. All phases were studied already in numerous publications using various methods (e.g. DMRG and ED[60] [57], Tensor networks [59]), in addition to some analytical studies [61]. Moreover, the model phase diagram was also studied by investigating the 2D classical ANNNI model, since there is a general connection between quantum models in d dimensions to classical models in $d+1$ dimensions. Instead of an external field, the 2D classical model would be temperature dependent. However, it must be mentioned that this mapping is only exact for some limiting cases. [52]
For the case of vanishing h, there exists a multicritical point at $\kappa = 0.5$, which separates the ferromagnetic phase from the antiphase. In the ferromagnetic case ($J > 0$), the spins are aligned in x-direction. By increasing the magnetic field, the system undergoes a second-order phase transition towards the paramagnetic (disordered) phase, where the spins are aligned in the z-direction. The critical line separating these two limits can be approximated ([59]) as

$$h \approx \frac{1-\kappa}{\kappa}\left(1 - \sqrt{\frac{1-3\kappa+4\kappa^2}{1-\kappa}}\right), \tag{4.50}$$

by using a self-consistent Hartree-Fock method in the interacting fermion picture. The dotted line in the paramagnetic phase denotes the Peschel-Emery line, which has the following form:

$$h = \frac{1}{4-\kappa} - \kappa. \tag{4.51}$$

The special property of this line is, that the system can be solved there analytically.
The floating phase, unlike all the other phases, is gapless and can be described in principle by a Luttinger liquid. It is separated from the paramagnetic phase by a Berezinskii-Kosterlitz-Thoughless (BKT) transition, named after its discoverers. Kosterlitz and Thoughless were honord for their work of such topological phase transitions with the nobel prize in 2016. The critical line in the phase diagram can be also described approximately

$$h_{\mathrm{BKT}} \approx 1.05\sqrt{\left(\kappa - \frac{1}{2}\right)(\kappa - 0.1)}. \tag{4.52}$$

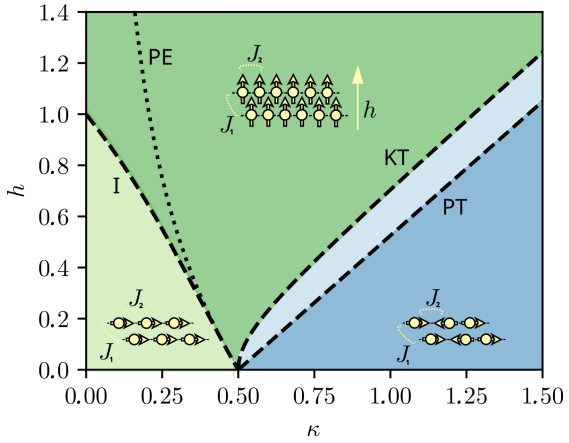

Figure 41: Phase diagram of the 1D ANNNI model, taken from [59].

This phase transition becomes important in the next section, as we attempt to capture the transition with our methods. The last phase, the antiphase is separated from the floating phase by a comensurate-incommensurate transition (Pokravskiy-Talapov universlaity class). The critical line can be approximated to

$$h_{\mathrm{PT}} = 1.05\left(\kappa - \frac{1}{2}\right). \tag{4.53}$$

In the antiphase, the antiferromagnetic ($J < 0$) next-nearest-neighbor interactions dominate, which leads to the ground state depicted in fig. 41.
In our study, only the paramagnetic phase and its Kosterlitz-Thoughless transition are investigated, as we examine the vertical line at $\kappa = 1$, starting from the high-field limit. So, we can rewrite the Hamiltonian in our usual form

$$H = \sum_j 1 - \sigma_i^z + x\left(\sum_j \sigma_j^x \sigma_{j+1}^x + \sigma_j^x \sigma_{j+2}^x\right) \tag{4.54}$$

$$= H_{\mathrm{ladder}} + x \sum_i b_{i,A}^\dagger b_{i+1,B} + b_{i,A} b_{i+1,B} + \mathrm{h.c.}, \tag{4.55}$$

with H_{ladder} the Hamiltonian of the ladder in the high-field limit and antiferromagnetic coupling.

4.4.2. Energy gap

Before studying the energy gap in detail, we first determine the corresponding k value. The dispersion relation (see fig. 42) reveals that, unlike other models, the minimum is not at $k = 0$ or $k = \pi$. Based on first-order perturbation theory, which was presented in the master thesis by Leon Schiller ([51]), the dispersion relation is given by:

$$w_k = 1 + x(2\cos k \pm \sqrt{(1 + \cos(k))^2 + \sin^2 k}, \tag{4.56}$$

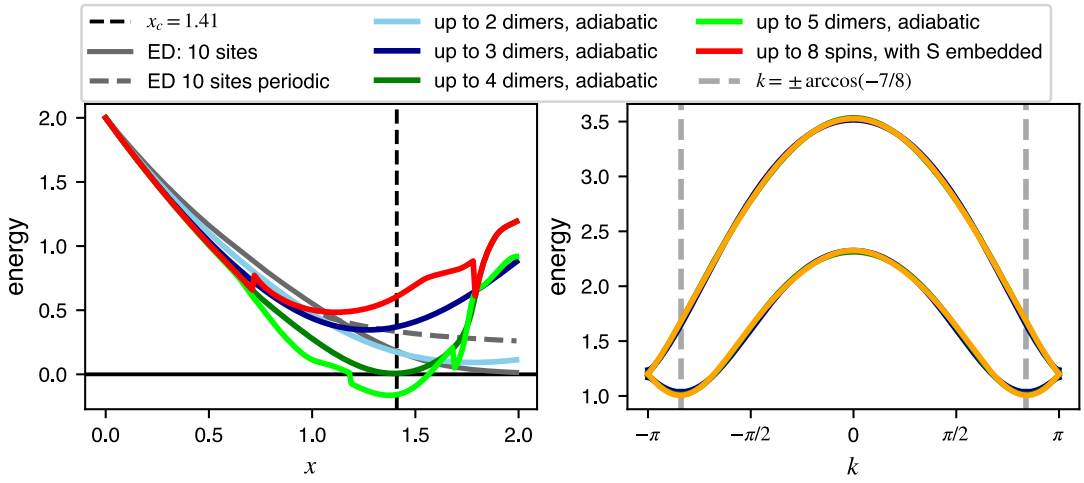

Figure 42: Left: The energy gap determined by NLCE and ED calculations. Right: Dispersion for $x = 0.5$ from NLCE calculations

which leads to a minimum at

$$k = \arccos\left(-\frac{7}{8}\right). \tag{4.57}$$

The consequence of k being an irrational product of π is that the k value does not fit within any finite system.
Another important difference compared to all previous models is the occurrence of a Berezinskii–Kosterlitz–Thouless (BKT) transition, instead of a second-order phase transition. A characteristic property of this transition is that the correlations length does not scale algebraically, instead it scales like ([62])

$$\xi = \xi_0 \exp\{a g^{-\nu}\}, \tag{4.58}$$

with g denoting the distance to the critical point, and ξ_0 and a non-universal constants. The critical exponent is denoted here with ν. In comparison, for the other models, the correlation lengths scales algebraically ([63]):

$$\xi \propto g^{-\nu}. \tag{4.59}$$

As before, NLCE was used to calculate the critical point. In fig. 42, the associated energy gaps as a function of the perturbation x are shown. Clearly, for clusters with the size of 4 dimers, problems arise regarding avoided level crossings. This can also be seen in fig. 43, where the series on a specific cluster is calculated up to high orders to determine the convergence radius of the subcluster. Unfortunately, for smaller clusters, the energy gap does not close at all. As an attempt to overcome the avoided level crossings, the S from smaller clusters was used to determine the eigenvectors for the transformation, as it was done in the toy example in section 3.3. As it can be seen, this does not lead

to an improvement of the energy gap. Thus, without any further improvements of the transformation, no information can be obtained about the critical point x_{crit} or the scaling. Of course, one also has to keep in mind that the phase transition is also difficult to describe with ED calculations, due to the exponential behaviour of the correlation length and the k value of $\arccos(-7/8)$.
In addition to the NLCE results, the series expansion of the two 1QP bands at $k = \arccos(-7/8)$ was determined by using TBOT:

$$\omega(k)_1 = 2 - 1.25x + 1.609375x^2 - 0.93164063x^3 + 0.80145264x^4 \tag{4.60}$$
$$- 1.5628891x^5 + 2.34576559x^6 - 4.26353818x^7 + 8.19380999x^8, \tag{4.61}$$
$$\omega(k)_2 = 2 - 2.25x + 0.734375x^2 - 0.86132812x^3 + 1.4274292x^4 \tag{4.62}$$
$$- 2.27806854x^5 + 3.9291358x^6 - 6.73724037x^7. \tag{4.63}$$

Like for the previous models, both the series as well as the NLCE calculations matches well in the perturbative regime.

Since the previous NLCE calculations do not lead to any physical insight, we also applied the modified OS-CUT scheme to the system. Therefore, we calculated the generator S based on finite clusters of up to 4 spins. To embed both H and S, we used systems sizes of $N' = 12$, $N' = 14$ and $N' = 16$ (see section 2.5). On the left side of fig. 44, the resulting gap is compared with the NLCE and series expansion results. The first remarkable observation is that this scheme leads to a closing gap. However, this critical point deviates significantly from the literature value (see black-dashed line in the plot). For values around $x = 0.5$ (perturbative regime), all methods convergence to each other. However, in the non-perturbative regime, the gap deviates from the Padè of the series up to order 7. However, if one only consider the series up to order 4, both the Padè as the modified CUT method leads to the same critical point. This shows again that S contains information up to order 4, even beyond the perturbative limit. To gain more insight, higher orders of S would be necessary, along with the calculation of using differential equations.
On the right side of fig. 44, the ED data on periodically coupled systems are also shown. The significant deviations in the ED calculations for 8 and 12 spins lie in the incommensurate k value of the gap, as only certain k values are present on the periodic finite lattices.

.

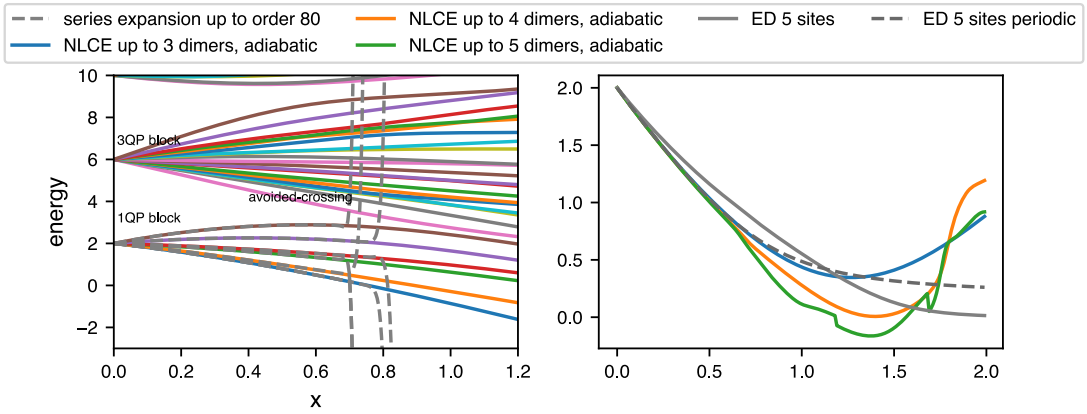

Figure 43: Left: Spectra of cluster with 6 spins based on ED calculations. The dashed lines represent the TBOT calculations up to order 80, which gives an approximate value of the convergence radius. Right: NLCE data compared with ED data for the energy gap.

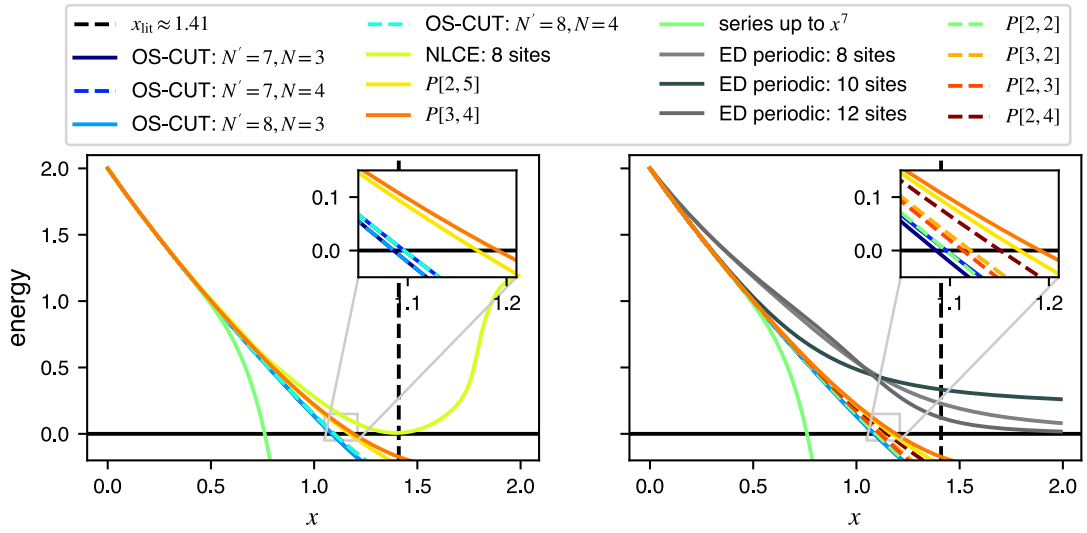

Figure 44: Left: Modified OS-CUT compared with NLCE and series expansion. Right: The gap is compared to different Padè's of series up to different orders. In general, one sees, that the critical point moves to the right, if high orders of the series are taken into account. Moreover, the Padè $P[2,2]$ is close to the data obtained from the modified OS-CUT approach.

4.5. Cross Stitch strip

The last lattice strip under investigation is the cross-stitch strip, shown in fig. 45. Here, we briefly present the NLCE data, since the NLCE results do not provide new insights into the method. The reason why we present this model nevertheless is that it completes, in a sense, our small overview of 1D strips. As we will see, a special and well-known property, flat bands, occurs due to its geometry.

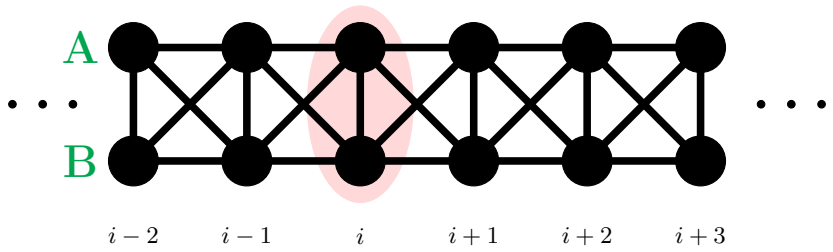

Figure 45: Lattice structure for the cross-stitch model (often named also as tetrahedral model).

Similar to the previous two models (the saw-tooth and ANNNI model), the lattice consists out of triangles. As for the ANNNI model, the ground-state manifold is not an extensive quantity. In fact, apart from the $\mathbb{Z}_2$ symmetry, the system has only one ground-state configuration as shown in fig. 46.

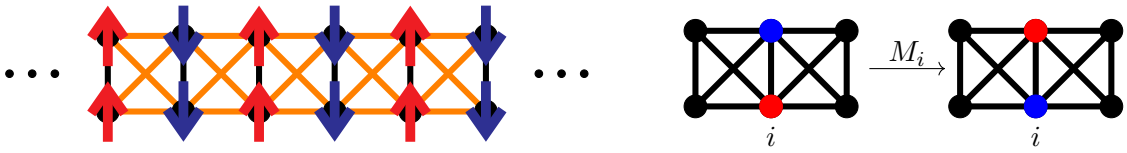

Figure 46: Left: Lowest excitation for antiferromagnetic coupling. Right: Schematic sketch of the local excitation (the different colors blue and red represents different signs).

Like all the other models before, the system undergoes a second-order phase transition, as indicated by a closing energy gap, as seen in fig. 47. Up to system sizes of 4 dimers, no effect of avoided crossings regarding the energy gap could be observed. For better comparison, the series expansion is calculated by applying TBOT. The corresponding

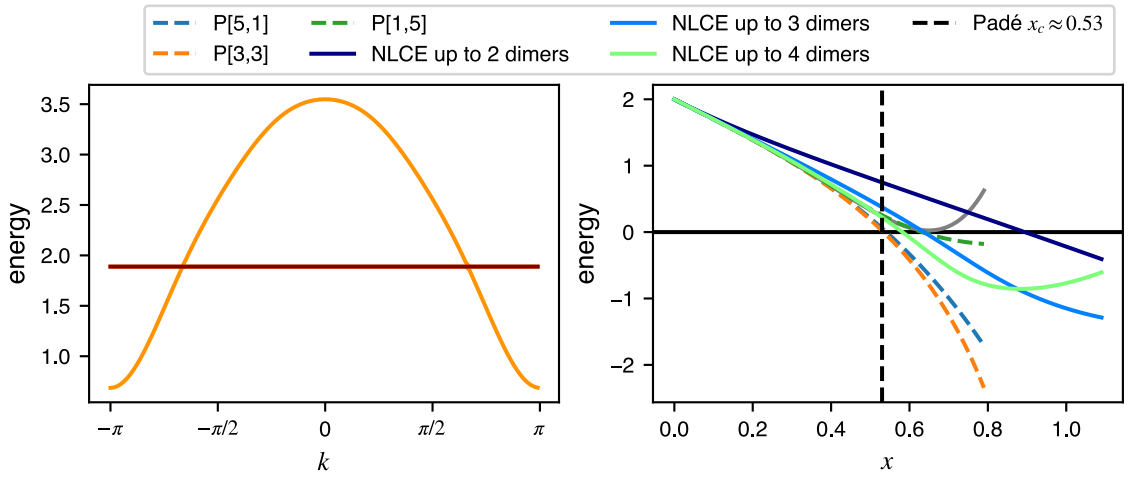

Figure 47: Left: Dispersion of the cross-stitch ladder, obtained by NLCE calculations. Right: Energy gap based on NLCE calculations and Padè's of the series. The black-dashed line represents the critical point obtained by the Padè's.

expansion for the two bands are:

$$\epsilon_1(k=\pi) = 2 - 3x + 0.25x^2 - 3x^3 + 2.234375x^4 - 7.5625x^5 + 15.5332031x^6 \tag{4.64}$$

$$\epsilon_2(k) = 2 - x + 2.25x^2 - 3x^3 + 6.984375x^4 - 12.375x^5 + 29.0644531x^6 \tag{4.65}$$

$$- 60.7695313x^7 + 146.29657x^8 - 341.142822x^9 \tag{4.66}$$

$$+ 857.451347x^{10} - 2159.68823x^{11} + 5669.32767x^{12} - 15060.3249x^{13}. \tag{4.67}$$

A comparison of NLCE with the Padè approximation of the calculated series up to order 6 leads to values around $x_c \approx 0.53$ (in comparison: NLCE up to 4 dimers leads to $x_c = 0.58 \pm 0.01$).

A significant difference to the other models so far is the presence of a flat band in the spectra. In principle, there are different ways to motivate such a property: By considering the situation in k-space, one can imagine a state with infinite mass, localized due to the lack of mobility. In a real-space description, one can interpret it as a state where all hopping processes interfere destructively. To determine the localized state, the

first-order perturbation theory is used:

$$P_1 V P_1 = \sum_i b^\dagger_{A,i} b_{A,i+1} + h.c. + b^\dagger_{B,i} b_{B,i+1} + h.c. \tag{4.68}$$

$$+ \sum_i b^\dagger_{A,i} b_{B,i+1} + h.c. + b^\dagger_{A,i+1} b_{B,i} + h.c. \tag{4.69}$$

$$+ \sum_i b^\dagger_{A,i} b_{B,i} + h.c. \tag{4.70}$$

$$\overset{F.T.}{=} \sum_k 2\cos(k)\big(b^\dagger_{A,k} b_{A,k} + b^\dagger_{B,k} b_{B,k}\big) + \big(b^\dagger_{A,k} b_{B,k} + h.c.\big)(1 + 2\cos(k)) \tag{4.71}$$

$$= \sum_k \begin{pmatrix} b^\dagger_{A,k} & b^\dagger_{B,k} \end{pmatrix} \begin{pmatrix} 2\cos(k) & 1 + 2\cos(k) \\ 1 + 2\cos(k) & 2\cos(k) \end{pmatrix} \begin{pmatrix} b_{A,k} \\ b_{B,k} \end{pmatrix}. \tag{4.72}$$

By diagonalizing the matrix, one gets to the solution:

$$|\psi_1\rangle = \frac{1}{\sqrt{2}}(b^\dagger_{A,k} - b^\dagger_{B,k})\,|0\rangle \qquad \text{with } \epsilon_1(k) = -1 \tag{4.73}$$

$$|\psi_2\rangle = \frac{1}{\sqrt{2}}(b^\dagger_{A,k} + b^\dagger_{B,k})\,|0\rangle \qquad \text{with } \epsilon_2(k) = 4\cos(k) + 1. \tag{4.74}$$

As it can be seen, the eigenvector $|\psi_1\rangle$ has an k-independent energy. By applying a Fourier-transformation, the localized state can be written in real-space as

$$|\psi_1\rangle = \frac{1}{\sqrt{2}}\big(\,|A,i\rangle - |B,i\rangle\,\big). \tag{4.75}$$

An interesting question is always whether the band is flat only for finite orders, or if this is a general property. For example, the localized state of the TFIM in the kagome lattice is flat up to order 7 [6]. A direct way to show that a state is localized for all orders is to show that it is a general eigenstate of H_{eff}. To show this, we make use of the symmetries of the lattice.
One important symmetry of the lattice is that it is invariant under the transposition of the sites inside the unit cell:

$$\tilde{M}_i\,|i,A\rangle = \tilde{M}_i\,|i,B\rangle \quad \text{and} \quad \tilde{M}_i\,|i,B\rangle = \tilde{M}_i\,|i,A\rangle \tag{4.76}$$

$$\tilde{M}_i\,|j,A\rangle = |j,A\rangle \qquad \text{for } j \neq i, \tag{4.77}$$

$$\tilde{M}_i^2 = \mathbb{1} \qquad \Rightarrow \text{spec}(\tilde{M}_i) = \{\pm 1\}. \tag{4.78}$$

By applying M_i to each unit cell sequentially, one obtains the mirror symmetry M_M along the horizontal axis. As a starting point for the effective Hamiltonian in the momentum basis, we take the most general form

$$H_k = \begin{pmatrix} A & D \\ C & B \end{pmatrix}, \tag{4.79}$$

with $A, B, C, D \in \mathbb{C}$. Thus, due to the invariance under M_M, it follows:

$$H_k \stackrel{!}{=} M H_k M = \begin{pmatrix} B & C \\ D & A \end{pmatrix} \rightarrow H_K = \begin{pmatrix} A & C \\ C & A \end{pmatrix}. \tag{4.80}$$

As a consequence, the resulting matrix only have real-valued entries. As a second step, the symmetry M_i is considered. This implies that any hopping amplitude from state $|i, A\rangle$ to $|j, A\rangle$ ($|j, B\rangle$) is equal to the hopping amplitude from $|i, B\rangle$ to $|j, A\rangle$ ($|j, B\rangle$) for $i \neq j$. After the Fourier transformation, the following equation holds

$$A = C - 1. \tag{4.81}$$

The additional offset of 1 comes from the hopping inside the unit-cell. Consequently, the matrix H_k can be written as

$$H_k = \begin{pmatrix} A & A+1 \\ A+1 & A \end{pmatrix}, \tag{4.82}$$

which leads always to an eigenstate which is not dependent of A.
Another way to see that the system contains a localized state for infinite orders is described in [6]. It points out that a state is localized up to order n if the corresponding hopping processes, which contain a closed loop for both $|i, A\rangle$ and $|i, B\rangle$, are topologically equivalent.
Here, we want to note again, that this property is well-known and described e.g. in [64]. Another well-studied spin model in 1D, that has a flat-band is the diamond chain [65].

5. XXZ model

In the previous section, we focused on the transverse field Ising model on different lattice strips. In the following section, the XXZ model (or bound-state model) will be studied primarily using NLCE and TBOT. One of the reasons why this system is interesting is the existence of an analytic solution for the 1D case, obtained by an Bethe ansatz. As with the TFIM, analytic systems give the opportunity to gain a deeper understanding of the method, especially regarding arising problems.
The structure of the description of the model is similar to that in the master thesis of Maximilian Bayer (see [66]), where a Green's function method was used to obtain insights into multiparticle bound states. After introducing the model based on the 1D case, we apply NLCE to obtain information about the bound state in this framework. Here, we will see that similar problems associated with avoided crossings, as in the previous sections, occur. This study is then expanded to the 2D and 3D cases of the model.

5.1. XXZ model in 1D

The XXZ model in the studied case takes the specific form

$$H_{\mathrm{XXZ}} = \sum_{<i,j>} \sigma_i^z \sigma_i^z + x \sum_{<i,j>} \left(\sigma_i^x \sigma_{i+1}^x + \sigma_i^y \sigma_{i+1}^y.\right) \tag{5.1}$$

By rewriting the Hamiltonian into hard-core bosons and bringing it into a more suitable form (neglecting offsets and scaling factors), the Hamiltonian can be written as:

$$H = -\sum_i n_i n_{i+1} + x \sum_i \left(b_i^\dagger b_{i+1} + b_i b_{i+1}^\dagger\right) \tag{5.2}$$

where the index i denotes the lattice sites.

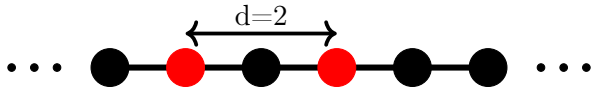

Figure 48: Schematic representation of the XXZ model in 1D. The red-marked lattice sites denote excitations. Bound states exist only for $d = 1$.

As can be clearly seen, we can divide the system into a purely hopping part ($b_i^\dagger b_{i+1}$ + h.c.) and a density-density part ($n_i n_{i+1}$). Consequently, the Hamiltonian is particle number conserving. In the case with only one particle in the system, only the hopping part is relevant, and the Hamiltonian can be diagonalized by applying a Fourier transform, leading to the dispersion:

$$\epsilon^{\mathrm{1QP}}(k) = 2x\cos(k). \tag{5.3}$$

In the two-particle sector, the $n_i n_{i+1}$ term leads to bound states, i.e., states consisting out of two directly neighbouring excitations ($d = 1$ in fig. 48). In fig. 49, a sketch of the

dispersion relation is shown. The grey area marks the 2QP continuum (states that are no bound states), which can be determined based on the 1QP dispersions:

$$\omega^{\mathrm{2QP}}(K) = \{\omega(k_1) + \omega(k_2) | k_1 + k_2 = K\}, \tag{5.4}$$

with K the total momentum. Consequently, the lower continuum edge in the 1D case is given by

$$\begin{aligned} \omega^{\text{lower edge}}(K) &= \min_{k_1,k_2}\{\omega^{k_1}(k_1) + \omega^{\mathrm{1QP}}(k_2) | k_1 + k_2 = K\} && (5.5)\\ &= 2x(\cos k_1 + \cos k_2) && (5.6)\\ \rightharpoonup \omega^{\text{lower edge}}(0) &= -4x. && (5.7) \end{aligned}$$

As we will see later in the NLCE calculations, the $K = 0$ mode is important, since it is the first mode which decays into the continuum (see fig. 49).
To gain more insight into the 2QP states, the basis is changed to the more suitable total momentum space

$$|K, d\rangle = \sum_{\nu} \exp\left\{ i\left(\nu + \frac{d}{2}\right) K \right\} |\nu, \nu + d\rangle \,, \tag{5.8}$$

with K the total momentum and ν denoting the lattice sites. In this basis, the Hamiltonian can be written as

$$H_K = \begin{pmatrix} -1 & 2x\cos\left(\frac{K}{2}\right) & 0 & \cdots \\ 2x\cos\left(\frac{K}{2}\right) & 0 & 2x\cos\left(\frac{K}{2}\right) & \\ 0 & 2x\cos\left(\frac{K}{2}\right) & 0 & \ddots \\ \vdots & 0 & \ddots & \ddots \end{pmatrix}, \tag{5.9}$$

where the basis set is ordered with increasing d ($\{ |K,1\rangle, |K,2\rangle, \cdots \}$). The energy of the bound state is given by

$$\omega^{\mathrm{bound}}(K) = -1 - x^2(2 + 2\cos(K)) \qquad \text{for } x < \left| \frac{\sin K/2}{\sin K} \right|, \tag{5.10}$$

with the corresponding eigenstate:

$$|\mathrm{bound}\rangle\,(K) = \sqrt{1 - \left(2x\cos\left(\frac{K}{2}\right)\right)^2} \sum_{d=1}^{\infty} \left(2x\cos\frac{k}{2}\right)^{d-1} |K, d\rangle \,, \tag{5.11}$$

which can be obtained via a Bethe Ansatz (see [66] for an explicit calculation). As shown in the sketch, the bound state generally lies above the continuum and exists only for a finite interval of K values. For the other values, the bound state intrudes into the continuum and decays. Therefore, the energy dispersion and state are only valid for

$$\omega^{\mathrm{bound}}(K) < 4x|\cos K| \Leftrightarrow x < \left| \frac{\sin K/2}{\sin K} \right|. \tag{5.12}$$

It is important to note that the energy of the bound state is exact up to second order. In other words, all the information about the bound states for all K values is already contained in a cluster with 3 sites. This is similar to the TFIM on a chain, where the gap is already obtained on a dimer. However, for this model, the trimer contains the information for all K values and not only for a specific one.
The general goal of our investigation is twofold: On the one hand, we want to study if and how the decay of states into the continuum affects the calculations with NLCE. As we will see, this is related to the avoided level crossings introduced in section 3. On the other hand, we are interested in how these problems can be solved for this system concretely, and how one could generalize this to other models (e.g. the lattice strips discussed in the previous chapter). However, this question is not yet answered, the following discussion explains the underlying problems in detail.

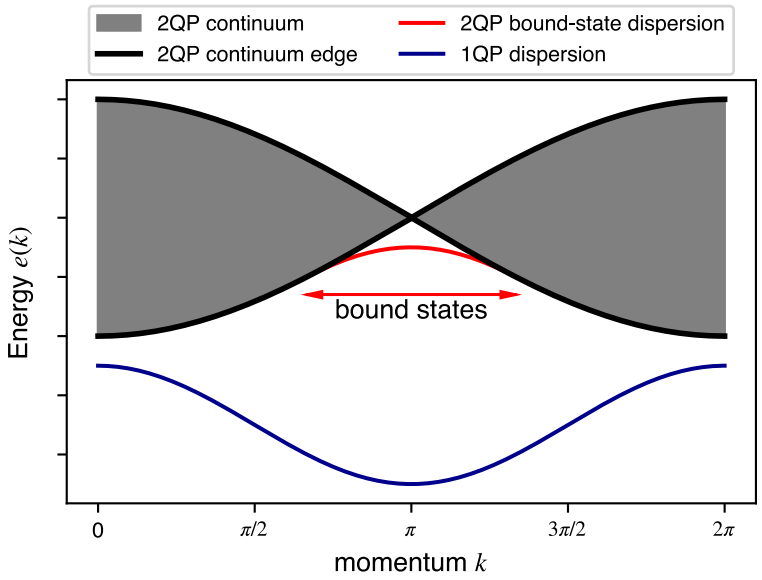

Figure 49: Illustration of the energies of the 1QP and 2QP blocks of the XXZ model in one dimension. As shown, the bound states decay into the continuum for certain k and x values. An offset was added to the one-particle dispersion to better distinguish the different lines in the plot.

5.1.1. NLCE calculation

As mentioned previously, eq. (5.11) and eq. (5.10) are only valid for certain x and k values because otherwise the bound states decay into the continuum. By applying NLCE calculations for $x \in [0, 0.5]$, one obtains convergent results for all k values (see fig. 50). This aligns with the fact that for $x < 0.5$, no mode decays into the continuum. In contrast, for $x > 0.5$, k modes, starting with $k = 0$, begin to decay into the continuum, and they can no longer be described by eq. (5.10) and eq. (5.11). This decay is observed

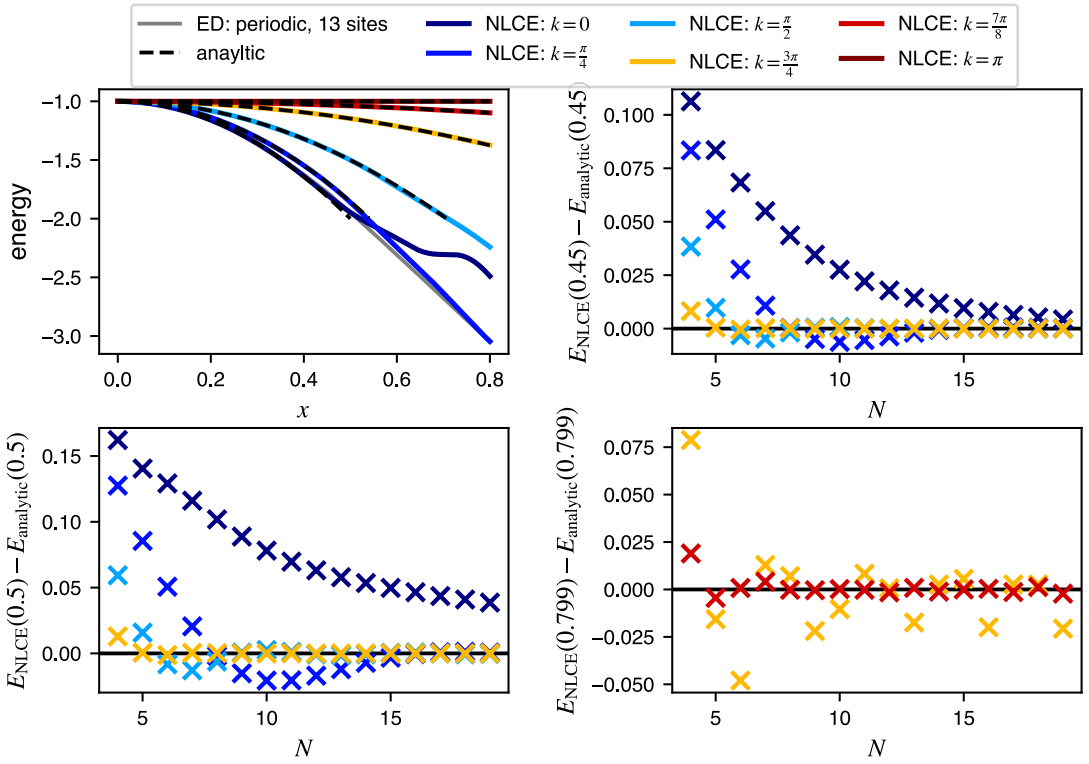

Figure 50: Upper left: NLCE calculations for 6 different k modes compared with their analytical result (black-dashed line). The other plots shows the convergence of NLCE with respect to the considered system sizes N at different k values. For $x = 0.45$ all modes show nice convergence behaviour towards the analytical result. For $x > 0.5$ the convergence gets slower.

in the NLCE data based on the convergence behaviour. For example, at $x = 0.5$, the $k = 0$ mode shows only a slow convergence, in comparison to $x < 0.5$. For values above $x = 0.5$, no convergence for $k = 0$ is observed, which aligns with the decay, as the introduced local particle picture is no longer valid after the decay. This observation can also be understood based on avoided crossings (see [39]). In principle, the decay is not directly visible on finite clusters, as finite clusters always have well-defined eigenstates. Therefore, one cannot directly observe that the bound state in the thermodynamic limit at $k = 0$ is no longer normalizable for $x > 0.5$:

$$\sqrt{1 - \left(2x \cos\left(\frac{0}{2}\right)\right)^2} = \sqrt{1 - 4x^2} \overset{x=0.5}{=} 0. \tag{5.13}$$

However, on finite clusters, one experiences an energetic overlap of the higher lying states (continuum states). This means that after $x = 0.5$ the states are no longer sufficiently separated, but rather, states of the continuum and the bound states are mixed with

respect to the initial particle picture. In other words, one again observes avoided crossings on the finite clusters. The main difference from the avoided crossings discussed in the previous sections (e.g., ANNNI model or saw-tooth chain) is that, in this case, the avoided crossings are related to the physical system in the thermodynamic limit and are not artifacts of the missing translational symmetry. Moreover, it is important to note, that this system obeys particle conservation which is not the case for the TFIM discussed before. Therefore, also underlying Hilbert spaces are different in their dimensions. However, the reason the transformation leads to a divergent result remains similar.
So far, the physical process in the thermodynamic limit can be clearly seen in the NLCE calculations. Interestingly, the decays also influence k modes with $\omega^{\text{bound}}(k) < 4x|\cos k|$, i.e. modes which still fulfill the condition of eq. (5.11) and eq. (5.10). The reason for this is the same as why the other modes diverge in our calculations: To determine T, the corresponding eigenvectors are tracked adiabatically. However, since some of the k modes have already decayed (avoided level crossing), states are considered that no longer describe the corresponding physics. In other words, the local particle picture used for $x < 0.5$ can no longer separate the bound and continuum states in a proper way. The consequences regarding the transformation can be seen in fig. 52. Here, the spectrum of the red-marked part of the transformation

$$T_n = \sum_{k \in s_n} X_{i,k} \left(X_{s_n}^{P_n \dagger} \left(X_{s_n}^{P_n} X_{s_n}^{P_n \dagger} \right)^{-1/2} \right) \tag{5.14}$$

is plotted (compare section 3.3). As shown, the lowest energies begin to decay towards zero around $x = 0.5$, leading to a breakdown of the transformation and the emergence of nonphysical dressed states $e^S |1\rangle$. This can be also seen in a significant increase of $\|T - \mathbb{1}\|$.
To summarize briefly, the main issue here is that the actual decay of modes in the thermodynamic limit leads to avoided crossings on the clusters, causing convergence problems even for states with $\omega^{\text{bound}}(k) < 4x|\cos k|$. Since the general problem is similar to the artificial avoided crossings, we attempted to use S from the trimer, as described in section 3.3, to determine the corresponding (diabatic) states. As shown in fig. 52, the states from $1 - P$ (P projects into Ω) are also used to construct T, and the resulting spectrum of $X_{s_n}^{P_n} X_{s_n}^{P_n \dagger}$ decays partially less fast. Unfortunately, however, the resulting NLCE calculations do not lead to significant improvements regarding the convergence. Thus, the question remains whether it is possible to construct T such that one obtains well-converging NLCE data for the bound states in the $x > 0.5$ regime. Moreover, since all the information about the dispersion is already contained on the trimer, the question is, how this can be extracted efficiently.

To gain another perspective on the problem, the overlap between the unperturbed and perturbed bound state is investigated more closely. As shown in an illustrative example in section 2.1, H_{eff} acts on the unperturbed Hilbertspace $\mathcal{H}_0$. However, the perturbed states are a superposition of states from the entire Hilbert space (dressed states, see

eq. (5.11)). From the analytical expression of the bound state, the overlap is given by

$$\frac{1}{2\pi}\int_0^{2\pi}\langle 1|\text{bound}\rangle\,(K)\mathrm{d}K=\int_0^{2\pi}\sqrt{1-\left(2x\cos\frac{K}{2}\right)^2}\,\mathrm{d}K. \tag{5.15}$$

This quantity can also be calculated via NLCE, by calculating $\langle 1|\,T\,|1\rangle$, since it is cluster additive. To see the cluster additivity, one can follow the same idea as in section 2.3, where we described the idea of Gelfand to obtain a cluster additive one-particle effective Hamiltonian. Therefore, we consider two disjoint clusters A and B. A bound state is either on cluster A or or on cluster B. If cluster A contains the bound state, when no excitation is on cluster B, and vice versa. Thus, the bound state can be written as:

$$|1\rangle_{A\cup B}=|1\rangle_A\otimes|0\rangle_B \qquad \text{or} \qquad |1\rangle_{A\cup B}=|0\rangle_A\otimes|1\rangle_B \tag{5.16}$$

with $|1\rangle$ and $|0\rangle$ denoting the bound state and no excitation (0QP) respectively. Based on this idea, one can write:

$$\begin{aligned}
\langle 1|\,T\,|1\rangle &= \langle 1|_A\otimes\langle 0|_B\,(T_A\otimes T_B)\,|1\rangle_A\otimes|0\rangle_B && (5.17)\\
&\quad+\langle 0|_A\otimes\langle 1|_B\,(T_A\otimes T_B)\,|0\rangle_A\otimes|1\rangle_B && (5.18)\\
&= \langle 1|_A\,T_A\,|1\rangle_A\,\langle 0|_B\,T_B\,|0\rangle_B+\langle 0|_A\,T_A\,|0\rangle_A\,\langle 1|_B\,T_B\,|1\rangle_B && (5.19)\\
&= \langle 1|_A\,T_A\,|1\rangle_A+\langle 1|_B\,T_B\,|1\rangle_B\,, && (5.20)
\end{aligned}$$

which demonstrates the cluster additivity. Terms like $\langle 0|_A\,T_A\,|1\rangle_A$ vanish because the Hamiltonian is particle-conserving. For the same reason, it holds that $\langle 0|_B\,T_B\,|0\rangle_B=1$. In fig. 51, the calculation shows that the quantity converges up to $x=0.5$, which indicates that the used local particle picture holds for that regime, as no k-mode is decayed and no avoided crossing occurs.

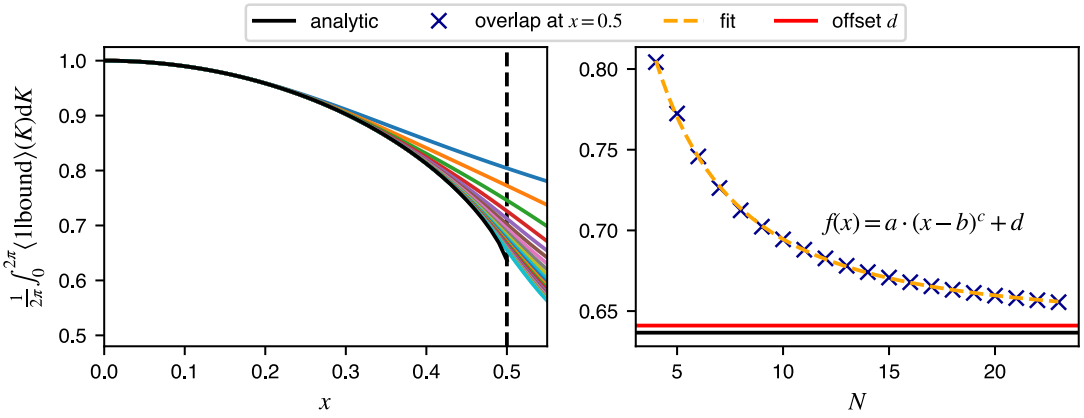

Figure 51: Left: The overlap between the unperturbed bound state and the dressed state is calculated via NLCE. The black curve represents the analytic result eq. (5.15). As shown, the NLCE data converges up to $x = 0.5$. Right: The NLCE values at $x = 0.5$ are plotted against their corresponding system size. The fit illustrates that the data converges well.

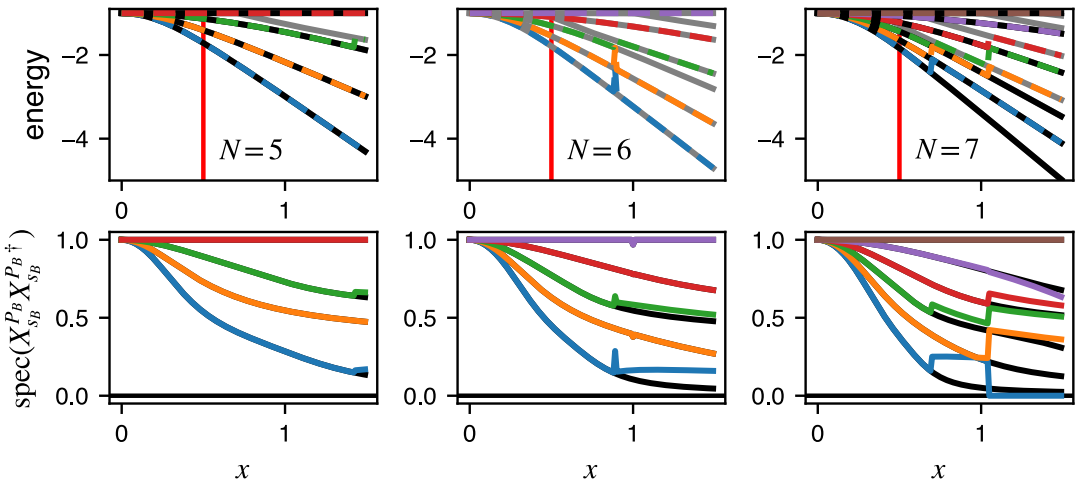

Figure 52: Top row: Energy spectra for different finite clusters of size N. The black and grey lines denotes the states associated to Ω and $1-\Omega$ (Ω represents the space of bound states). Both lines are calculated via ED. The colored dashed line represents the levels obtained by embedding S from smaller clusters (see section 3.3). As can be seen, levels from Q are obtained. Lower row: Spectra for the red-marked part in eq. (5.14). The colors represent the same states as in the top row.

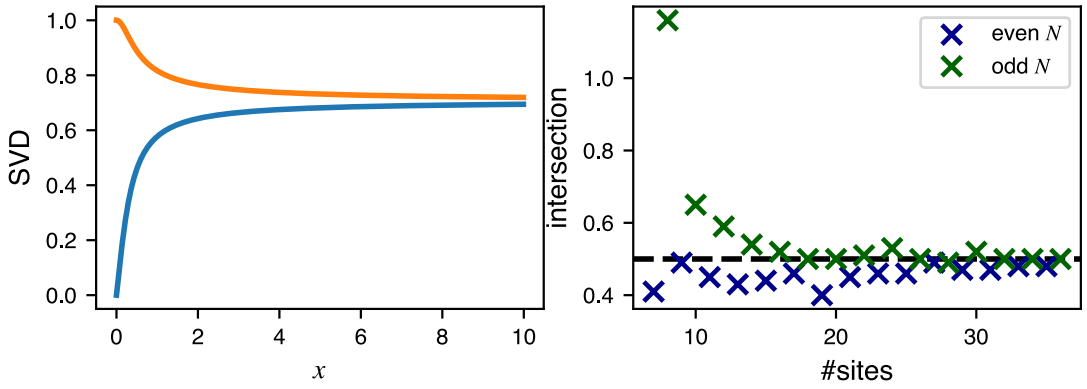

Figure 53: Left: weight of the highest bound state and lowest unbound state on a cluster with 3 sites obtained by singular value decomposition. Since the lines are not crossing, there is no intruder state. Right: The weights of the highest bound state and the next higher lying states is determined by singular value decomposition. The intersection point is shown over the size of the associated periodically coupled system. As can be seen, for large system, the value converges to $|x| = 0.5$, which corresponds to the point, where the $k = 0$ mode decays into the continuum.

5.1.2. Exceptional Points

So far, we have seen that the decay of k modes disturbs the convergence of the other k modes. Because the decay occurs in the thermodynamic limit, an energetic overlap of states (avoided crossing) arises on finite systems. Since such avoided crossings are associated with exceptional points in the complex plane (section 3), the aim is to study them more closely by determining their positions. The initial hope was that the resulting knowledge could improve our understanding of the system. However, before continuing, we will briefly discuss the three-sited cluster. As mentioned in the previous section, the cluster was used to determine the diabatic transitions (see fig. 52). Using its spatial symmetries, the Hamiltonian can be reduced to:

$$H = \begin{pmatrix} 0 & V \\ V & -1 \end{pmatrix}, \tag{5.21}$$

with $V = \frac{2}{\sqrt{2}}x$ and exceptional points at $(0, \pm\frac{i}{\sqrt{8}})$. The exceptional points also match the convergence radius, which is determined by a Taylor expansion of the energy levels, as expected. However, the cluster does not lead to the problems of avoided level crossing as described in section 3. This can be verified by determining the overlap of both states via a singular value decomposition (SVD). As shown in fig. 53, the corresponding singular values do not cross, which indicates that the weight of the bound state remains on the adiabatically connected one.

In contrast, if one does the same for a periodic coupled lattice with respect to the

$k = 0$ mode, one sees that the singular values lead to an intersection point. In fig. 53, the position of these intersections as a function of the system size is shown. For large systems, the value of 0.5 is reached, which matches with the value of decay of the $k = 0$ mode in the thermodynamic limit.

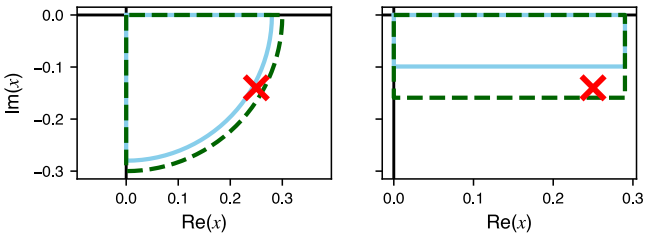

Figure 54: Sketch, how the position of the EPs were determined.

To gain deeper insight into the avoided crossings of this system, we will determine the position of the exceptional points x_{EP}. To achive this, we will use the Hamiltonian in $|K, d\rangle$ basis (denoted as H_k). To determine the position x_{EP}, we take advantage of the topological properties of EPs, specifically that encircling one leads to a permutation in the eigenvalue spectrum. Consequently, we chose a curve $g(\varphi) : [0, 1] \to \mathbb{C}$ with $g(0) = g(1) = z_0$, where z_0 is the starting point. By following the curve adiabatically, one obtains at $\varphi = 1$ the same spectra ($\mathrm{spec}\{H(g(0))\} = \mathrm{spec}\{H(g(1))\}$), but not in the initial order, if the closed loop contains EPs. The number of transpositions allows us to determine the number of exceptional points within the closed path $g(\varphi)$. We will use this method to determine the locations of the points by setting $z_0 = (0, 0)$ and having a set of curves $g_n(\varphi)$, which are parameterized by an angle and a fixed radius r_n in one of the quadrants (see left side of fig. 54). The curve g_n where a permutation in the lowest energy occurs identifies the radial component of the exceptional point. With an appropriate second curve $h_n(\varphi)$ (see right side of fig. 54), one can then determine $\mathrm{Im}(z_{\mathrm{EP}})$ and, consequently, the position z_{EP}.
To track each energy value adiabatically, we used, in principle, the method mentioned in the appendix of [67]. In short, the idea is based on using Rayleigh-Schrödinger perturbation theory up to second order to predict the energy values at $x + \Delta x$. These energy values are used to sort the exact values at $x + \Delta x$ obtained via ED.

The right side of fig. 55 shows $\min_{i,j}(|\lambda_i - \lambda_j|)$, where λ_i represents the eigenvalues of the Hamiltonian $H_k(x)$ with size $d = 24$. The idea behind this is that at exceptional points $x = x_{\mathrm{EP}}$, the eigenvalues are degenerate and having a square-root behaviour around them. Consequently, based on this color plot, one can identifies directly potential EPs (the dark points aligned in an a circular shape around the origin). By examining the spectrum of each of these points, one sees that every point is an EP associated with the lowest energy value (bound state). By tracking, for each model size $d = N$, the EP point that have minimal distance to the real axis, fig. 55 is obtained. There, one can see that

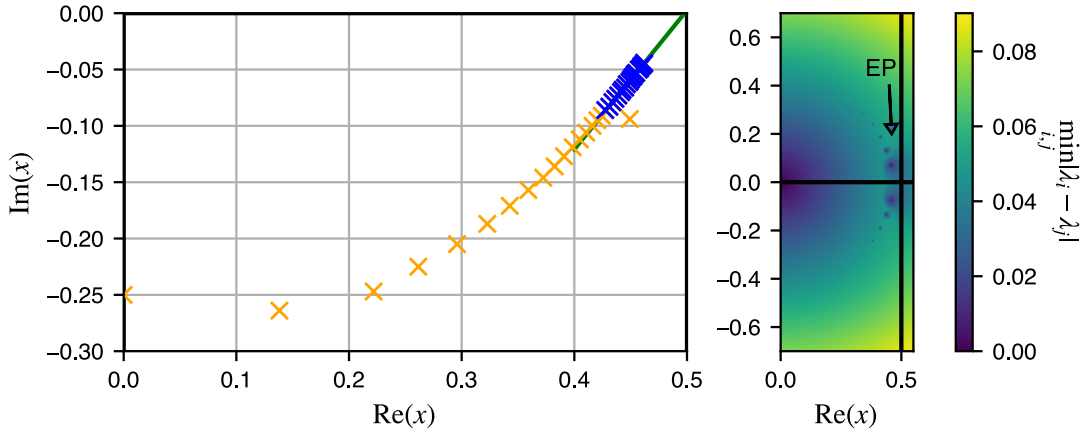

Figure 55: Left: The nearest EP to the real axis is plotted for different sizes of $H_{k=0}$. By a linear fit, one can extrapolate the trend of the data points, leading to an real value of $x = 0.5$. Right: The minimal eigenvalue distance $\min_{i,j} |\lambda_i - \lambda_j|$ is plotted for a specific system size of $H_{k=0}$. All the points are EPs related to the bound-state level. With increasing system size, the points move towards the real axis and the vertical black line (Re(x) = 0.5).

with increasing the system size, the exceptional point moves towards the real axis. A linear fit indicates that, for large systems, this EP would converge towards $x = 0.5$. The color plots in fig. 56 are generated for the $k = \pi/2$ and $k = 3\pi/4$ mode. We observe there the same pattern of exceptional points as for the $k = 0$ mode. However, in these cases, the EP closest to the real axis exists converges to $x \approx 0.707$ and $x \approx 1.306$, respectively. These points coalesced with the point where these modes decay into the continuum. This means that by studying the EPs, one can find direct connections to the physical processes. The fact that we found EPs near the x values of decay is connected, that this decay causes avoided crossings on finite systems. The interesting and yet unanswered question is whether and how one can obtain more information from the distribution of the EPs in the complex plane. In this context, it would be interesting to investigate the specific reasons why the 1D case leads to such unique patterns of EPs (see color plot). The hope is that this will lead to new insights into the system, which could help overcome the problems associated with NLCE.

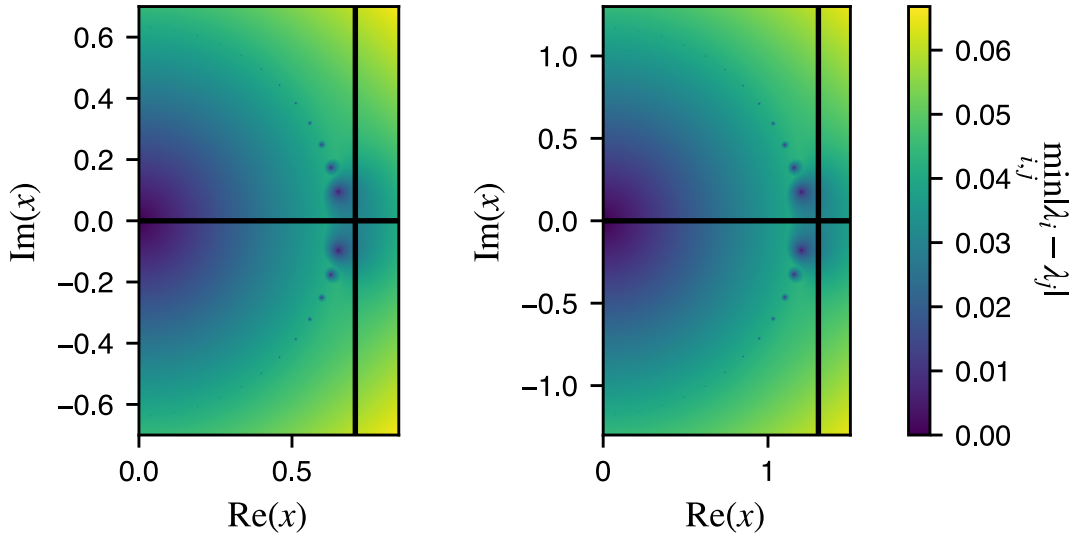

Figure 56: The minimal eigenvalue distance $\min_{i,j} |\lambda_i - \lambda_j|$ is plotted for a specific system size of $H_{k=\pi/2}$ and $H_{k=3\pi/4}$. As can be seen, the structure of the EPs stays the same as for the $k = 0$ case. With increasing system size, the points move towards the real axis and the vertical black lines, which indicates the x value of decay in the thermodynamic limit.

5.1.3. deepCUT

To view the system under another aspect, we also calculated the bound state energy with deepCUT up to second order. A detailed overview about the calculation is presented in appendix A.4.
From the resulting energy gap (fig. 57) it can be seen that deepCUT does not lead to the exact result either. However, if one calculates the Taylor expansion up to second order, the analytical expression is recovered. This behaviour was expected, since it is a fundamental property of deepCUT that its result matches the Taylor expansion up to the corresponding order.
In general, this should give a first glimpse of how other methods perform for this model. For further research, it would be interesting to see how the deepCUT results change if higher orders are taken into account. In addition, calculations with OS-CUT should be performed and compared to the deepCUT results to obtain more insights into the differences between the methods and their truncation.

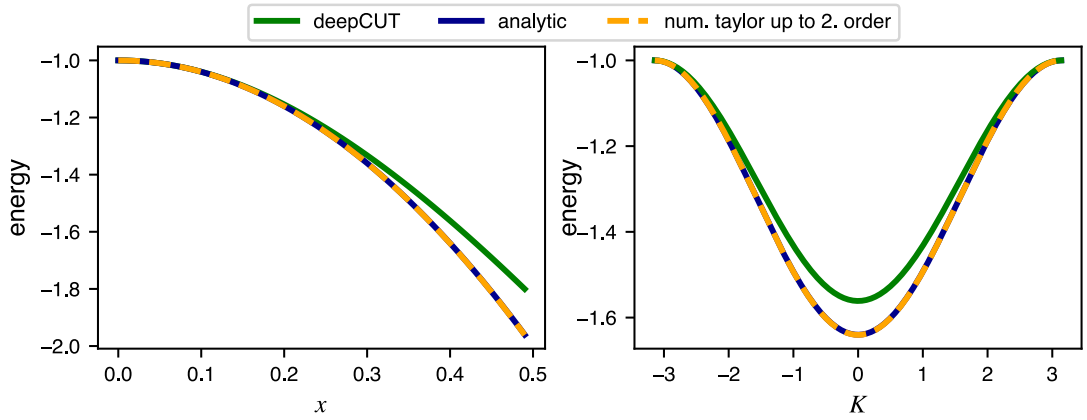

Figure 57: Left: The calculated energy of the bound state for $K = 0$ by deepCUT in comparison to the analytic result. Also, a numerical Taylor expansion was applied to the result of deepCUT up to second order. Right: Dispersion for $x = 0.4$.

5.2. XXZ Model in 2D and 3D

In this section, the model will be briefly discussed in two and three dimensions. A schematic sketch of the 2D system is depicted in fig. 58. In principle, these are only generalizations of the previous 1D case. However, an analytic solution regarding the energy gap or the bound states is not known. Similar to the 1D case, the model can be described in the $\left|K, \vec{d}\right\rangle$ basis, where $\vec{d}$ is the vectorial difference between two excitations (see fig. 58) in the unperturbed basis. The advantage of this is that the system can be described more efficiently, as it allows us to examine only specific k values. The resulting series for the 2D case, based on TBOT calculations, are:

$$\begin{aligned}\epsilon_1(x) = &-1 - 20x^2 + 96x^4 - 1536x^6 + 35328x^8 - 903168x^{10} + 24797184x^{12} \\ &- 713785344x^{14} + 21253718000x^{16} - 649215345000x^{18} \\ &+ 20230082400000x^{20} - 640552740000000x^{22}\end{aligned} \tag{5.22}$$

$$\begin{aligned}\epsilon_2(x) = &-1 - 4x^2 - 32x^4 - 512x^6 - 11776x^8 - 329728x^{10} - 10428416x^{12} \\ &- 358318080x^{14} - 13074038800x^{16} - 499285754000x^{18} \\ &- 19762212000000x^{20} - 804626048000000x^{22}.\end{aligned} \tag{5.23}$$

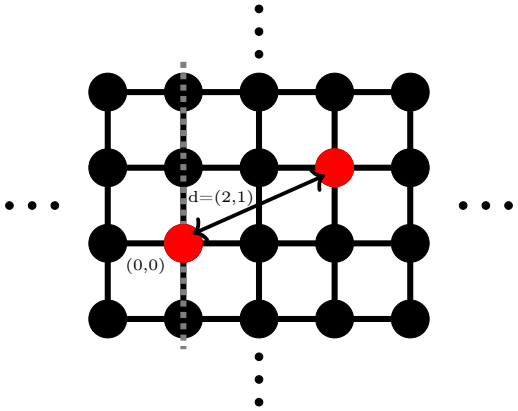

Figure 58: Schematic representation of the XXZ model in 2D. The right marked lattice-points denote excitations. Only for $d = (0, 1)$ and $d = (1, 0)$ bound states exist.

For the 3D case, we obtained:

$$\begin{aligned}\epsilon_1^{k=0}(x) = &-1 - 36x^2 - 64x^4 + 4608x^6 - 121856x^8 + 552960x^{10} + 111296512x^{12} \\ &- 5567348740x^{14} + 103036486000x^{16} + 3130622210000x^{18} \\ &- 301491726000000x^{20}\end{aligned} \tag{5.24}$$

$$\begin{aligned}\epsilon_{2,3}^{k=0}(x) = &-1 - 12x^2 - 64x^4 - 3072x^6 - 140288x^8 - 8171520x^{10} \\ &- 536330240x^{12} - 38401671200x^{14} - 2928975020000x^{16} \\ &- 234484547000000x^{18} - 1.95047895 \cdot 10^{16}x^{20}.\end{aligned} \tag{5.25}$$

Both series are plotted in fig. 59. As can be seen, similar to the 1D case, the $k = 0$ mode decays into the continuum. In contrast, in higher dimensions, the decay occurs at smaller x values. In addition to this TBOT analysis, NLCE was performed for the 2D case using rectangular clusters. As expected, the NLCE data show good agreement with the series, but breaks down after the perturbative regime.
As before, the decay can also be seen by studying the EPs, which is done briefly here for the 2D case. It should be noted that the study of EPs is only a way to gain a different understanding of the system and the connections between the different perspectives. However, up to now, it has not provided insight into how this might be helpful in solving the problems arising in the NLCE calculations.

In fig. 60, the minimal eigenvalue distance for the $|\vec{d}| = 4$ case is shown. The fact that the marked points are actual EPs is displayed in fig. 61, where the square root behaviour in the vicinity of the EP is clearly visible. In comparison to the 1D case, the 2D case does not exhibit an obvious pattern as $|\vec{d}|$ increases. This suggests that the pattern observed in the 1D case is related to the fact that the 1D case is analytically solvable. Therefore, for further studies, it would be interesting to understand the pattern of the 1D case more in detail. Since the H_K are triangular Toeplitz matrices, one idea would be to check if

there is an analytical expression for the EPs based on eq. (3.2).
However, it turns out in the 2D case, that by tracking one of the EPs related to the bound state for different system sizes H_k, one obtains fig. 60. As can be seen, with increasing system sizes, the EP moves toward the real axis and converges to $x \approx 0.139$. As in the 1D case, this is the location of the $k = 0$ decay. For further studies, it would be interesting to know, how the other EPs change. As mentioned at the beginning, this should provide a different perspective on how to think about the system in terms of EPs. Unfortunately, no new direct insights have been found yet. Therefore, the next section will summarize some open questions and suggest ideas for further examination of this model.

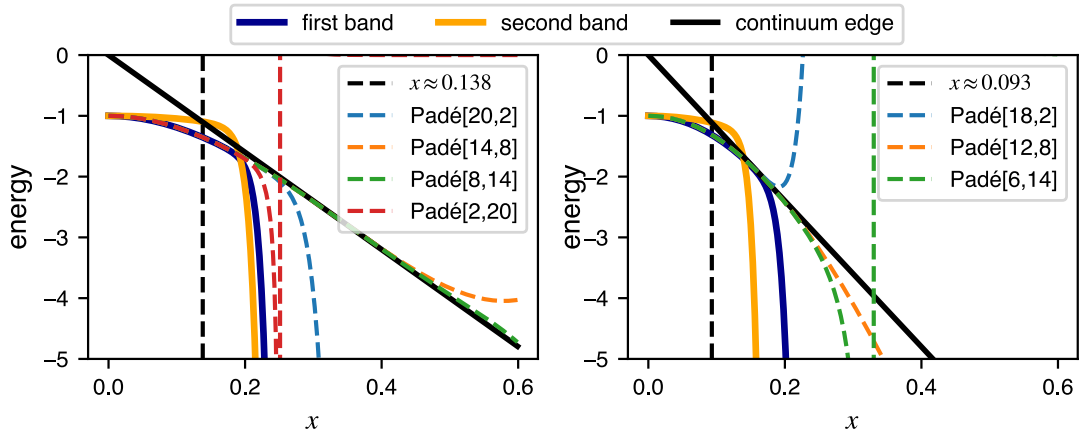

Figure 59: The series for the energy bands at $k = 0$ in 2D (left) and 3D (right) case. The black-dashed lines denotes the position, where one band enters the continuum.

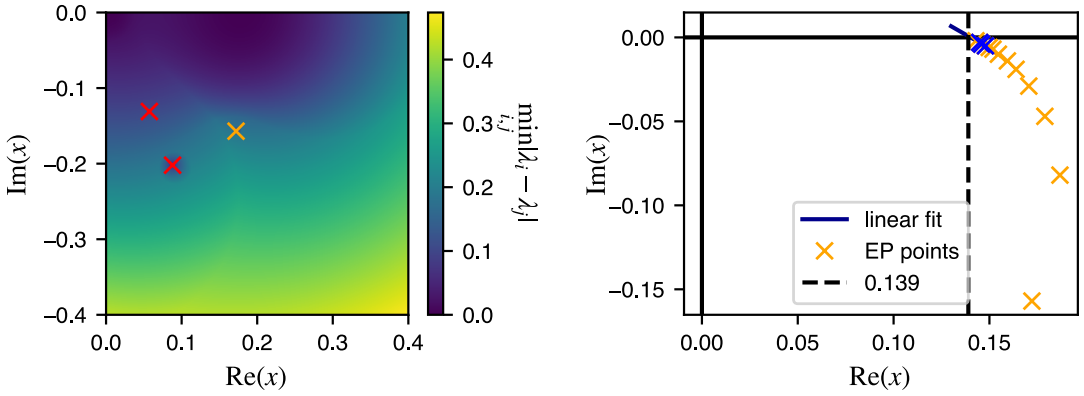

Figure 60: Left: The minimal eigenvalue distance $\min_{i,j} |\lambda_i - \lambda_j|$ is plotted up to $|\vec{d}| = 4$. The crosses mark the exceptional points. Right: One of the EPs, which is associated with one of the bound states, is determined for different d values.

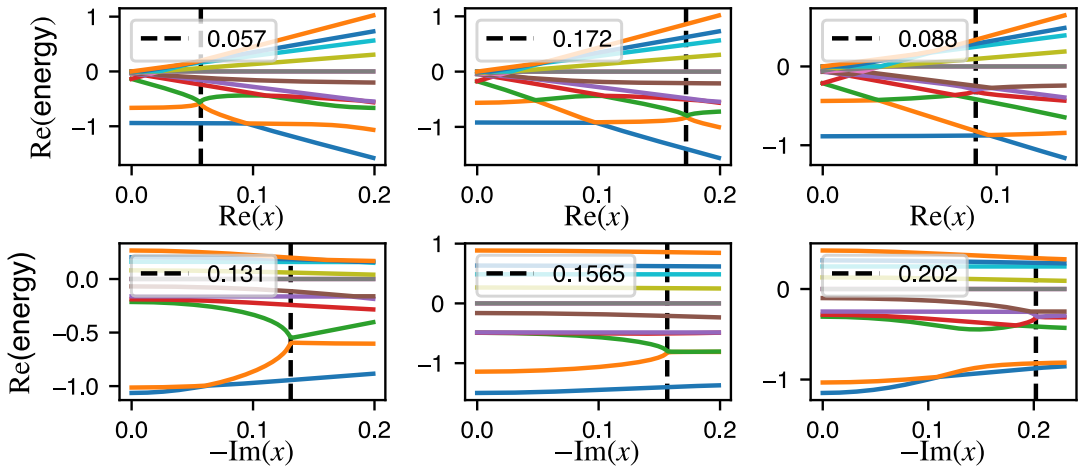

Figure 61: The real part of the energy spectra around the three EPs points $x_{\mathrm{EP},1} = 0.057 - 0.131\mathrm{i}$, $x_{\mathrm{EP},2} = 0.172 - 0.1565\mathrm{i}$ and $x_{\mathrm{EP},3} = 0.088 - 0.202\mathrm{i}$. The square-root behaviour is clearly visible for all three points.

5.3. Outlook and remaining questions

In this section, we provide an overview of possible ideas from M. Hörmann, which can be viewed as a starting point for further research. As observed from the 1D, 2D and 3D cases, the decay of $k = 0$ modes leads to convergence problems.
The overall aim would be to find a schematic way how to modify the transformation T to use only the states which contribute to the targeted quantity. As mentioned in section 3, there is strong evidence that the adiabatic transitions have to replaced by

diabatic ones. Therefore, we need a smooth transition between the states, similar to the scheme proposed by K. Cöster in the gCUT framework but without its ambiguity. To obtain a good continuation of the energy levels, M. Hörmann constructed a partner Hamiltonian, which is for $k = 0$

$$H_{\text{partner}} = \begin{pmatrix} -4x^2 & -2x & 0 & \cdots \\ -2x & 0 & \ddots & \\ 0 & \ddots & \ddots & \end{pmatrix}. \tag{5.26}$$

The corresponding eigenstate and energy is

$$|\text{partner bound}\rangle\,(K=0) = \sqrt{1 - \frac{1}{4x^2}} \sum_{d=1}^{\infty} \frac{1}{(2x)^d} |K, d\rangle \tag{5.27}$$

$$\omega^{\text{partner bound}}(K=0) = -1 - 4x^2 \qquad \text{for } x > 0.5. \tag{5.28}$$

Interestingly, the bound states of this Hamiltonian exist for $x > 0.5$ and continue the energy of the original $k = 0$ mode in a smooth way (at least up to a certain derivative). For $x < 0.5$, the $k = 0$ mode of the partner Hamiltonian decays into the continuum (see fig. 62). However, this Hamiltonian continues the original one in a smooth way beyond the decay. M. Hörmann's idea was to use this information to construct appropriate eigenstates for the transformation T that do not diverge for $x > 0.5$. However, the concrete procedure has not yet been developed.

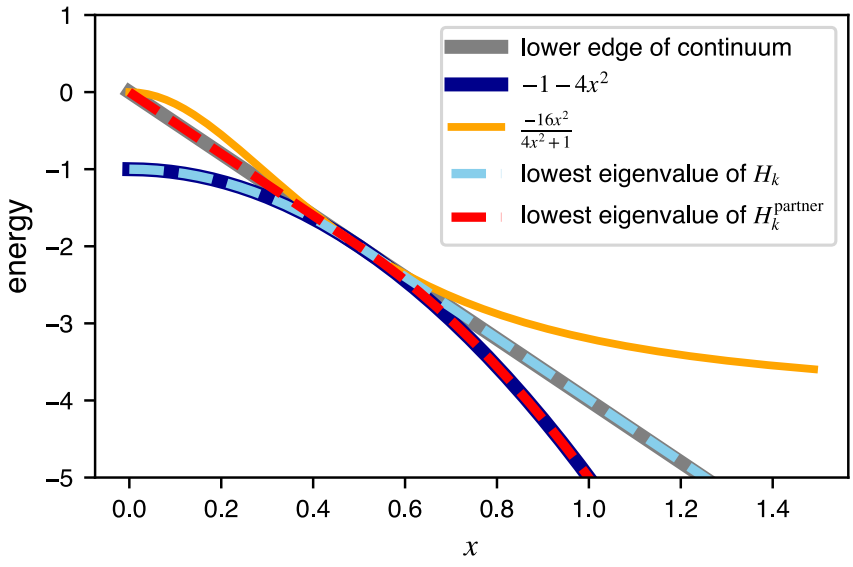

Figure 62: Both bound states of H and H^{partner} at $k = 0$ are shown. In addition, $\max_\omega -\frac{1}{\pi}\text{Im}\,\langle k, 1|\,(\omega - \mathcal{H} + i0^+)^{-1}\,|k, 1\rangle$ is given.

Another point is regarding the Green's function of the system. Since the Hamiltonian is a tridiagonal Toeplitz matrix, there exists an analytical expression for its inverse [68], allowing for direct calculations of the Greens function. An interesting quantitiy of the Greens functions is the following:

$$\max_\omega -\frac{1}{\pi}\mathrm{Im}\left\langle k,1\right|\left(\omega-\mathcal{H}+i0^+\right)^{-1}\left|k,1\right\rangle=\frac{4}{2x^2\cos k+2x^2+1}-4. \tag{5.29}$$

This quantity gives the maximal overlap between the bound state in the unperturbed basis with the states in the continuum. To better understand this expression, we first introduce some basic properties of Green's functions, based on [69]. In the spectral representation, every Green function can be written as:

$$G(z)=\sum_n\frac{\left|\phi_n\right\rangle\left\langle\phi_n\right|}{z-\omega_n}+\int\frac{\mathrm{d}\lambda}{N(\lambda)}\frac{\left|\lambda\right\rangle\left\langle\lambda\right|}{z-\omega(\lambda)}, \tag{5.30}$$

with the discrete eigenstates $|\phi_n\rangle$ and the continuous eigenstates $|\lambda\rangle$. Both sets of states are labeled by indices n and λ. The $N(\lambda)$ is only a normalization factor. In our system, the $|\phi_n\rangle$ would represent the bound states, while $|\lambda\rangle$ represents the states forming the 2QP continuum. The last term in eq. (5.30) can be rewritten as:

$$\int\frac{\mathrm{d}\lambda}{N(\lambda)}\frac{\left|\lambda\right\rangle\left\langle\lambda\right|}{z-\omega(\lambda)}=\int\mathrm{d}\omega\frac{P_\omega}{z-\omega}, \tag{5.31}$$

with

$$P_\omega=\int\frac{\mathrm{d}\lambda}{N(\lambda)}\delta(\omega-\omega(\lambda))\left|\lambda\right\rangle\left\langle\lambda\right|. \tag{5.32}$$

The P_ω can be interpreted as a projector into the continuum states with energy ω. Consequently, it follows

$$\mathrm{Im}(\left\langle u\right|G(\omega+\mathrm{i}\delta)\left|u\right\rangle)=-\pi\left\langle u\right|P_\omega\left|u\right\rangle, \tag{5.33}$$

with $|u\rangle$ being an arbitrary state. This means for eq. (5.30), that it provides the maximal overlap of our unperturbed bound state within the continuum states (see fig. 62). An Taylor expansion around $x=0.5$ of eq. (5.29) for the $k=0$ mode leads to

$$\begin{aligned}\max_\omega -\frac{1}{\pi}\mathrm{Im}\left\langle 0,1\right|\left(\omega-\mathcal{H}+i0^+\right)^{-1}\left|0,1\right\rangle&=\frac{-16x^2}{4x^2+1}\\&\approx -2-4(x-0.5)+4(x-0.5)^2+\mathcal{O}(x^3).\end{aligned}$$

As can be seen, up to second order, it matches the energy value of the bound state. A direct question would be whether such a solution can be found via NLCE. However, for this, further research would be necessary.
As mentioned at the beginning, no concrete results have been gained from these ideas yet. However, they represent an ideal starting point for further investigations.

6. Conclusion

6.1. Summary

In this project, the non-perturbative method PCAT was applied to different 1D spin systems to calculate the energy gap via a cluster expansion. For the different models the advantage of such a cluster expansion in comparison to ED calculations with regards to convergence was well seen. Moreover, the comparison between the series expansions and the results obtained by NLCE shows that NLCE can reproduce the physics within the perturbative regime in a well converging manner. Beyond, we face a divergent behaviour of the resulting energy gap. For the studied TFIM, this means that the effective Hamiltonian no longer describes the physical processes. The reason for this is the occurrence of avoided level crossings on the finite clusters. Due to them, an ambiguity arises which states should be taken into account by constructing the cluster additive transformation T. As seen in the models, the adiabatic states are unsuitable.
We denote the avoided crossings on finite clusters as artificial if they are not associated with a physical process in the thermodynamic limit but are rather an effect of the finite cluster. In comparison, we also observed non-artificial avoided crossings in the XXZ model, where the avoided crossing indicates the decay of the $k = 0$ mode. However, the consequences for the other modes are similar to those of an artificial avoided crossing, as we see that the transformation breaks down in the non-perturbative regime.
One way to reduce the effects of avoided crossings was to modify the cluster expansion, as we did for the TFIM on the saw-tooth lattice, by going from a unit-cell expansion to a triangular expansion. However, on the one hand, this is not possible for every system. On the other hand, it only reduced the effects of those crossings without solving the principle problem. Indeed, as we showed, avoided crossings also emerge nevertheless. Therefore, a systematic scheme is needed for how the problems associated with artificial avoided crossings can be overcome. A general idea, which is also mentioned in detail in the gCUT framework [39], is the replacement of adiabatic transitions by diabatic ones. As we showed for the ANNNI model, such diabatic transition can reduce the arising problems. It is important to note that the diabatic transition has to be smooth in such a way, that it is still possible to perform a cluster expansion. This means that the diabatic transition should not lead to an imbalance in the different perturbative contributions from the different clusters. In gCUT, it was tried to modify the flow equations appropriately. Here, however, we did not present a direct way, how a possible smooth diabatic transition could look like. Nevertheless, we showed that embedding of generator $S = \log T$ from smaller clusters can help to identify potential diabatic transitions.
Especially the use of S turned out to be also useful in another ansatz, namely combining PCAT with a CUT scheme. The resulting gaps showed evidence that S contains already higher orders, which is in alignment with the literature. However, the results of the presented OS-CUT like scheme indicates that this scheme and its special truncation lead to remarkable results when compared with NLCE and data from the literature.
Despite the arising problems, it should be noted that PCAT turns out to be an efficient tool, as it enables one to calculate both NLCE as well as the concrete series where

other methods, like TBOT, fail. In this way, PCAT is an excellent method to obtain information within the perturbative limit.

6.2. Outlook

The main challenge that remains is to develop a way to obtain information within the non-perturbative regime using the NLCE framework. Therefore, as mentioned above, it is essential to find a way to address (artificial) level crossing. In this context, it may be interesting to extend the study of EPs, as we briefly did in the discussion of the XXZ model. Although the XXZ model has special properties (e.g., real decay of k modes), progress there could lead to general insights, which could also help with other models.
Moreover, the modified CUT schemes should be investigated in more detail. As we saw in our investigations, the scheme led to some remarkable results. However, so far, we have only shown that this method is applicable. What remains missing is a detailed evaluation of the underlying mechanisms of this method. For instance, it would be quite important to gain more insight into its truncation and how this influences the results. It is also of interest with respect to the scaling behaviour, which was not investigated in this thesis. To obtain further progress there, it is necessary to calculate higher orders of S and evaluate their behaviour in comparison to the lower orders.
Besides these aspects of further method development, there are still open questions regarding NLCE within the perturbative limit. One important question is how to extract critical exponents. As we showed for the TFIM in the chain and ladder, a log-log plot of the spatial length shows deviations of up to 20%. One starting point would be to calculate higher orders of NLCE. This would help in understanding the course the data points follow. Hopefully, based on this, one can find a way to understand the connection to scaling. Especially obtaining the critical exponent from NLCE calculations would enlarge the field of application of NLCE.

A. Appendix

A.1. NLCE for 1D lattices

As mentioned in section 2.2, for performing a cluster expansion for 1D lattices, using clusters up to size N, one only needs to perform the calculations on clusters of size N and $N-1$. For the chain, this means that a cluster expansion up to 5 sites, only the clusters of 5 and 4 sites are needed. In principle, one can directly see that contributions from lower (reduced) clusters cancel each other out by explicitly writing down the cluster expansion, since all clusters have the same embedding factor. Nevertheless, we will briefly motivate the relation in a more formal way.
For that, we take a cluster additive quantity $\mathcal{M}(C_i)$ which is evaluated on cluster C_i. The idea of a cluster expansion is to only adding up the reduced contributions, to avoid double counting. This leads to

$$\overline{\mathcal{M}}(C_N) = \mathcal{M}(C_N) - \sum_{i=1}^{N-1} a_i \mathcal{M}(C_i), \tag{A.1}$$

with $\overline{\mathcal{M}}(C_N)$ being the reduced quantity of cluster C_N. Note, that C_i denotes cluster with i being the spatial extension in the translational invariant axis. For the chain, i would denote the number of sites. Consequently, the embedding factors a_i are takes the form of: $a_i = N - i + 1$. For the next larger cluster, the reduced element is

$$\overline{\mathcal{M}}(C_{N+1}) = \mathcal{M}(C_{N+1}) - \sum_{i=1}^{N} b_i \mathcal{M}(C_i) \tag{A.2}$$

$$= \mathcal{M}(C_{N+1}) - \sum_{i=1}^{N-1} b_i \overline{\mathcal{M}}(C_i) - 2\overline{\mathcal{M}}(C_N), \tag{A.3}$$

with $b_i = N - i + 2$ and $b_i - a_i = 1$. From this follows

$$\overline{\mathcal{M}}(C_{N+1}) - \overline{\mathcal{M}}(C_N) = \mathcal{M}(C_{N+1}) - \mathcal{M}(C_N) - \sum_{i=1}^{N-1} \overline{\mathcal{M}(C_i)} - 2\overline{\mathcal{M}}(C_N). \tag{A.4}$$

Consequently it holds

$$\mathcal{M}(\mathcal{L}_{\mathcal{N}+\infty}) = \sum_{i=1}^{N+1} \overline{\mathcal{M}}(C_i) = \sum_{i=1}^{N} \overline{\mathcal{M}}(C_N) + \overline{\mathcal{M}}(C_{N+1}) \tag{A.5}$$

$$= \sum_{i=1}^{N} \overline{\mathcal{M}}(C_N) + \mathcal{M}(C_{N+1}) - \mathcal{M}(C_N) - \sum_{i=1}^{N} \overline{\mathcal{M}}(C_i) \tag{A.6}$$

$$= \mathcal{M}(C_{N+1}) - \mathcal{M}(C_N), \tag{A.7}$$

with $\mathcal{M}(\mathcal{L}_{\mathcal{N}+\infty})$ the quantity $\mathcal{M}$ obtained by the cluster expansion up to clusters of size $N+1$. For the last step, eq. (A.4) was used. Therefore, it directly follows, that one only needs the quantity on cluster C_{N+1} and C_N. Note, that this is only valid for 1D lattices with the appropriate cluster expansion, e.g. the unit-cell expansion for a ladder.

A.2. Modified OS-CUT on trimer

Here we provide additional material regarding our calculations with the OS-CUT on the linear chain, using the trimer (see section 4.1.3). From the trimer, the general form of S can be extracted.

$$S_3 = \begin{bmatrix} 0 & 0 & 0 & -\beta & 0 & -\gamma & -\beta & 0 \\ 0 & 0 & 0 & 0 & 0 & 0 & 0 & -\beta \\ 0 & 0 & 0 & 0 & 0 & 0 & 0 & \gamma \\ \beta & 0 & 0 & 0 & 0 & 0 & 0 & 0 \\ 0 & 0 & 0 & 0 & 0 & 0 & 0 & -\beta \\ \gamma & 0 & 0 & 0 & 0 & 0 & 0 & 0 \\ \beta & 0 & 0 & 0 & 0 & 0 & 0 & 0 \\ 0 & \beta & -\gamma & 0 & \beta & 0 & 0 & 0 \end{bmatrix}.$$

Important to note, that the reduced S_3 has to be embedded on the infinite lattice. Afterwards, the equation

$$\partial_\theta H = [S, H] \tag{A.8}$$

is solved. Therefore, a self-consistent basis set is required (see table 3). The corresponding differential equations are as follows:

$$\partial_\theta h_0 = -\gamma h_6 - \beta h_3 - \beta h_2 - \gamma h_7 \tag{A.9}$$
$$\partial_\theta h_1 = 2\beta h_2 + 2\beta h_3 + 2\gamma h_6 + 2\gamma h_6 + 2\gamma * h_7 + 2\gamma h_7 - \beta h_{12} - \beta h_{13} - \gamma h_{14} \tag{A.10}$$
$$+ 2\gamma h_{14} - \gamma h_{15} + 2\gamma h_{15} - \beta h_{22} - \beta h_{23} \tag{A.11}$$
$$\partial_\theta h_2 = -2\beta h_1 - 2\gamma h_4 - 2\beta h_8 - \gamma h_{11} - \beta h_{16} - \beta h_{17} - \gamma h_{19} - \beta h_{20} \tag{A.12}$$
$$\partial_\theta h_3 = -2\beta h_1 - 2\gamma h_4 - 2\beta h_8 - \gamma h_{10} - \beta h_{16} - \beta h_{17} - \gamma h_{18} - \beta h_{20} \tag{A.13}$$
$$\partial_\theta h_4 = -\gamma h_2 + 2\gamma h_2 - \gamma h_3 + 2\gamma h_3 - \beta h_6 - \beta h_7 - \gamma h_{13} \tag{A.14}$$
$$+ 2\gamma h_{13} - \beta h_{14} - \beta h_{15} - \gamma h_{23} + 2\gamma h_{23} \tag{A.15}$$
$$\partial_\theta h_5 = -\gamma h_2 + 2\gamma h_2 - \gamma h_3 + 2\gamma h_3 - \beta h_6 - \beta h_7 - \gamma h_{12} \tag{A.16}$$
$$+ 2\gamma h_{12} - \beta h_{14} - \beta h_{15} - \gamma h_{22} + 2\gamma h_{22} \tag{A.17}$$
$$\partial_\theta h_6 = -2\gamma h_1 - 2\beta h_4 - \beta h_{10} - \beta h_{18} - \gamma h_{21} \tag{A.18}$$
$$\partial_\theta h_7 = -2\gamma h_1 - 2\beta h_4 - \beta h_{11} - \beta h_{19} - \gamma h_{21} \tag{A.19}$$
$$\partial_\theta h_8 = -\beta h_2 - \beta h_3 - \beta h_{13} - \beta h_{23} \tag{A.20}$$
$$\partial_\theta h_9 = -\beta h_2 - \beta h_3 - \beta h_{12} - \beta h_{22} \tag{A.21}$$
$$\partial_\theta h_{10} = -2\gamma h_3 + 2\gamma h_3 + 2\beta h_6 + \beta h_{14} + \gamma h_{22} - 2\gamma h_{22} \tag{A.22}$$
$$\partial_\theta h_{11} = 2\gamma h_2 - 2\gamma h_2 + 2\beta h_7 + \beta h_{15} + \gamma h_{23} - 2\gamma h_{23} \tag{A.23}$$
$$\partial_\theta h_{12} = 2\gamma h_4 - 2\gamma h_4 + 2\beta h_8 + \beta h_{16} + \gamma h_{19} - \beta h_{20} - \beta h_{21} \tag{A.24}$$
$$\partial_\theta h_{13} = 2\gamma h_4 - 2\gamma h_4 + 2\beta h_8 + \beta h_{17} + \gamma h_{18} - \beta h_{20} - \beta h_{21} \tag{A.25}$$
$$\partial_\theta h_{14} = 4\gamma h_1 + 4\beta h_4 + \beta h_{10} + \beta h_{18} - 2\gamma h_{20} + 4\gamma h_{20} + 2\gamma h_{21} \tag{A.26}$$
$$\partial_\theta h_{15} = 4\gamma h_1 + 4\beta h_4 + \beta h_{11} + \beta h_{19} - 2\gamma h_{20} + 4\gamma h_{20} + 2\gamma h_{21} \tag{A.27}$$

$$\partial_\theta h_{16} = 2\beta h_2 + 2\beta h_3 + \beta h_{12} + \beta h_{22} \tag{A.28}$$
$$\partial_\theta h_{17} = 2\beta h_2 + 2\beta h_3 + \beta h_{13} + \beta h_{23} \tag{A.29}$$
$$\partial_\theta h_{18} = 2\gamma h_3 - 2\gamma h_3 + 2\beta h_6 + \gamma h_{13} - 2\gamma h_{13} + \beta h_{14} \tag{A.30}$$
$$\partial_\theta h_{19} = 2\gamma h_2 - 2\gamma h_2 + 2\beta h_7 + \gamma h_{12} - 2\gamma h_{12} + \beta h_{15} \tag{A.31}$$
$$\partial_\theta h_{20} = -4\gamma h_6 - 4\gamma h_7 + \beta h_{12} + \beta h_{13} + 2\gamma h_{14} - 4\gamma h_{14} + 2\gamma h_{15} \tag{A.32}$$
$$- 4\gamma h_{15} + \beta h_{22} + \beta h_{23} \tag{A.33}$$
$$\partial_\theta h_{21} = \beta h_{12} + \beta h_{13} + \beta h_{22} + \beta h_{23} \tag{A.34}$$
$$\partial_\theta h_{22} = 2\gamma h_4 - 2\gamma h_4 + 2\beta h_8 + \gamma h_{10} + \beta h_{16} - \beta h_{20} - \beta h_{21} \tag{A.35}$$
$$\partial_\theta h_{23} = 2\gamma h_4 - 2\gamma h_4 + 2\beta h_8 + \gamma h_{11} + \beta h_{17} - \beta h_{20} - \beta h_{21}. \tag{A.36}$$

Based on this, one can calculate $H(\theta)$. As a next step, one needs to integrate the commutator $[S, H]$, to gain the effective Hamiltonian.

second quantization	basis term
$\mathbb{1}$	A_0
$b_i^\dagger b_i$	A_1
$b_i^\dagger b_{i+1}^\dagger$	A_2
$b_i b_{i+1}$	A_3
$b_i^\dagger b_{i+1}$	A_4
$b_i b_{i+1}^\dagger$	A_5
$b_i^\dagger b_{i+2}^\dagger$	A_6
$b_i b_{i+2}$	A_7
$b_i^\dagger b_{i+2}$	A_8
$b_i b_{i+2}^\dagger$	A_9
$b_i^\dagger b_i b_{i+1} b_{i+2}^\dagger$	A_{10}
$b_i^\dagger b_i b_{i+1}^\dagger b_{i+2}$	A_{11}
$b_i^\dagger b_i b_{i+1}^\dagger b_{i+2}^\dagger$	A_{12}
$b_i^\dagger b_i b_{i+1} b_{i+2}$	A_{13}
$b_i^\dagger b_{i+1}^\dagger b_{i+1} b_{i+2}^\dagger$	A_{14}
$b_i b_{i+1}^\dagger b_{i+1} b_{i+2}$	A_{15}
$b_i b_{i+1}^\dagger b_{i+1} b_{i+2}^\dagger$	A_{16}
$b_i^\dagger b_{i+1}^\dagger b_{i+1} b_{i+2}$	A_{17}
$b_i^\dagger b_{i+1} b_{i+2}^\dagger b_{i+2}$	A_{18}
$b_i b_{i+1}^\dagger b_{i+2}^\dagger b_{i+2}$	A_{19}
$b_i^\dagger b_i b_{i+1}^\dagger b_{i+1}$	A_{20}
$b_i^\dagger b_i b_{i+2}^\dagger b_{i+2}$	A_{21}
$b_i b_{i+1} b_{i+2}^\dagger b_{i+2}$	A_{22}

$b_i^\dagger b_{i+1}^\dagger b_{i+2}^\dagger b_{i+1}$	A_{23}

Table 3: Basis terms

A.3. OS-CUT ladder

In section 4.2.1, we presented the modified OS-CUT calculations for the ladder. The S used was obtained up to cluster C_2 in fig. 21. From the 4-spin cluster, the general shape of the finite S can be extracted as follows

$$S_4 = \begin{bmatrix}
0 & 0 & 0 & -\alpha & 0 & -\alpha & -\beta & 0 & 0 & -\beta & -\alpha & 0 & -\alpha & 0 & 0 & 0 \\
0 & 0 & 0 & 0 & 0 & 0 & 0 & 0 & 0 & 0 & 0 & -\gamma & 0 & -\gamma & 0 & 0 \\
0 & 0 & 0 & 0 & 0 & 0 & 0 & -\gamma & 0 & 0 & 0 & 0 & 0 & 0 & -\gamma & 0 \\
\alpha & 0 & 0 & 0 & 0 & 0 & 0 & 0 & 0 & 0 & 0 & 0 & 0 & 0 & 0 & -\alpha \\
0 & 0 & 0 & 0 & 0 & 0 & 0 & -\gamma & 0 & 0 & 0 & 0 & 0 & 0 & -\gamma & 0 \\
\alpha & 0 & 0 & 0 & 0 & 0 & 0 & 0 & 0 & 0 & 0 & 0 & 0 & 0 & 0 & -\alpha \\
\beta & 0 & 0 & 0 & 0 & 0 & 0 & 0 & 0 & 0 & 0 & 0 & 0 & 0 & 0 & \beta \\
0 & 0 & \gamma & 0 & \gamma & 0 & 0 & 0 & 0 & 0 & 0 & 0 & 0 & 0 & 0 & 0 \\
0 & 0 & 0 & 0 & 0 & 0 & 0 & 0 & 0 & 0 & 0 & -\gamma & 0 & -\gamma & 0 & 0 \\
\beta & 0 & 0 & 0 & 0 & 0 & 0 & 0 & 0 & 0 & 0 & 0 & 0 & 0 & 0 & \beta \\
\alpha & 0 & 0 & 0 & 0 & 0 & 0 & 0 & 0 & 0 & 0 & 0 & 0 & 0 & 0 & -\alpha \\
0 & \gamma & 0 & 0 & 0 & 0 & 0 & 0 & \gamma & 0 & 0 & 0 & 0 & 0 & 0 & 0 \\
\alpha & 0 & 0 & 0 & 0 & 0 & 0 & 0 & 0 & 0 & 0 & 0 & 0 & 0 & 0 & -\alpha \\
0 & \gamma & 0 & 0 & 0 & 0 & 0 & 0 & \gamma & 0 & 0 & 0 & 0 & 0 & 0 & 0 \\
0 & 0 & \gamma & 0 & \gamma & 0 & 0 & 0 & 0 & 0 & 0 & 0 & 0 & 0 & 0 & 0 \\
0 & 0 & 0 & \alpha & 0 & \alpha & -\beta & 0 & 0 & -\beta & \alpha & 0 & \alpha & 0 & 0 & 0
\end{bmatrix}$$

The basis states obtained, as well as the form of the embedded S is written down in a text file, which can be found her: `https://faubox.rrze.uni-erlangen.de/getlink/fiCXvsvYGYderiS6q53X9i/Basis_terms_and_S.txt`

A.4. deepCUT for XXZ model

Here, we present the calculation steps for the deepCUT calculation up to second order. The Hamiltonian was chosen in the following form

$$H = -\sum_i n_i n_{i+1} + x \sum_i (b_i^\dagger b_{i+1} + b_i b_{i+1}^\dagger). \tag{A.37}$$

Since we restricted ourselves to the two-particle block, the hopping term is rewritten as

$$b_i^\dagger b_{i+1} + b_i b_{i+1}^\dagger = A_2 + A_3 + A_4 + A_5 + A_6 + A_7 + \mathcal{O}(A_8), \tag{A.38}$$

with the corresponding monoms A_i listed in table 4. As we will see, the limitation up to A_7 is sufficient, as further terms do not contribute to our calculations. To improve readability, we divide the calculations into first and second order.

A.4.1. First order

To calculate the first order, we have to evaluate $[\eta[V], H_0]$. Here important to note is

$$\eta[V] = \eta[A_2] + \eta[A_3]. \tag{A.39}$$

Therefore, the corresponding commutator relations are

$$[\eta[A_2], H_0] = A_2, \tag{A.40}$$
$$[\eta[A_3], H_0] = A_3. \tag{A.41}$$

Arising terms, consisting of more than 4 operators, are discarded, since only the 2QP sector is under study.

A.4.2. Second order

Table 4: Basis terms

Index i	Monom A_i	$O_{\min}(A_i)$
0	$b_i^\dagger b_i b_{i+1}^\dagger b_{i+1}$	0
2	$b_i b_{i+1}^\dagger b_{i+2}^\dagger b_{i+2} + h.c.$	1
3	$b_i^\dagger b_i b_{i+1}^\dagger b_{i+2} + h.c.$	1
4	$b_i^\dagger b_i b_{i+2}^\dagger b_{i+3} + h.c.$	1
5	$b_i^\dagger b_{i+1} b_{i+3}^\dagger b_{i+3} + h.c.$	1
6	$b_i^\dagger b_i b_{i+3}^\dagger b_{i+4} + h.c.$	1
7	$b_i^\dagger b_{i+1} b_{i+4}^\dagger b_{i+4} + h.c.$	1
8	$b_i^\dagger b_{i+1}^\dagger b_{i+1} b_{i+2} + h.c.$	2
9	$b_i^\dagger b_i b_{i+2}^\dagger b_{i+2}$	2
10	$b_i b_{i+1}^\dagger b_{i+2} b_{i+3}^\dagger + h.c.$	2
11	$b_i b_{i+1}^\dagger b_{i+2}^\dagger b_{i+3} + h.c.$	2
12	$b_i b_{i+2}^\dagger b_{i+3}^\dagger b_{i+3} + h.c.$	2
13	$b_i^\dagger b_i b_{i+1} b_{i+3}^\dagger + h.c.$	2
14	$b_i b_{i+1}^\dagger b_{i+2}^\dagger b_{i+3} + h.c.$	2

As a next step, contributions from

$$[\eta[V], V] \qquad \text{and} \qquad [\eta[[\eta[V], V]], H_0] \tag{A.42}$$

are needed. Therefore, we calculate

$$[\eta[A_2], A_2] = -2n_i n_{i+1} + 2n_i n_{i+2} \tag{A.43}$$
$$[\eta[A_2], A_3] = -b_i b_{i+1}^\dagger b_{i+1} b_{i+2} - \text{h.c.} + b_i b_{i+1}^\dagger b_{i+2} b_{i+3}^\dagger + \text{h.c.} \tag{A.44}$$

$$[\eta[A_2], A_4] = -b_i b_{i+1}^\dagger b_{i+2}^\dagger b_{i+3} - \text{h.c.} \tag{A.45}$$
$$[\eta[A_2], A_5] = -b_i b_{i+2}^\dagger b_{i+3}^\dagger b_{i+3} - \text{h.c.} \tag{A.46}$$
$$[\eta[A_2], A_6] = 0 \tag{A.47}$$
$$[\eta[A_2], A_7] = 0 \tag{A.48}$$
$$[\eta[A_3], A_2] = -b_i b_{i+1}^\dagger b_{i+1} b_{i+2}^\dagger - \text{h.c.} + b_i b_{i+1}^\dagger b_{i+2} b_{i+3}^\dagger + \text{h.c.} \tag{A.49}$$
$$[\eta[A_3], A_3] = -2n_i n_{i+1} + 2n_i n_{i+2} \tag{A.50}$$
$$[\eta[A_3], A_4] = -b_i^\dagger b_i b_{i+1} b_{i+3}^\dagger - \text{h.c.} \tag{A.51}$$
$$[\eta[A_3], A_5] = -b_i b_{i+1}^\dagger b_{i+2}^\dagger b_{i+3} - \text{h.c.} \tag{A.52}$$
$$[\eta[A_3], A_6] = 0 \tag{A.53}$$
$$[\eta[A_3], A_7] = 0. \tag{A.54}$$

The obtained set of monoms is closed, because

$$[\eta[A_{11}], A_0] = A_{11}, \tag{A.55}$$
$$[\eta[A_{12}], A_0] = A_{12}, \tag{A.56}$$
$$[\eta[A_{13}], A_0] = A_{13}, \tag{A.57}$$
$$[\eta[A_{14}], A_0] = A_{14,} \tag{A.58}$$

Together, all commutators up to second order are:

$$[\eta[A_2], A_0] = D_{2,2,0} A_2 = A_2 \tag{A.59}$$
$$[\eta[A_3], A_0] = D_{3,3,0} A_3 = A_3 \tag{A.60}$$
$$[\eta[A_2], A_2] = D_{9,2,2} A_9 + D_{022} A_0 = 2A_9 - 2A_0 \tag{A.61}$$
$$[\eta[A_2], A_3] = D_{10,2,3} A_{10} + D_{823} A_8 = A_{10} - A_8 \tag{A.62}$$
$$[\eta[A_3], A_2] = D_{10,3,2} A_{10} + D_{832} A_8 = A_{10} - A_8 \tag{A.63}$$
$$[\eta[A_3], A_3] = D_{0,3,3} A_0 + D_{933} A_9 = -2A_0 + 2A_9 \tag{A.64}$$
$$[\eta[A_2], A_4] = D_{11,2,4} A_{11} = -A_{11} \tag{A.65}$$
$$[\eta[A_2], A_5] = D_{12,2,5} A_{12} = -A_{12} \tag{A.66}$$
$$[\eta[A_3], A_4] = D_{13,3,4} A_{13} = -A_{13} \tag{A.67}$$
$$[\eta[A_3], A_5] = D_{14,3,5} A_{14} = -A_{14} \tag{A.68}$$
$$[\eta[A_{11}], A_0] = D_{11,11,0} A_{11} = A_{11} \tag{A.69}$$
$$[\eta[A_{12}], A_0] = D_{12,12,0} A_{12} = A_{12} \tag{A.70}$$
$$[\eta[A_{13}], A_0] = D_{13,13,0} A_{13} = A_{13} \tag{A.71}$$
$$[\eta[A_{14}, A_0] = D_{14,14,0} A_{14} = A_{14}. \tag{A.72}$$

Applying the truncation scheme of deepCUT, leads to the following differential equations:

$$\partial_l h_0 = D_{0,2,2} h_2 h_2 + D_{0,3,3} h_3, \tag{A.73}$$
$$\partial h_2 = D_{2,2,0} h_2 h_0, \tag{A.74}$$
$$\partial h_3 = D_{3,3,0} h_3 h_0, \tag{A.75}$$
$$\partial h_8 = 2 D_{8,3,2} h_3 h_2, \tag{A.76}$$

with the following initial conditions ($l = 0$):

$$h_0(0) = -1, \tag{A.77}$$
$$h_2(0) = x, \tag{A.78}$$
$$h_3(0) = x, \tag{A.79}$$
$$h_8(0) = 0. \tag{A.80}$$

From this, the energy of the bound states can be directly calculated, leading to fig. 57.

References

[1] P. W. Anderson. 'More Is Different'. In: *Science* 177.4047 (1972), pp. 393–396. DOI: 10.1126/science.177.4047.393. eprint: https://www.science.org/doi/pdf/10.1126/science.177.4047.393. URL: https://www.science.org/doi/abs/10.1126/science.177.4047.393.

[2] Lucile Savary and Leon Balents. 'Quantum spin liquids: a review'. In: *Reports on Progress in Physics* 80.1 (Nov. 2016), p. 016502. ISSN: 1361-6633. DOI: 10.1088/0034-4885/80/1/016502. URL: http://dx.doi.org/10.1088/0034-4885/80/1/016502.

[3] Piers Coleman. 'Scales and complexity'. In: *Introduction to Many-Body Physics*. Cambridge University Press, 2015, pp. 5–9.

[4] Subir Sachdev. *Quantum Phase Transitions*. 2nd ed. Cambridge University Press, 2011.

[5] R. Moessner and S. L. Sondhi. 'Ising models of quantum frustration'. In: *Phys. Rev. B* 63 (22 May 2001), p. 224401. DOI: 10.1103/PhysRevB.63.224401. URL: https://link.aps.org/doi/10.1103/PhysRevB.63.224401.

[6] M. Powalski et al. 'Disorder by disorder and flat bands in the kagome transverse field Ising model'. In: *Phys. Rev. B* 87 (5 Feb. 2013), p. 054404. DOI: 10.1103/PhysRevB.87.054404. URL: https://link.aps.org/doi/10.1103/PhysRevB.87.054404.

[7] Michael Karbach and Gerhard Muller. *Introduction to the Bethe ansatz I*. 1998. arXiv: cond-mat/9809162 [cond-mat.stat-mech]. URL: https://arxiv.org/abs/cond-mat/9809162.

[8] Ulrich Schollwöck. 'The density-matrix renormalization group in the age of matrix product states'. In: *Annals of Physics* 326.1 (Jan. 2011), pp. 96–192. ISSN: 0003-4916. DOI: 10.1016/j.aop.2010.09.012. URL: http://dx.doi.org/10.1016/j.aop.2010.09.012.

[9] Román Orús. 'A practical introduction to tensor networks: Matrix product states and projected entangled pair states'. In: *Annals of Physics* 349 (Oct. 2014), pp. 117–158. ISSN: 0003-4916. DOI: 10.1016/j.aop.2014.06.013. URL: http://dx.doi.org/10.1016/j.aop.2014.06.013.

[10] Anders W. Sandvik, Adolfo Avella and Ferdinando Mancini. 'Computational Studies of Quantum Spin Systems'. In: *AIP Conference Proceedings*. AIP, 2010. DOI: 10.1063/1.3518900. URL: http://dx.doi.org/10.1063/1.3518900.

[11] C. Knetter and G.S. Uhrig. 'Perturbation theory by flow equations: dimerized and frustrated S = 1/2 chain'. In: *The European Physical Journal B - Condensed Matter and Complex Systems* 13.2 (Jan. 2000), pp. 209–225. ISSN: 1434-6036. DOI: 10.1007/s100510050026. URL: http://dx.doi.org/10.1007/s100510050026.

[12] H. Krull, N. A. Drescher and G. S. Uhrig. 'Enhanced perturbative continuous unitary transformations'. In: *Phys. Rev. B* 86 (12 Sept. 2012), p. 125113. DOI: 10.1103/PhysRevB.86.125113. URL: https://link.aps.org/doi/10.1103/PhysRevB.86.125113.

[13] Max Hörmann and Kai P. Schmidt. 'Projective cluster-additive transformation for quantum lattice models'. In: *SciPost Phys.* 15 (2023), p. 097. DOI: 10.21468/SciPostPhys.15.3.097. URL: https://scipost.org/10.21468/SciPostPhys.15.3.097.

[14] Sergey Bravyi, David P. DiVincenzo and Daniel Loss. 'Schrieffer–Wolff transformation for quantum many-body systems'. In: *Annals of Physics* 326.10 (Oct. 2011), pp. 2793–2826. ISSN: 0003-4916. DOI: 10.1016/j.aop.2011.06.004. URL: http://dx.doi.org/10.1016/j.aop.2011.06.004.

[15] Takeo Matsubara and Hirotsugu Matsuda. 'A Lattice Model of Liquid Helium, I'. In: *Progress of Theoretical Physics* 16.6 (Dec. 1956), pp. 569–582. ISSN: 0033-068X. DOI: 10.1143/PTP.16.569. eprint: https://academic.oup.com/ptp/article-pdf/16/6/569/5383838/16-6-569.pdf. URL: https://doi.org/10.1143/PTP.16.569.

[16] Carlos E. Soliverez. 'General theory of effective Hamiltonians'. In: *Phys. Rev. A* 24 (1 July 1981), pp. 4–9. DOI: 10.1103/PhysRevA.24.4. URL: https://link.aps.org/doi/10.1103/PhysRevA.24.4.

[17] Philippe Durand. 'Direct determination of effective Hamiltonians by wave-operator methods. I. General formalism'. In: *Phys. Rev. A* 28 (6 Dec. 1983), pp. 3184–3192. DOI: 10.1103/PhysRevA.28.3184. URL: https://link.aps.org/doi/10.1103/PhysRevA.28.3184.

[18] Kenji Suzuki and Ryoji Okamoto. 'Degenerate Perturbation Theory in Quantum Mechanics'. In: *Progress of Theoretical Physics* 70.2 (Aug. 1983), pp. 439–451. ISSN: 0033-068X. DOI: 10.1143/PTP.70.439. eprint: https://academic.oup.com/ptp/article-pdf/70/2/439/5465670/70-2-439.pdf. URL: https://doi.org/10.1143/PTP.70.439.

[19] D. J. Klein. 'Degenerate perturbation theory'. In: *The Journal of Chemical Physics* 61.3 (Aug. 1974), pp. 786–798. ISSN: 0021-9606. DOI: 10.1063/1.1682018. eprint: https://pubs.aip.org/aip/jcp/article-pdf/61/3/786/18891807/786_1_online.pdf. URL: https://doi.org/10.1063/1.1682018.

[20] M Takahashi. 'Half-filled Hubbard model at low temperature'. In: *Journal of Physics C: Solid State Physics* 10.8 (Apr. 1977), p. 1289. DOI: 10.1088/0022-3719/10/8/031. URL: https://dx.doi.org/10.1088/0022-3719/10/8/031.

[21] T. Kato. *Perturbation theory for linear operators*. Grundlehren der mathematischen Wissenschaften. Springer Berlin Heidelberg, 2013. ISBN: 9783662126783. URL: https://books.google.de/books?id=k-7nCAAAQBAJ.

[22] Frédéric Mila and Kai Phillip Schmidt. 'Strong-Coupling Expansion and Effective Hamiltonians'. In: *Introduction to Frustrated Magnetism*. Springer Berlin Heidelberg, Sept. 2010, pp. 537–559. ISBN: 9783642105890. DOI: 10.1007/978-3-642-10589-0_20. URL: http://dx.doi.org/10.1007/978-3-642-10589-0_20.

[23] Christian Knetter, Kai P Schmidt and Götz S Uhrig. 'The structure of operators in effective particle-conserving models'. In: *Journal of Physics A: Mathematical and General* 36.29 (July 2003), p. 7889. DOI: 10.1088/0305-4470/36/29/302. URL: https://dx.doi.org/10.1088/0305-4470/36/29/302.

[24] P. Adelhardt et al. *Monte Carlo based techniques for quantum magnets with long-range interactions*. 2024. arXiv: 2403.00421 [cond-mat.str-el]. URL: https://arxiv.org/abs/2403.00421.

[25] Martin P. Gelfand. 'Series expansions for excited states of quantum lattice models'. In: *Solid State Communications* 98.1 (1996), pp. 11–14. ISSN: 0038-1098. DOI: https://doi.org/10.1016/0038-1098(96)00051-8. URL: https://www.sciencedirect.com/science/article/pii/0038109896000518.

[26] D. J. Priour, M. P. Gelfand and S. L. Sondhi. 'Disorder from disorder in a strongly frustrated transverse-field Ising chain'. In: *Phys. Rev. B* 64 (13 Sept. 2001), p. 134424. DOI: 10.1103/PhysRevB.64.134424. URL: https://link.aps.org/doi/10.1103/PhysRevB.64.134424.

[27] Weihong Zheng et al. 'Linked cluster series expansions for two-particle bound states'. In: *Phys. Rev. B* 63 (14 Mar. 2001), p. 144410. DOI: 10.1103/PhysRevB.63.144410. URL: https://link.aps.org/doi/10.1103/PhysRevB.63.144410.

[28] L S Cederbaum, J Schirmer and H -D Meyer. 'Block diagonalisation of Hermitian matrices'. In: *Journal of Physics A: Mathematical and General* 22.13 (July 1989), p. 2427. DOI: 10.1088/0305-4470/22/13/035. URL: https://dx.doi.org/10.1088/0305-4470/22/13/035.

[29] Gary Schmiedinghoff. 'Applications and extensions of flow equations to closed and open quantum systems'. PhD thesis. Technische Universität Dortmund, 2022.

[30] Sébastien Dusuel and Götz S Uhrig. 'The quartic oscillator: a non-perturbative study by continuous unitary transformations'. In: *Journal of Physics A: Mathematical and General* 37.39 (Sept. 2004), pp. 9275–9294. ISSN: 1361-6447. DOI: 10.1088/0305-4470/37/39/014. URL: http://dx.doi.org/10.1088/0305-4470/37/39/014.

[31] Lukas Schamriß. 'Extracting quantum-critical properties from directly evaluated enhanced perturbative continuous unitary transformations'. MA thesis. Friedrich-Alexander Universtiy Erlangen, Dec. 2023.

[32] Vladimir L. Safonov. *Continuous Unitary Transformations*. 2002. arXiv: quant-ph/0202095 [quant-ph]. URL: https://arxiv.org/abs/quant-ph/0202095.

[33] Alexander Dalgarno, A. L. Stewart and David Robert Bates. 'On the perturbation theory of small disturbances'. In: *Proceedings of the Royal Society of London. Series A. Mathematical and Physical Sciences* 238.1213 (1956), pp. 269–275. DOI: 10.1098/rspa.1956.0219. eprint: https://royalsocietypublishing.org/doi/pdf/10.1098/rspa.1956.0219. URL: https://royalsocietypublishing.org/doi/abs/10.1098/rspa.1956.0219.

[34] P G Hornby and M N Barber. 'Perturbation series for the mass gap of the (1+1)-dimensional O(2)-model'. In: *Journal of Physics A: Mathematical and General* 18.5 (Apr. 1985), p. 827. DOI: 10.1088/0305-4470/18/5/015. URL: https://dx.doi.org/10.1088/0305-4470/18/5/015.

[35] C.M. Bender and S.A. Orszag. *Advanced Mathematical Methods for Scientists and Engineers I: Asymptotic Methods and Perturbation Theory*. Springer New York, 2013. ISBN: 9781475730692. URL: https://books.google.de/books?id=xz0mBQAAQBAJ.

[36] Kai Phillip Schmidt. 'Spectral Properties of Quasi One-dimensional Quantum Antiferromagnets . Perturbative Continuous Unitary Transformations'. PhD thesis. Universität zu Köln, 2004.

[37] J. VON NEUMANN and E. WIGNER. 'ON THE BEHAVIOUR OF EIGENVALUES IN ADIABATIC PROCESSES'. In: *Quantum Chemistry*, pp. 25–31. DOI: 10.1142/9789812795762_0002. eprint: https://www.worldscientific.com/doi/pdf/10.1142/9789812795762_0002. URL: https://www.worldscientific.com/doi/abs/10.1142/9789812795762_0002.

[38] K. Coester et al. 'A generalized perspective on non-perturbative linked-cluster expansions'. In: *EPL (Europhysics Letters)* 110.2 (Apr. 2015), p. 20006. ISSN: 1286-4854. DOI: 10.1209/0295-5075/110/20006. URL: http://dx.doi.org/10.1209/0295-5075/110/20006.

[39] Kris Coester. 'Quasiparticle pictures and graphs - from perturbative to non-perturbative linked-cluster expansions'. PhD thesis. Technische Universität Dortmund, 2015. URL: http://dx.doi.org/10.17877/DE290R-16955.

[40] J P Malrieu, P Durand and J P Daudey. 'Intermediate Hamiltonians as a new class of effective Hamiltonians'. In: *Journal of Physics A: Mathematical and General* 18.5 (Apr. 1985), p. 809. DOI: 10.1088/0305-4470/18/5/014. URL: https://dx.doi.org/10.1088/0305-4470/18/5/014.

[41] Stefano Battaglia et al. 'Regularized CASPT2: an Intruder-State-Free Approach'. In: *Journal of Chemical Theory and Computation* 18.8 (2022). PMID: 35876618, pp. 4814–4825. DOI: 10.1021/acs.jctc.2c00368. eprint: https://doi.org/10.1021/acs.jctc.2c00368. URL: https://doi.org/10.1021/acs.jctc.2c00368.

[42] W D Heiss and A L Sannino. 'Avoided level crossing and exceptional points'. In: *Journal of Physics A: Mathematical and General* 23.7 (Apr. 1990), p. 1167. DOI: 10.1088/0305-4470/23/7/022. URL: https://dx.doi.org/10.1088/0305-4470/23/7/022.

[43] Thomas H Schucan and Hans A Weidenmüller. 'Perturbation theory for the effective interaction in nuclei'. In: *Annals of Physics* 76.2 (1973), pp. 483–509. ISSN: 0003-4916. DOI: https://doi.org/10.1016/0003-4916(73)90044-4. URL: https://www.sciencedirect.com/science/article/pii/0003491673900444.

[44] Elizabeth M. Y. Lee and Adam P. Willard. 'Solving the Trivial Crossing Problem While Preserving the Nodal Symmetry of the Wave Function'. In: *Journal of Chemical Theory and Computation* 15.8 (2019). PMID: 31305997, pp. 4332–4343. DOI: 10.1021/acs.jctc.9b00302. eprint: https://doi.org/10.1021/acs.jctc.9b00302. URL: https://doi.org/10.1021/acs.jctc.9b00302.

[45] W D Heiss. 'Chirality of wavefunctions for three coalescing levels'. In: *Journal of Physics A: Mathematical and Theoretical* 41.24 (June 2008), p. 244010. DOI: 10.1088/1751-8113/41/24/244010. URL: https://dx.doi.org/10.1088/1751-8113/41/24/244010.

[46] *Plotly plot of the Riemann surface, real part of square root.* https://nbviewer.org/github/empet/Math/blob/master/Riemann-Surface-sqrt-z.ipynb. Accessed: 2024-08-01.

[47] Matthew Huynh. *A BRIEF INTRODUCTION TO RIEMANN SURFACES.* https://web.ma.utexas.edu/users/drp/files/Spring2020Projects/drp_project%20-%20Matthew%20Huynh.pdf. 2020.

[48] M. Abramowitz and I.A. Stegun. *Handbook of Mathematical Functions: With Formulas, Graphs, and Mathematical Tables.* Applied mathematics series. Dover Publications, 1965. ISBN: 9780486612720. URL: https://books.google.de/books?id=MtU8uP7XMvoC.

[49] Nimrod Moiseyev. *Non-Hermitian Quantum Mechanics.* Cambridge University Press, 2011.

[50] W D Heiss. 'The physics of exceptional points'. In: *Journal of Physics A: Mathematical and Theoretical* 45.44 (Oct. 2012), p. 444016. ISSN: 1751-8121. DOI: 10.1088/1751-8113/45/44/444016. URL: http://dx.doi.org/10.1088/1751-8113/45/44/444016.

[51] Leon Schiller. 'Ising Models on Frustrated Chains in a Light Induced Quantised Transverse'. MA thesis. Friedrich-Alexander Universtiy Erlangen, Nov. 2021.

[52] S. Suzuki, J. Inoue and B.K. Chakrabarti. *Quantum Ising Phases and Transitions in Transverse Ising Models.* Lecture Notes in Physics. Springer Berlin Heidelberg, 2012. ISBN: 9783642330407. URL: https://books.google.de/books?id=NVM5jgEACAAJ.

[53] Jaan Oitmaa, Chris Hamer and Weihong Zheng. 'Quantum spin models at T = 0'. In: *Series Expansion Methods for Strongly Interacting Lattice Models.* Cambridge University Press, 2006, pp. 74–98.

[54] Martin P. Gelfand and Rajiv R. P. Singh. 'High-order convergent expansions for quantum many particle systems'. In: *Advances in Physics* 49.1 (2000), pp. 93–140. DOI: 10.1080/000187300243390, eprint: https://doi.org/10.1080/000187300243390. URL: https://doi.org/10.1080/000187300243390.

[55] J. C. Xavier et al. 'Coexistence of spontaneous dimerization and magnetic order in a transverse-field Ising ladder with four-spin interactions'. In: *Phys. Rev. B* 105 (2 Jan. 2022), p. 024430. DOI: 10.1103/PhysRevB.105.024430. URL: https://link.aps.org/doi/10.1103/PhysRevB.105.024430.

[56] Sébastien Dusuel et al. 'Bound states in two-dimensional spin systems near the Ising limit: A quantum finite-lattice study'. In: *Phys. Rev. B* 81 (6 Feb. 2010), p. 064412. DOI: 10.1103/PhysRevB.81.064412. URL: https://link.aps.org/doi/10.1103/PhysRevB.81.064412.

[57] Gianpaolo Torre et al. *Interplay between local and non-local frustration in the 1D ANNNI chain I – The even case*. 2024. arXiv: 2406.19449 [cond-mat.str-el]. URL: https://arxiv.org/abs/2406.19449.

[58] Mahmoud Abdelshafy and Marcos Rigol. 'Numerical linked-cluster expansions for two-dimensional spin models with continuous disorder distributions'. In: *Phys. Rev. E* 109 (5 May 2024), p. 054127. DOI: 10.1103/PhysRevE.109.054127. URL: https://link.aps.org/doi/10.1103/PhysRevE.109.054127.

[59] M. Cea et al. *Exploring the Phase Diagram of the quantum one-dimensional ANNNI model*. 2024. arXiv: 2402.11022 [cond-mat.str-el]. URL: https://arxiv.org/abs/2402.11022.

[60] Matteo Beccaria, Massimo Campostrini and Alessandra Feo. 'Evidence for a floating phase of the transverse ANNNI model at high frustration'. In: *Physical Review B* 76.9 (Sept. 2007). ISSN: 1550-235X. DOI: 10.1103/physrevb.76.094410. URL: http://dx.doi.org/10.1103/PhysRevB.76.094410.

[61] I. Peschel and V.J. Emery. 'Calculation of spin correlations in two-dimensional Ising systems from one-dimensional kinetic models'. In: *Z. Physik B - Condensed Matter* 43 (1981). DOI: https://doi.org/10.1007/BF01297524. URL: https://link.springer.com/article/10.1007/BF01297524#citeas.

[62] Zhiyao Zuo et al. 'Scaling theory of the Kosterlitz-Thouless phase transition'. In: *Phys. Rev. B* 104 (21 Dec. 2021), p. 214108. DOI: 10.1103/PhysRevB.104.214108. URL: https://link.aps.org/doi/10.1103/PhysRevB.104.214108.

[63] Amit Dutta et al. *Quantum Phase Transitions in Transverse Field Spin Models: From Statistical Physics to Quantum Information*. Cambridge University Press, 2015.

[64] Sergej Flach et al. 'Detangling flat bands into Fano lattices'. In: *EPL (Europhysics Letters)* 105.3 (Feb. 2014), p. 30001. ISSN: 1286-4854. DOI: 10.1209/0295-5075/105/30001. URL: http://dx.doi.org/10.1209/0295-5075/105/30001.

[65] K. Coester et al. 'Quantum disorder and local modes of the fully-frustrated transverse field Ising model on a diamond chain'. In: *Phys. Rev. B* 88 (18 Nov. 2013), p. 184402. DOI: 10.1103/PhysRevB.88.184402. URL: https://link.aps.org/doi/10.1103/PhysRevB.88.184402.

[66] Maximilian Bayer. 'On the study of bound states in quantum lattice models Master'. MA thesis. Friedrich-Alexander Universtiy Erlangen, June 2024.

[67] David J. Luitz and Francesco Piazza. 'Exceptional points and the topology of quantum many-body spectra'. In: *Phys. Rev. Res.* 1 (3 Oct. 2019), p. 033051. DOI: 10.1103/PhysRevResearch.1.033051. URL: https://link.aps.org/doi/10.1103/PhysRevResearch.1.033051.

[68] G Y Hu and R F O'Connell. 'Analytical inversion of symmetric tridiagonal matrices'. In: *Journal of Physics A: Mathematical and General* 29.7 (Apr. 1996), p. 1511. DOI: 10.1088/0305-4470/29/7/020. URL: https://dx.doi.org/10.1088/0305-4470/29/7/020.

[69] Marcos Mariño. 'Propagator and Resolvent'. In: *Advanced Topics in Quantum Mechanics*. Cambridge University Press, 2021, pp. 1–30.

Acknowledgments

A big thank you goes to Prof. Kai Schmidt, who not only made this work possible in the first place, but also always had time for regular meetings, even during stressful weeks. I would also like to express my special thanks to Max Hörmann, who not only supported the project over the entire period, but also patiently answered all my questions at all times. It was always a pleasure to listen to his ideas and gain further insight into the physical connections. The many conversations in the coffee room will be always in good memory.
I would also like to thank Lukas and Matthias, who helped me with their code and general questions about deepCUT. I also want to express my gratitude to the entire group, not only for the wonderful atmosphere, but also for the great support I received from everyone at all times during the project.

Eigenständigkeitserklärung

Hiermit versichere ich, dass ich die vorliegende Masterarbeit selbstständig verfasst habe. Ich versichere, dass ich keine anderen als die angegebenen Quellen benutzt und alle wörtlich oder sinngemäß aus anderen Werken übernommenen Aussagen als solche gekennzeichnet habe, und dass die eingereichte Arbeit weder vollständig noch in wesentlichen Teilen Gegenstand eines anderen Prüfungsverfahren gewesen ist.

Ort, Datum

Harald Leiser